New Jersey Institute of Technology
Digital Commons @ NJIT

Dissertations | Theses and Dissertations

Spring 2000

# Simulation and modeling of magnetically-assisted impaction coating (MAIC) process for dry particle coating

Bodhisattwa Chaudhuri
*New Jersey Institute of Technology*

Follow this and additional works at: https://digitalcommons.njit.edu/dissertations

 Part of the Mechanical Engineering Commons

Recommended Citation
Chaudhuri, Bodhisattwa, "Simulation and modeling of magnetically-assisted impaction coating (MAIC) process for dry particle coating" (2000). *Dissertations*. 394.
https://digitalcommons.njit.edu/dissertations/394

This Dissertation is brought to you for free and open access by the Theses and Dissertations at Digital Commons @ NJIT. It has been accepted for inclusion in Dissertations by an authorized administrator of Digital Commons @ NJIT. For more information, please contact digitalcommons@njit.edu.

# Copyright Warning & Restrictions

The copyright law of the United States (Title 17, United States Code) governs the making of photocopies or other reproductions of copyrighted material.

Under certain conditions specified in the law, libraries and archives are authorized to furnish a photocopy or other reproduction. One of these specified conditions is that the photocopy or reproduction is not to be "used for any purpose other than private study, scholarship, or research." If a, user makes a request for, or later uses, a photocopy or reproduction for purposes in excess of "fair use" that user may be liable for copyright infringement,

This institution reserves the right to refuse to accept a copying order if, in its judgment, fulfillment of the order would involve violation of copyright law.

Please Note: The author retains the copyright while the New Jersey Institute of Technology reserves the right to distribute this thesis or dissertation

Printing note: If you do not wish to print this page, then select "Pages from: first page # to: last page #" on the print dialog screen

NJIT New Jersey's Science & Technology University

The Van Houten library has removed some of the personal information and all signatures from the approval page and biographical sketches of theses and dissertations in order to protect the identity of NJIT graduates and faculty.

## ABSTRACT

## SIMULATION AND MODELING OF MAGNETICALLY-ASSISTED IMPACTION COATING (MAIC) PROCESS FOR DRY PARTICLE COATING

**by**
**Bodhisattwa Chaudhuri**

The objective of proposed research is to model and understand the processes happening at multiple length and time scales in magnetically assisted impaction coating process. The smallest length scale is of the order of the molecular size and is important because during collisions the molecules rearrange themselves to form a semi-permanent bond between the core and secondary particles, which is studied by using the results of direct numerical integration of the governing Newton's equations. The effect of parameters such as size, orientation and relative velocity of particles on the collision mechanics is quantified. The largest length scale which is the device scale determines the magnetic field strength that is needed to fluidize the mixture. The intermediate length scale is of the order of particle size. The frequency of collision among the fluidized particles at this length scale determines the residence time required to coat the particles. The velocities and the normal force attained by the non-magnetic particles are estimated and compared with the same necessary for coating process. The deformation of the virtual guest particles are estimated from the normal force of collision of host particles and the van der Waal force of attraction is calculated. The attraction force is found to be more than the separation force of guest from the host, which is favorable for the coating process.

# SIMULATION AND MODELING OF MAGNETICALLY-ASSISTED IMPACTION COATING (MAIC) PROCESS FOR DRY PARTICLE COATING

by
**Bodhisattwa Chaudhuri**

**A Dissertation**
**Submitted to the Faculty of**
**New Jersey Institute of Technology**
**In Partial Fulfillment of the Requirements for the Degree of**
**Doctor of Philosophy in Mechanical Engineering**

**Department of Mechanical Engineering**

**May 2000**

Copyright © 2000 by Bodhisattwa Chaudhuri
ALL RIGHTS RESERVED

## APPROVAL PAGE

## SIMULATION AND MODELING OF MAGNETICALLY-ASSISTED IMPACTION COATING (MAIC) PROCESS FOR DRY PARTICLE COATING

**Bodhisattwa Chaudhuri**

---

Dr. Rajesh N. Dave, Dissertation Advisor — Date
Professor of Mechanical Engineering, NJIT

---

Dr. Pushpendra Singh, Dissertation Co-Advisor — Date
Assistant Professor of Mechanical Engineering, NJIT

---

Dr. Robert Pfeffer, Committee Member — Date
Professor of Chemical Engineering, NJIT

---

Dr. Anthony D. Rosato, Committee Member — Date
Associate Professor of Mechanical Engineering, NJIT

---

Dr. Rong Chen, Committee Member — Date
Professor of Mechanical Engineering, NJIT

## BIOGRAPHICAL SKETCH

**Author:** Bodhisattwa Chaudhuri

**Degree:** Doctor of Philosophy in Mechanical Engineering

**Date:** May 2000

**Undergraduate and Graduate Education:**

- Doctor of Philosophy in Mechanical Engineering
  New Jersey Institute of Technology
  Newark, New Jersey, 2000

- Master of Science in Chemical Engineering
  Indian Institute of Science
  Bangalore, India, 1996

- Bachelor of Science in Chemical Engineering
  Jadavpur University
  Calcutta, India, 1992

**Major:** Mechanical Engineering

**Publications and Proceedings:**

B.Chaudhuri, J.M.Modak, Optimization of fed-batch bioreactors using a neural network model, Bioprocess Engineering,19, 1, 71-79, 1998.

R.Dave, C.Y.Wu, B.Chaudhuri, S.Watano, Magnetically mediated flow enhancement for controlled powder discharge of cohesive powders,Powder Technology, 1999, Accepted.

C.Y.Wu, W.C.Dunphy, B.Chaudhuri, M.Ramlakhan, P.Singh, R.Pfeffer, R.Dave, Particle Coating by magnetically-Assisted Impaction Coating, 16th AAAR Conference, October 14-17, 1997, Denver, Colorado.

**Publications and Proceedings(continued)**

B. Chaudhuri, P. Singh, C. Y. Wu, R. Pfeffer, R. N. Dave, Simulation and Modeling of Magnetically-Assisted Impaction Coating(MAIC) Process for Dry Particle Coating; Proceedings of the World Congress on Particle Technology, July 7-9, 1998, Brighton, UK.

C. Babets, B. Chaudhuri, E. Geskin, Modeling and optimization of Water Jet Cutting process using artificial neural networks, $10^{th}$ American Waterjet Conference, Houston, Texas, August, 1999.

**Dedicated to my wife Dipanwita and daughter Basudha who endured all the difficulties in making our dreams come true.**

## ACKNOWLEDGMENT

The author wishes to express his sincere gratitude to his advisor, Dr. Rajesh N. Dave, for his guidance, friendship and moral support throughout this research. He advised and helped the author to full extent in tackling all the barriers in academic and personal life. The author would like to thank Dr.Pushpendra Singh and Dr. Robert Pfeffer for many stimulating discussions.

Special thanks to Dr. Anthony Rosato and Dr. Rong Chen for serving as members of the committee. The author would like to thank all of his research group colleagues namely Dr C.Y.Wu, Michelle Ramlakhan, Ajit Mujumdar, T.P. Ravichandran, Wengliang Chen, William Dunphy, Felix Alcocer and Gregory James for their support and cooperation during the research. The author is also grateful to Dr Singh for providing the MD code and Dr. Moakher of Rutgers for providing the DEM code, which were modified for the purpose of these research. The author is very thankful to Dr Moinuddin Malik for the time he spent correcting the thesis. Annette Damiano's help in formatting the thesis is also acknowledged. The helps from the staff of the library and the department of Engineering Computing are also sincerely acknowledged.

## TABLE OF CONTENTS

**Chapter** **Page**

## TABLE OF CONTENTS
## (Continued)

**Chapter** **Page**

## LIST OF FIGURES

**Figure** **Page**

## LIST OF FIGURES
## (continued)

**Figure** **Page**

## LIST OF FIGURES
## (continued)

**Figure** **Page**

## LIST OF FIGURES
## (continued)

**Figure** **Page**

## LIST OF FIGURES
## (continued)

**Figure** **Page**

## LIST OF FIGURES
## (continued)

**Figure** **Page**

## LIST OF TABLES

**Table** **Page**

# CHAPTER 1

# INTRODUCTION

## 1.1 Significance and Motivation

In several key industries, such as, food, biomaterials, superconductors, pharmaceutical, and ceramics among others coating of particulate materials is done routinely to change their physio-chemical surface properties of particulates. Such engineered composite particulates can (1) have completely different functionality, (2) be highly cost effective alternative to expensive materials, and (3) have improved flowability, wettability, dispersibility, electro-magnetic, thermal and other characteristics. To quote some specific example, in pharmaceutical industry cohesive particles are coated with non-cohesive secondary particles of smaller size. The composite particles thus produced are non-cohesive, and therefore easier to transport. In some applications, the hydrophilic particles need to be protected from moisture. This again can be achieved by coating such particles with hydrophobic secondary particles and, thus making them hydrophobic. Conventional techniques such as wet coating and plasma spray are now considered environmentally unsafe as these processes produce hazardous waste [1]. Dry coating processes, on the other hand, operate under dry environment and arc pollution free. Consequently dry coating processes have gained significant popularity over the past few years. Herein, one such dry coating process called MAIC (magnetically assisted impaction coating) will be discussed that has been successfully used to coat particulates.

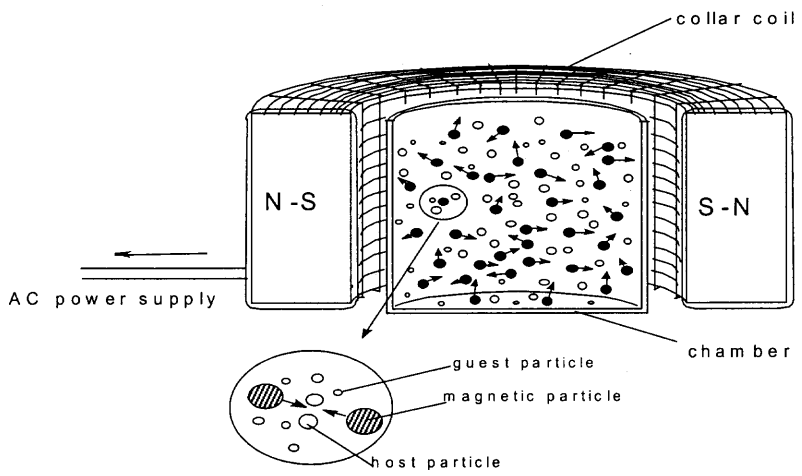


**Fig 1.1** The experimental setup of MAIC process

The MAIC process for coating particulates can be used in both batch and continuous modes [1]. In the batch MAIC, a hollow cylinder filled with the magnetic (200-1000 micron in diameter)particles, the host (1-200 micron in diameter) particles and secondary (20nm - 1 micron in diameter) particles is placed in an alternating magnetic field generated by a field coil of squirrel cage AC motor. In an alternating magnetic field a time-dependent torque acts on the non-spherical magnetic particles. The magnitude and direction of the torque depends on the relative orientation of the magnetic particles and the instantaneous magnetic field. The torque causes magnetic particles to rotate and collide randomly with the core and secondary particles, as well as with each other. Therefore, for the random collisions, their orientations relative to the applied magnetic field and the torque acting on the magnetic particles can be assumed random. The random torque and the resulting random collisions among the magnetic and other particles cause

the particulate mixture to "fluidize". The random collisions also lead to mixing and plastic deformation of particles. Agglomerates of the guest particles (nano particles are generally agglomerates) get attached to the host surface and the repeated collisions between host (coated with fine agglomerates) and host and/or host and magnetic particles result in deagglomeration and eventual bonding of a thin layer of fine particles. At the end of the MAIC process the magnetic particles can be easily separated from the mixture by using sieves and/or magnetic separations.

Our objective in this research is to develop a model that would allow us to predict and control the MAIC coating process. As we will discuss in the next section, there are several important factors that collectively determine the efficiency of the MAIC process. For developing an effective theory, it is important to identify and include these factors in the model. Specifically, for modeling the MAIC process, an understanding of the processes happening at multiple length and time scales is required. The largest length scale obviously is the device scale, which, for example, determines the magnetic field strength and the nature of the motion of magnetic particle that are needed to fluidize the mixture. The intermediate length scale is of the order of host particle size. The frequency of collisions among the fluidized particles at this length scale determines the residence time required to coat the particles. The focus of the study is on collisions between host/host and host/magnetic particles in order to determine the relative velocities and frequency of collisions. The third length scale is of the order of the molecular size. This length scale is important because during collisions the molecules rearrange themselves to form a semi-permanent bond between the host and secondary particles. It is, however,

possible to divide this complex problem into three relatively simpler sub-problems because the time scales for the above three length scales are quite different.

### 1.2 Factors Determining the Efficiency of the MAIC Process

There are two key factors that determine the efficiency of the MAIC process. First, the core and secondary particles should be thoroughly mixed together so that the secondary particles are in contact with the surface of core particles. This is difficult to achieve in practice because the core and secondary particles differ in size by at least an order of magnitude, and thus when the mixture is agitated the gravitational force causes it to segregate. Second, the relative velocity(of the center of mass of particles) distribution for the secondary and core particles, must include the range where the collisions are sufficiently strong for forming semi-permanent bonds. This is required because when the secondary particles are simply placed close to the surface of a core particle the attractive forces are not strong enough to hold them together --the secondary particles can be easily rubbed off. It is therefore necessary to have the relative velocity distribution such that adequate plastic deformation occurs during the collisions. The plastic deformation increases the contact area between the core and secondary particles, and thus also the magnitude of the attractive van der Walls force to a level necessary for forming a semi-permanent bond. The relative velocity between the particles, however, should not be too large because then the particles are likely to rebound away from each other. Experiments show that the relative hardness of the particles plays a role in determining the optimal relative velocity range [1]. The parameters listed below will be also investigated as they are believed to play a role in the MAIC process:

**(a)** The relative sizes of the core, secondary and magnetic particles

**(b)** The electrical power input and the frequency of the magnetic field

## 1.3 Literature Review on Modeling

### 1.3.1 Analytical Modeling

The adhesion induced deformation was first considered by Bradley [2,3] who gave the following equation for the force of attraction between two contacting rigid spheres of radii $R_1$ and $R_2$,

$$F = 4\pi\gamma \frac{R_1 R_2}{R_1 + R_2} \tag{1}$$

where $\gamma$ is the surface energy of the spheres.

Derjaguin[4] calculated the contact radius resulting from adhesion forces by assuming that the particles acted as Hertzian indentors with the applied load $P^0$ arising from van der Waals interactions. Accordingly, he evaluated that for a rigid particle in contact with compliant substrate, the contact radius a would be related to the particle radius R by

$$a^3 = 0.75\, P^0 \left[\frac{1-\upsilon^2}{E}\right] R \tag{2}$$

where and E and ν are Young's modulus and Poisson ratio, respectively, of the substrate and $P^0$ is given by

$$P^0 = \frac{hw}{8\pi z_0^2} R \tag{3}$$

where $z_0$ is the separation distance (for irregularities on the surfaces) in between the particle and the substrate and *hw* is the Hamaker coefficient.

The generalization of Derjaguin's model of particle adhesion was done by Krupp[5] to allow for cases where the stress exceeded the yield strength of the material. He found that the contact area could be divided into two concentric regions: an inner region of radius $a_1$, which being subjected to higher stresses, would deform plastically and an outer annulus extending from radius $a_1$ to the total contact radius, $a_0$ which being subjected to lower stresses, would deform elastically. Accordingly,

$$\pi a_0^2 = \frac{P^0}{H(t)} + \frac{1}{3}\left[\frac{\pi^{3/2}(1-\upsilon^2)RH(t)}{2E}\right]^2 \tag{4}$$

$$\pi a_1^2 = \frac{P^0}{H(t)} + \frac{1}{3}\left[\frac{\pi^{3/2}(1-\upsilon^2)RH(t)}{2E}\right]^2 \tag{5}$$

where determination of the time dependent hardness *H(t)* is phenomenological . He allowed the contact radius to reach a limiting size, while assuming that *H(t)* approached an asymptotic value of the order of $10^{-3}$ E within approximately 30 minutes.

The aforementioned classical theories of particle adhesion, assumed the interactions to be compressive. Modern understanding of particle adhesion began with the theory by Johnson et al. [6], who proposed an adhesion theory that considers both the tensile and compressive interactions (Johnson-Kendall-Roberts theory or JKR theory). According to the JKR theory, all interactions that occur within the contact zone and the resulting deformations are elastic. Dealing the problem from a thermodynamic rather than

molecular viewpoint, the JKR theory predicts the following relation between contact radius and particle radius:

$$a^3 = \frac{R}{K}\left\{ P + 3\omega_A \pi R + \left[ 6\omega_A \pi R P + \left(3\omega_A \pi R\right)^2 \right]^{0.5} \right\} \quad (6)$$

where P is the externally applied load, $\omega_A$ is the work of adhesion and is related to the surface energy $\gamma_1$ and $\gamma_2$ and the interfacial energy $\gamma_{12}$ by

$$\omega_A = \gamma_1 + \gamma_2 - \gamma_{12} \quad (7)$$

and

$$K = 4/\left[3\pi\left(k_1 + k_2\right)\right] \quad (8)$$

where

$$k_i = \frac{1 - \nu_i^2}{\pi E_i} \quad (9)$$

the subscripts of 1 and 2 are for the two materials involved. According to this theory, the separation of the particle from the surface occurs when

$$P_S = -1.5\ \omega_A \pi R \quad (10)$$

where $P_S$ is the separating load.

They also calculated the central displacement and the stress distribution in the contact circle. When $\omega_A = 0$ the equations reduce to those of Hertz theory (1881). One difficulty with JKR theory is that it predicts an infinite stress at the edge of the contact circle where the surfaces are expected to bend infinitely sharply through $90^0$. This unphysical situation arises because the JKR theory is a continuum theory and implicitly assumes that the attractive forces between the two surfaces act over an infinitesimally small range [24].

Derjaguin et.al. [7] calculated the same radii with a molecular level approach (DMT theory or Derjaguin-Muller-Toporov theory). Muller et al. [8,9] established a new model (MYD or Muller-Yushchenko-Derjaguin theory) using Lennard-Jones potential and showed JKR and DMT are special cases of the MYD model, with JKR model being valid for low modulus, high surface energy, and larger size particles, and DMT model for rigid materials having lower surface energies and for smaller size particles. The problem of JKR disappears as soon as the attractive force law between surfaces are allowed to have a finite range, by assuming a Lennard-Jones potential. However, in small deformations the adhesion forces change from JKR limit of $P_S = - 3\ \omega_A \pi R$ to the DMT limit of $P_S = - 4\ \omega_A \pi R$ .

Rogers and Reed [10] found the effect of particle-substrate impacts, and the resulting plastic and elastic deformations, on adhesion. Dahneke [11] proposed a simple, conservation of energy model for characterizing the particle-surface-collision, namely, the idealized collision of a homogenous, solid, non-rotating particle moving at a normal incidence towards a flat, smooth surface of a solid body in vacuum. The model fits well with the experimental data of collision of 1.27 μm diameter polystyrene spheres striking a polished fused-silica surface.

Maugis *et.al* [30] searched for the role of surface forces on deformation and adhesion in metal microcontacts. Plastic deformation under zero applied load was initially evaluated. The ductile or the brittle separation under an external force was evaluated followed by an elastoplastic or plastic contact of two metal surfaces. Maugis[31] used a Dugdale model to continuously transit from the JKR model to DMT approximations (models discussed in following section). He considered the adhesion

force to be constant over a certain length of the crack tip in a contact. The internal loading acting in the air gap was cancelled for the external loading. The energy release rate and the equilibrium conditions are also defined and plotted against force or displacement.

More recently Maugis[32] extended the JKR theory of elastic contact of spheres to large contact radii. Rimai's group experimented on adhesion of small particles on soft elastic surfaces and found that contact radius under zero load can be rather large and does not vary with particle radius to the 2/3 power. The extension of JKR theory here worked well with the said experiments. Thus for spherical particles of small radii on a soft elastic solid, the ratio of the radius of contact over the ball radius can be so large that the parabolic approximation for the sphere profile used in JKR theory can be no longer valid.

These models have varied applicability to particle-substrate and particle-particle adhesion problems but also can create following problems:

(a) the same model may not be valid at all length scales or under all conditions.
(b) applicability of some of these models need to be examined for sub-micron sized particles.

### 1.3.2 Numerical Modeling

The investigation of particle dynamics in a particulate flow or to estimate the force and deformation in collision in molecular length scale needs a lot of calculations. Quesnel et al. [12,13] evaluated the Poisson's ratio and elastic constants for an FCC lattice interacting via the Lennard-Jones potential. A first principle approach [14] was developed to the problem of particle adhesion. Molecular dynamics modeling was used to

calculate the changes in the energy between two surfaces when surfaces approach one another and subsequently separate. The interfacial energy between two surfaces is reported. Energy loss mechanisms in the presence of elastic deformations are modeled. Finally, defects such as surface roughening and defect formation upon separation are proposed. Molecular dynamics simulations were also used by Quesnel et.al. [15] to study the interaction between two dimensional nano sized particles and the surface of a two dimensional crystal composed of the same molecules. The particle and the surface were found to deform before, during and after the impact. The surface forces were found to be sufficiently large to prevent particles from separating from the substrate after the collision. The excess energy generated an acoustic wave and lattice defect.

Smith et al.[35] used MD simulation to simulate particle-substrate collision. The physical state of surface after collision interaction was found and any surface damage was also detected. The result of particle impacts depends on the energy, incidence angle of the projectile and the substrate surface.

The following chapter has results for the collision and adhesion of three dimensional particles obtained by the direct numerical simulations of the collisions. We have also attempted to use our simulations to systematically quantify the role of parameters such as the potential energy between the molecules, number of molecules forming particles, relative orientation of crystal planes in particles and approach velocity in the collision process.

Larger scale modeling like particle scale modeling is done by Walton [16] for numerical simulation of inclined chute flows of monodisperse, inelastic, frictional spheres. Molecular dynamics like simulations are utilized to map regions of flow

parameter space where steady flow occurs for these spheres, flowing down frictional, inclined planar surfaces. Thornton et. al. [17] used the TRUBAL computer code, which uses DEM (discrete element method) to simulate the orthogonal impaction of monodisperse FCC and BCC agglomerates with a wall. The impaction of agglomerates colliding with each other is also presented. The computer simulations allow a microexamination of the process and the extraction of data both on the micromechanics of fracture and the resulting fragmentation. It is shown that the damage ratio is a function of Weber number, packing fraction and the primary particle to agglomerate size ratio. The effect of particle size and bond strength on impact breakage of agglomerates is checked by Thornton *et. al.* [18] using the same TRUBAL code, where particle interaction laws are based on theoretical contact mechanics and van der Waals adhesion forces determine the bond strength between individual particles in the assembly. A good agreement has been found between simulation results and experimental measurements. The effect of liquid bridge forces on agglomerate collisions is quantified by Thornton *et. al.* [19] using the DEM based TRUBAL code. Computer simulated normal collisions of two moist agglomerates each consisting of 1000 particles with a degree of saturation 0.71 % is performed. Unfortunately by doing experiments, it is difficult to obtain the micro-level quantities such as particle forces, velocities and packing geometries of the tested agglomerates. This simulation produces some preliminary results of the relative energy dissipated by viscous damping and plastic deformation of agglomerates in terms of micro-level properties of the pendular liquid bridges. A microscopic simulation of oblique collisions of wet agglomerates is also done by Thornton *et. al.* [20]. Each agglomerate consisted of 1000 particles with radii of $30\pm 3$ μm. At the incident angles

less than $45^0$, the agglomerates coalesce at small impact velocities while at high values coalescence is accompanied by attrition involving particle ejection. At the impact angle more than $45^0$, the two agglomerates do not coalesce and their shapes remained essentially unchanged. This oblique collision results in rupture of interstitial liquid bridges and also the formation of new bridges between neighboring particles. Such disturbances to the microstructure increase as the incident angle decreases and the trend may be described by cosine functions.

A new model has been developed by Thornton et. al. [21] to deal with capture and rebound of small particles from surfaces upon elastic-plastic impact. For the case of no surface adhesion, the plastic force displacement relationship is based on Hertzian theory while the JKR adhesion model is extended to investigate impact behavior which involves plastic deformation. Computer simulations have been performed to determine the coefficient of restitution over a wide range of particle impact speeds. The simulated results are compared with experimental finding. Thornton [22] proposed a simplified model for normal contact interaction between two elastic-perfectly plastic spheres. This model is also incorporated in TRUBAL in order to numerically simulate a sphere impacting orthogonally with a target wall. From the simulation, a relation between coefficient of restitution and impact velocity is developed. The analytical solution from the theoretical model is derived

## 1.4 Outline of the Thesis

The problem at the molecular scales is studied by conducting direct numerical simulations of the collision process using molecular dynamics simulation. In this

dissertation, MD simulations are done only for the nano sized particle, which is presented in chapter 2. The real energy requirement in particle-particle adhesion process is presented in chapter 3. The host particle scale and device scale modeling are presented in chapter 4. Each chapter includes concluding remarks and suggestions for future work.

# CHAPTER 2

# MOLECULAR SCALE MODELING

In MAIC process in order to investigate the processes happening at multiple length and scale the modeling at the guest particle scale level or the smallest scale is considered as the initial task of the dissertation. The guest particles are of nanometer size and so the length scale has been chosen as that of the molecule, the basic unit of building up the particle. The head on and oblique collision of nanoparticles are modeled.

## 2.1 Direct Numerical Simulation of Smaller Nanoparticles

The mechanics of collision between two identical spherical particles in a three dimensional space is simulated by conducting molecular dynamics simulations. Specifically, both the particles are assumed to be made up of Argon molecules that interact with each other via the Lennard-Jones potential. Argon is successfully used to model any solid state material by MD simulation. Argon's structure is very simple as it is an inert gas and it has melting point of 80 K. The particles are given initial velocities such that they perform head on collision. Herein, we will present our preliminary results only for the particles of diameters of the order of 10-50 nm.

The Lennard-Jones potential $\phi$ is given by

$$\phi = -4\,\varepsilon\left[(\sigma/r)^6 - (\sigma/r)^{12}\right] \qquad (1)$$

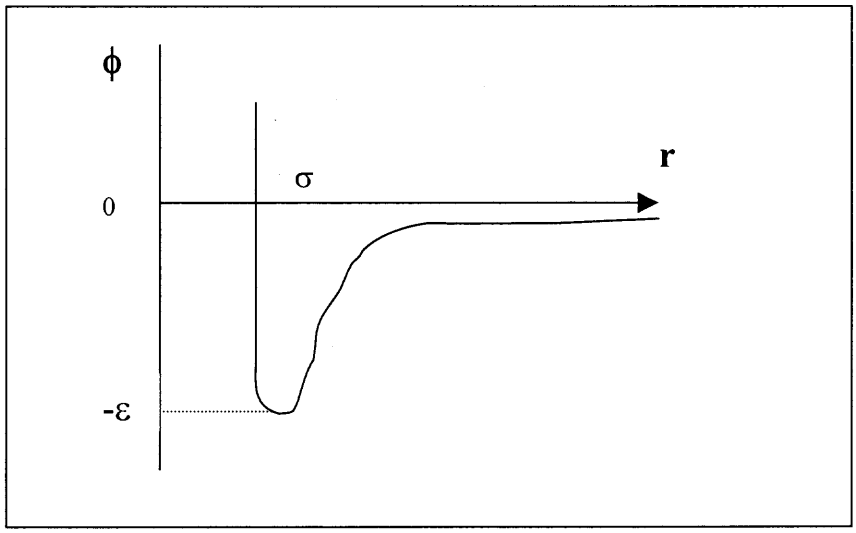


**Figure 2.1** The Lennard-Jones potential.

where $\varepsilon$ is the binding energy, and $\phi(r) = 0$ at $r = \sigma$ where $r$ is the distance between the molecules. The values of constants $\varepsilon$ and $\sigma$ are given in table 2.1. The molecular trajectories are obtained by integrating Newton's equation of motion:

$$m_i \frac{d^2 r_i(t)}{dt^2} = - F_i \tag{2}$$

$$F_i = - \frac{\partial \phi(r_i, \ldots, r_N)}{\partial r_i} \tag{3}$$

where $F_i$ (t) is the force acting on the i-th particle at time t. The simultaneous integration of (2,3) is done by using a second order finite difference scheme. The time step used in the numerical scheme is 0.075 femtoseconds.

**Table 2.1** Physical parameters of argon. [14]

| Parameter | Symbol | Value |
|---|---|---|
| Mass | m | $6.624 \times 10^{-26}$ Kg/molecule |
| Energy | $\varepsilon$ | $1.725 \times 10^{-21}$ Joule/molecule |
| Distance | $\sigma$ | $3.44 \times 10^{-11}$ meter |

The particles modeled as spheres, are constructed by placing the Lennard-Jones molecules in the FCC lattice positions within the sphere. The two particles thus obtained are placed at a distance of 200 dimensionless units(scaled by $\sigma$) from each other where they are allowed to equilibrate to an equilibrium kinetic energy of 0.0125 $\varepsilon$ per molecule. .The particles are kept apart to ensure that they do not deform or influence each other. The calculations are started by placing these two particles in their equilibrated configurations at a distance of 2 or 4 dimensionless units and giving them an initial relative velocity of $1.816 \times 10^{11}$ dimensionless units. In the present calculations the first particle on the left hand side taken to be in rest and the second particle on left hand side is moved towards the first particle with the given velocity. The collision mechanics between particles of six different sizes was studied. The particle sizes were changed by taking the number of molecules as: 152, 240, 312, 336, 532 and 1004. The dimensionless time $\tau = t / 7.5 \times 10^{-15}$ where t is in seconds.

A systematic study to check the effect of size, initial relative velocity and the orientation of the particles on the relative velocity of the center of mass of the particles

after collision is done with same sort of direct numerical simulations. Both heads on collision and oblique collision cases are simulated.

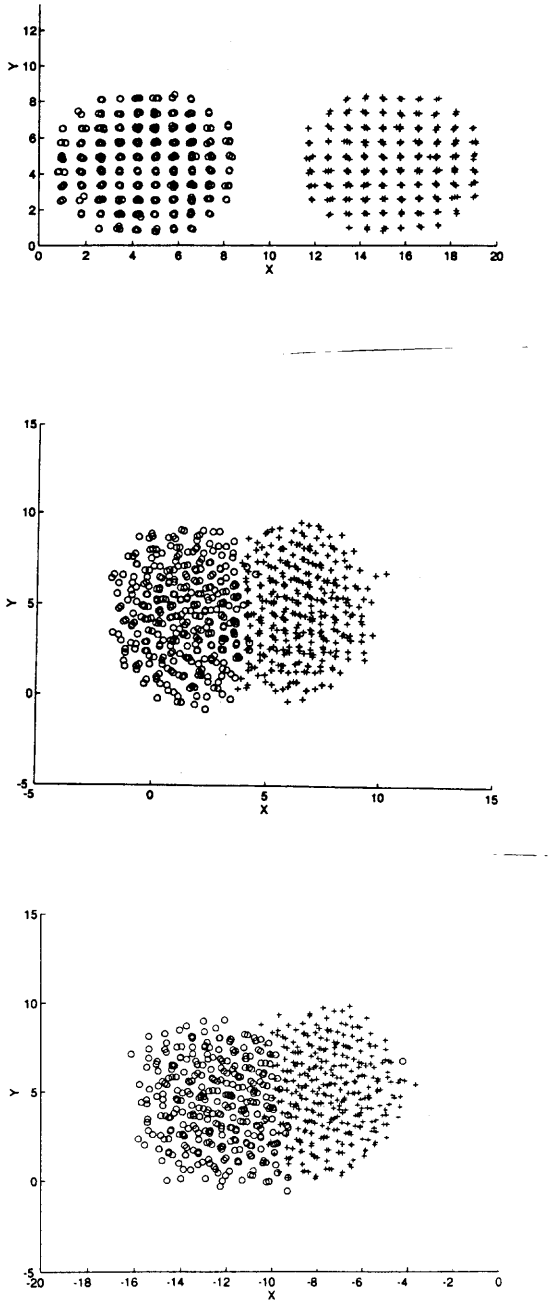


**Figure 2.2** The instantaneous configuration of two colliding particles at $\tau$ = 1, 4000, 8000. Each particle has 336 molecules.

### 2.1.1 Head on Collision

Figure 2.2 shows the instantaneous configuration due to head on collision of particles where each particle is made by 336 molecules. A two-dimensional projection of the molecular positions is plotted to show the particles trajectories and deformation during collision. The particles are symmetric to each other as the lattice planes of both the particles are parallel. At $\tau = 0$, the relative velocity is given to the second particle. The particles come in contact at $\tau = 4000$, after which they move in unison in the negative x-direction. The particles are seen to be melting or merging. For all cases studied, we found that the particles fuse together after collision.

**2.1.1.1 Effect of Orientation:** The orientations of the lattice planes are changed keeping the size and initial relative velocity of the particles to be same. Each particle has 336 molecules. The cases where planes are parallel and the planes are rotated so those are mirror reflections are examined.

In figure 2.3 the initial configuration of the two particles is set asymmetrical by rotating the second particle $30^0$ about the Z-axis. At $\tau = 0$, keeping the left side particle stationary, the right side particle is given the same mentioned relative velocity. The particles are in contact at t $\tau = 4000$ and they have started oscillating towards the negative and positive x-directions. At $\tau = 15000$ the particles are adhered and moving in the negative x direction. The small fluctuations in their relative velocity are indicative of wave propagation within the particles (see figure 2.4). These fluctuations, as expected, diminish with time. Their trajectory is observed till 1.5 million time steps and they are found to be behaving similar with decreasing fluctuation of velocities of both of the

particles. For all of the mentioned cases we found both the particles sticking or adhering to each other after collision, oscillating and moving along the negative x-direction, *i.e.* the direction of the relative velocity.

The projections onto both the xz- and xy-planes show that a sound wave is produced during impact which then propagates through the particles (see Figure 2.5); the number of molecules forming the particles is 336. The interface between the two particles appears to lose its lattice structure as the sound wave propagates inwards, but the remaining part of the particles remains almost undisturbed. Both views show that the disturbance is concentrated around the contact region and the regions away from the interface maintain their lattice structure.

To check the effect of orientation, a different initial lattice structure is created within the particles by rotating both of them by the same angle along z axis but in opposite direction. That makes the lattice planes of one particle just the mirror reflection of the same in the other particle, shown in Figure 2.6 at $\tau = 1$. Then the same relative velocity is given to the second particle. The number of molecules in each particle is 336. The particles after colliding stick together and move towards the negative x direction as shown in the Figure 2.6 for $\tau = 5000$ and 10000. No merging or melting of particles is observed. Acoustic waves are generated after collision.

**Table 2.2** The scaling parameters used in MD simulations.

| | Distance | Velocity | Time |
|---|---|---|---|
| Scaling parameter | $3.44 \times 10^{-10}$ m | $3.44 \times 10^{-10}$ m/s | $7.5 \times 10^{-15}$ s |

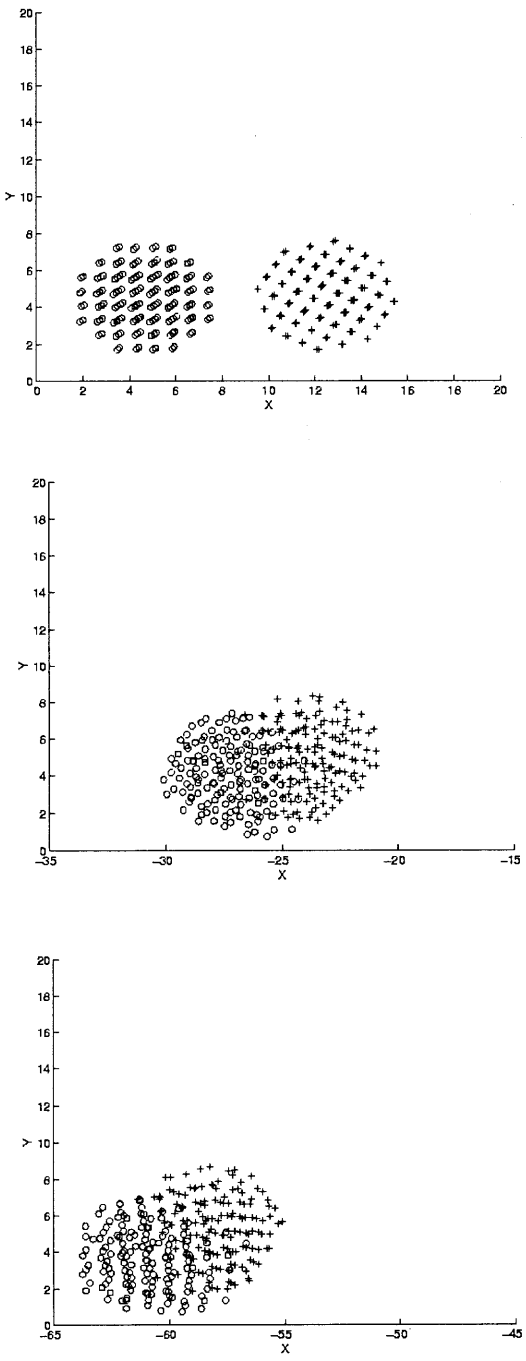


**Figure 2.3** The particle positions at $\tau$ = 1, 4000, 15000, where each particle has 336 molecules.

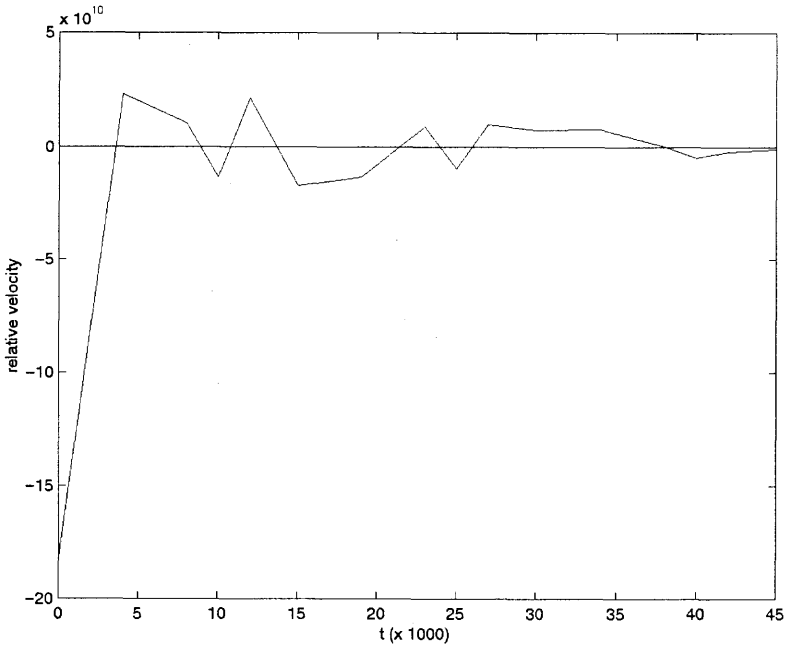


**Figure 2.4** The plot shows the variation in relative velocity when each particle has 336 molecules.

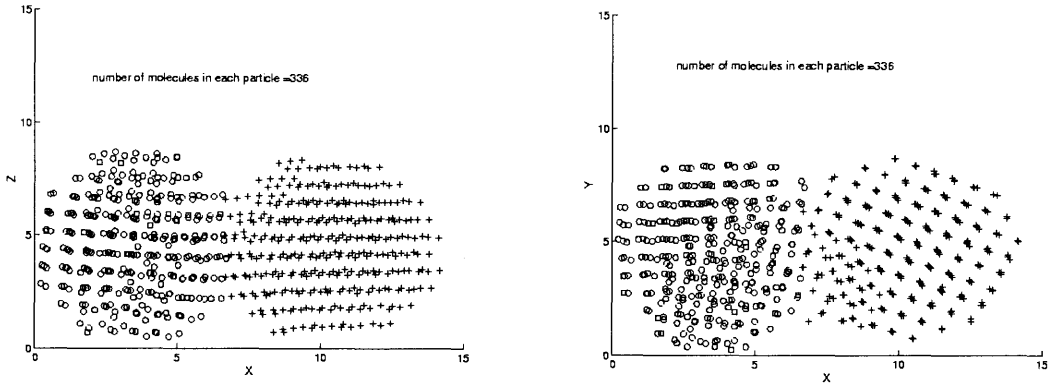


**Figure 2.5** The views through Z and Y axes to the particle position at t = 4000. Each particle is made of 336 molecules.

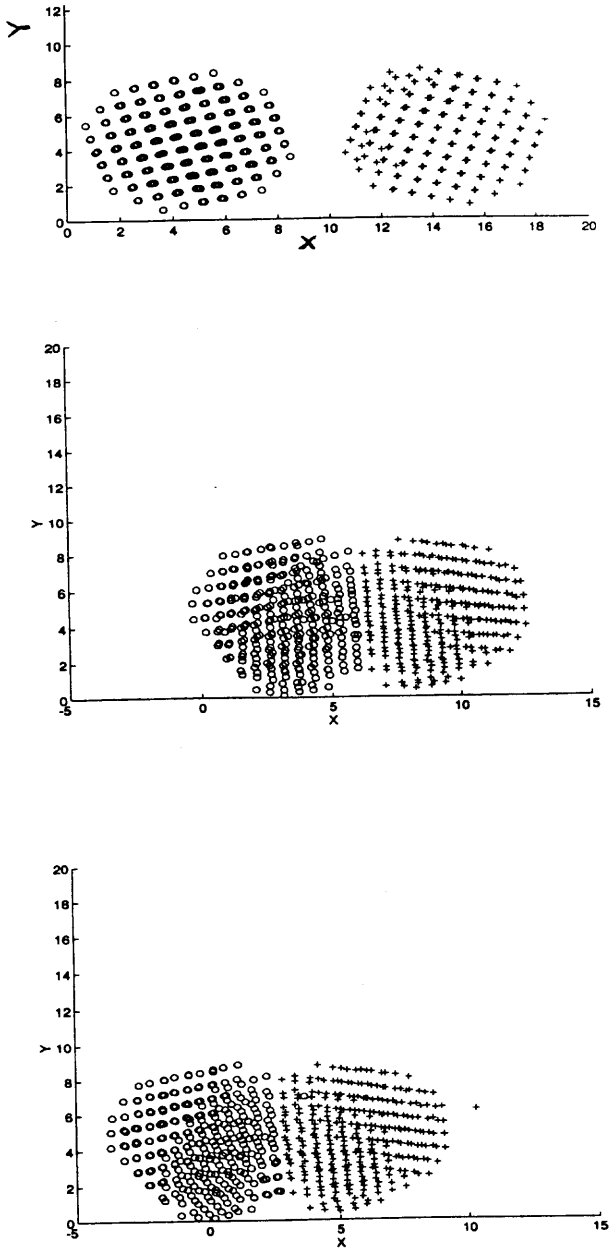


**Figure 2.6** The particle positions at $\tau$ = 1, 5000, 10000. Each particle has 336 molecules and mirror reflection to the other.

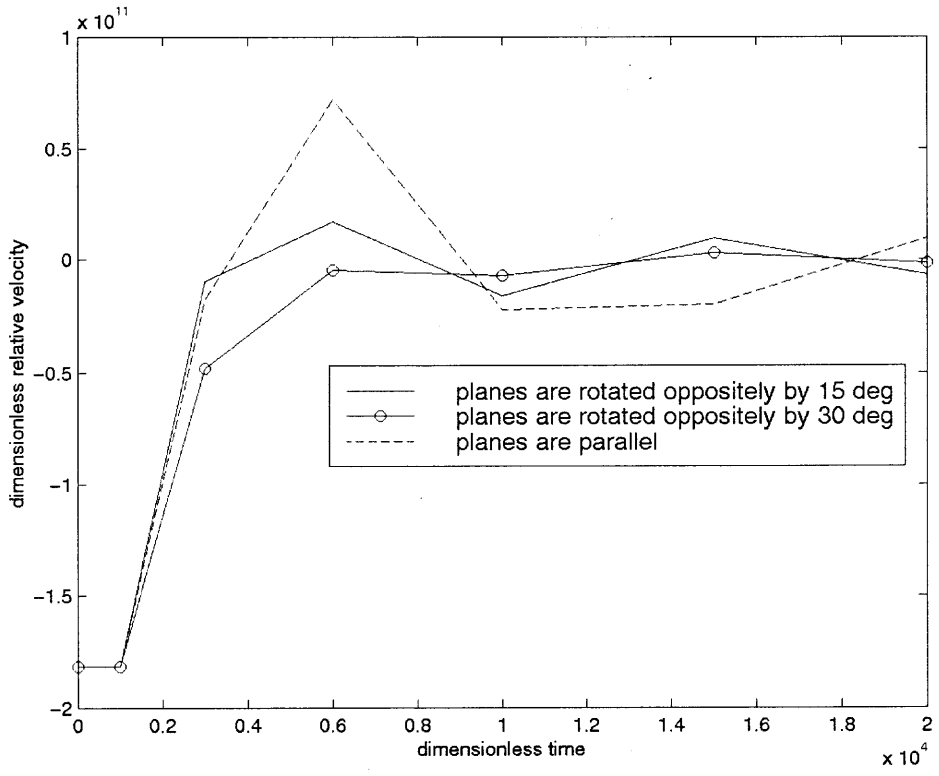


**Figure 2.7** Variation of relative velocity with time at different orientations of lattice planes.

The variation of relative velocity after collision is estimated with the change of lattice orientation. The lattice planes are rotated by $15^0$ and $30^0$. Both of the particles rotate in opposite direction but by same angle. Figure 2.7 shows the variation of dimensionless relative velocity with dimensionless time at different orientations. It is observed that the oscillations decrease with the increase of angle of rotation.

**2.1.1.2 Effect of Initial Relative Velocity :** The effect of the relative velocity is checked with the case where only the second particle is given the z rotation. The second particle is given a relative velocity which is five hundred times the usual value. The projection of

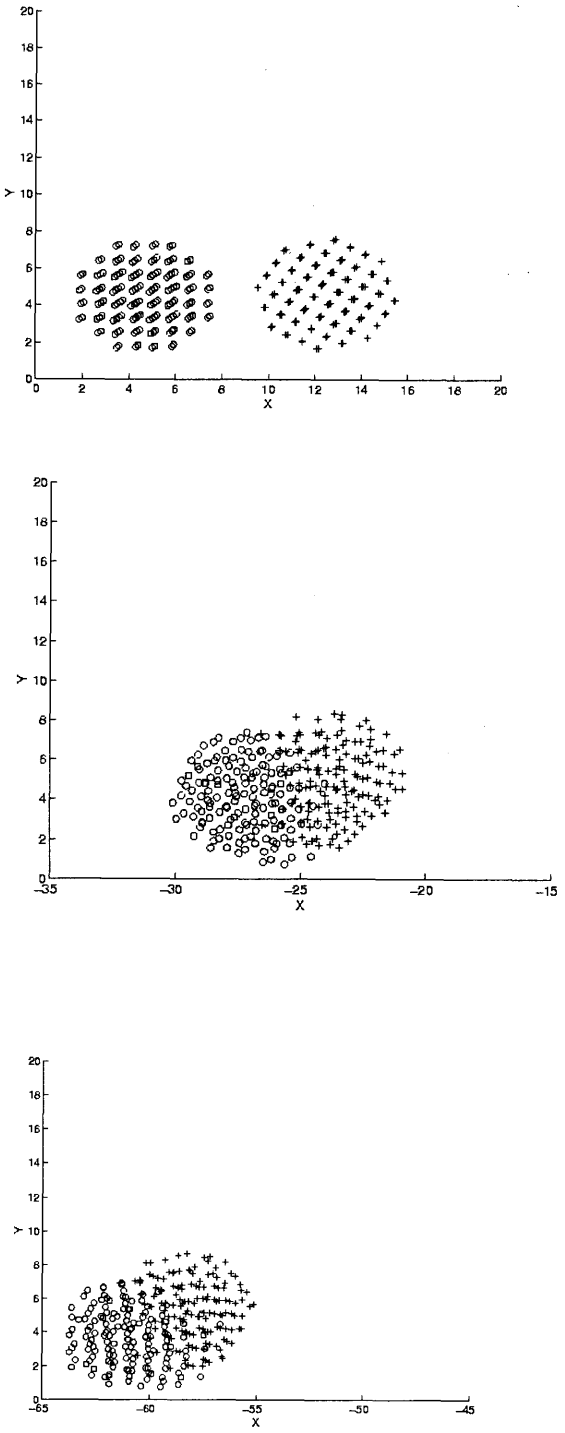


**Figure 2.8:** The particle positions at $\tau$ = 1, 4000, 15000. Each particle has 152 molecules.

particle position on the xy plane is shown in Figure 2.8. Each particle is made of 152 molecules. At $\tau = 1$, the relative velocity is given. At $\tau = 4000$, the particles are already melted after the collision, as they jointly move towards the negative x direction. At $\tau =$ 15000 more melting and breakage of lattice structure is evident.

The 3D particles made up of 240 molecules are collided with different initial relative velocities where the second particle(made of + sign) is rotated by $30^0$ about Z axis before the initial velocity was given. In figure 2.9 dimensionless relative velocity is plotted against the dimensionless time at different constant initial relative velocities. It is observed for velocities of second particle equal and more than $1.8\times10^{10}$ the oscillations in the relative velocity of the center of mass of the two particles decrease with increase of velocity of second particle. If the initial relative velocity of the particles is less than the said value the oscillation decreases with decrease in the velocity. Figure 2.10 shows the above mentioned phenomenon where dimensionless relative velocity is the ordinate and dimensionless time is the abscissa. The variation of relative velocity is shown at two constant initial relative velocities which are less than $1.8\times10^{10}$.

**2.1.1.3 Effect of Size:** The sizes of the 3D particles ( where the planes are at an angle of $30^0$) are changed by changing the number of molecules necessary to create the particles. As the size increases the oscillation in the relative velocity decreases. The numbers of molecules considered are 142, 240, 336 in each of the particles. Figure 2.11 shows the variation of relative velocity with respect to the number of the molecules involved.

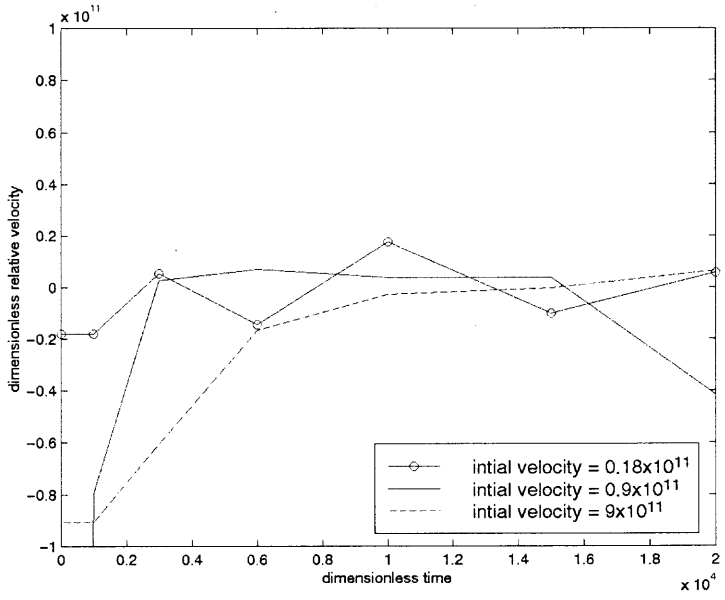


**Figure 2.9** Variation of relative velocity with the time at different constant initial relative Velocities.

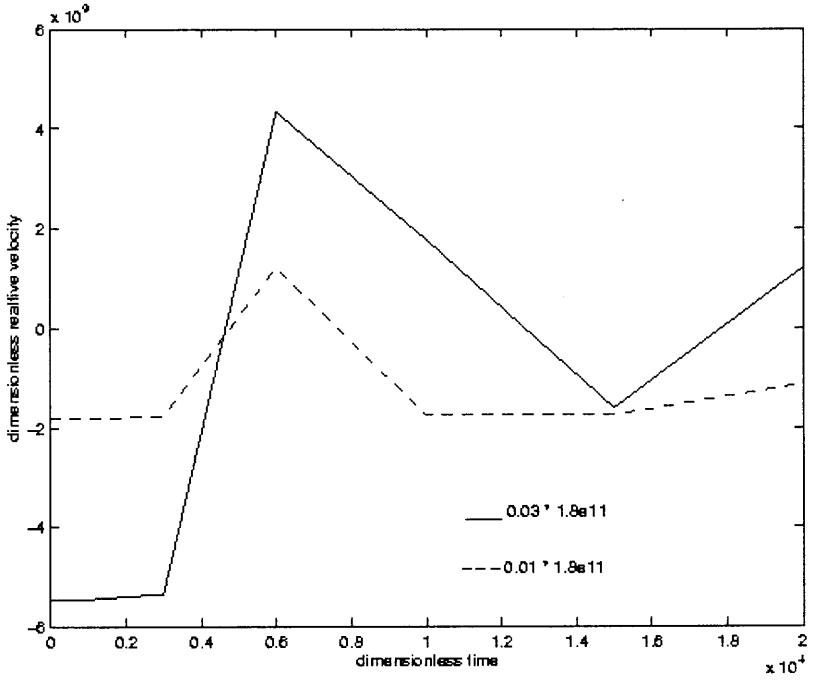


**Figure 2.10** Variation of relative velocity with time at different constant initial relative velocities.

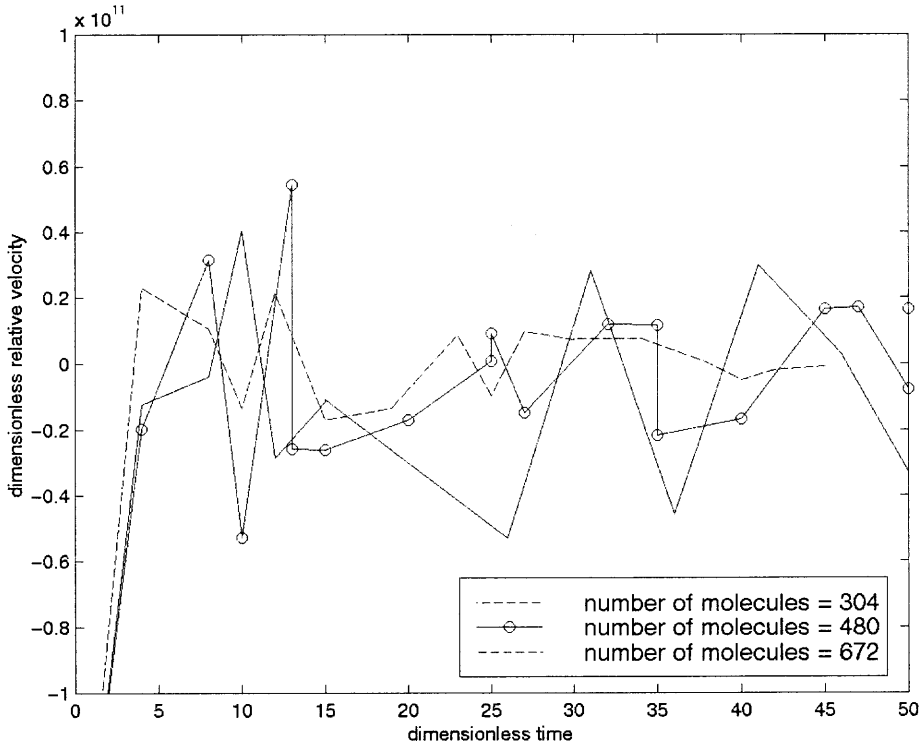


**Figure 2.11** Variation of relative velocity with time at different constant sizes of particles.

### 2.1.2 Oblique and Offset Collisions

3D particles made up of Argon are used to undergo similar MD simulations where the parameters like number of molecules, initial relative velocity and the orientation of the lattice plane are systematically varied. Different offset positions of the y coordinate of the center of mass of the particles are used.

**2.1.2.1 When the Offset = 0.25 D :** When the particles each made of 336 molecules are collided with the relative velocity of 1.8 x $10^{11}$ they stick after collision and continue to rotate in clockwise direction. Figure 2.12 shows this phenomenon where the particles stick and rotate for less relative velocity. The planes of the particles are parallel. The projections of particle positions in xy plane at different time intervals are plotted in the four graphs in figure 2.12.

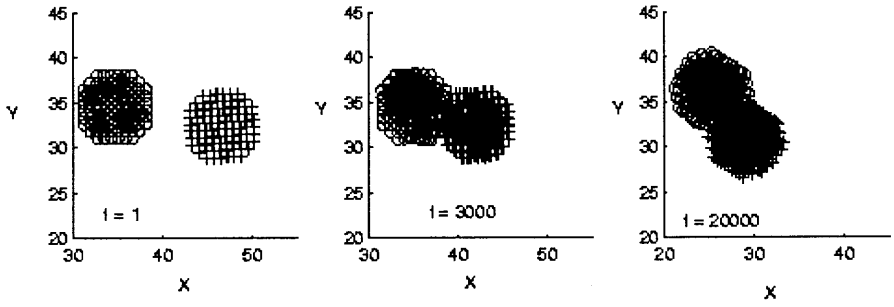


**Figure 2.12** Particle positions at $\tau$ =1, 3000, 6000, 10000, where the offset = 0.25 D.

These plots are at $\tau$ =1, 3000 and 20000. This sticking and rotation without any merging of particles take place for any orientation of the lattice planes between two of the particles. But if the velocity is increased ten times of the earlier cases the particles used to merge and melt within themselves. In figure 2.13 the particles are seen to be merged for higher

velocity. The particle positions at τ =1 and 6000 are shown. The lattice planes of the two particles are parallel.

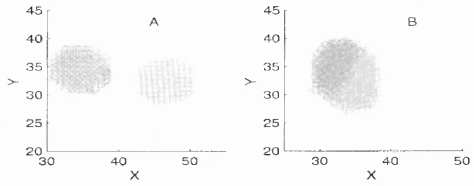


**Figure 2.13** Particle positions at τ =1, 6000 where offset = 0.25 D and the initial relative velocity is higher.

**2.1.2.2 Where the Offset = 0.75 D:** When the velocity is 1.8 x $10^{11}$ then the behaviors of the particles are just same as the above case as the particles collide and rotate clockwise. Figure 2.14 shows the case where number of molecules in each particle is 336 and the planes are parallel. The xy plane projection of the positions of the particle is shown in the 3 graphs. The positions are at time t =1, 10,000 and 20,000. The same phenomenon occurs for any orientation of the lattice planes. But if the velocity is increased to 10 times of the earlier case, the particles after colliding get separated instead of sticking to each other. They get detached with some of molecule transfer from one particle to the other (located at the surface) and also formation of a very small particle or agglomerate made of both types of molecules

(shown in figure 2.15). The projection of particle positions on xy plane are shown at time t = 1, 6000 and 10,000. The particles after separation remain rotating in the clockwise direction.

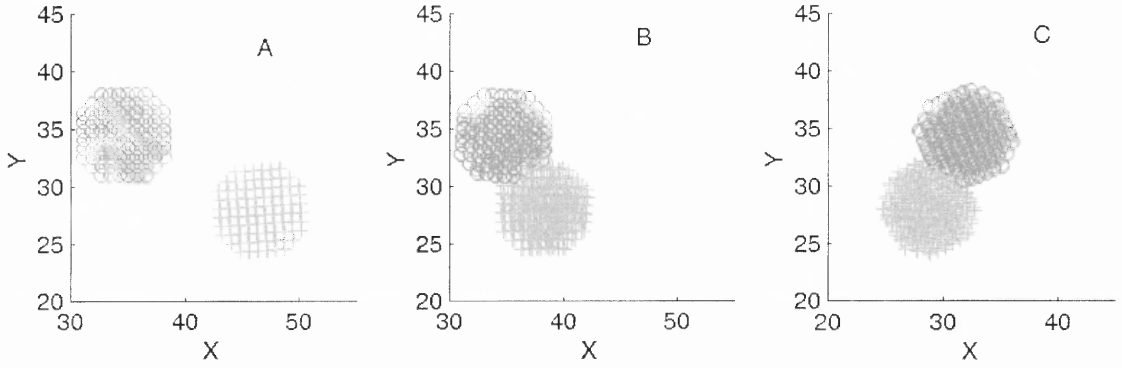


**Figure 2.14** Particle positions at τ =1, 10000, 20000 where offset = 0.75 D.

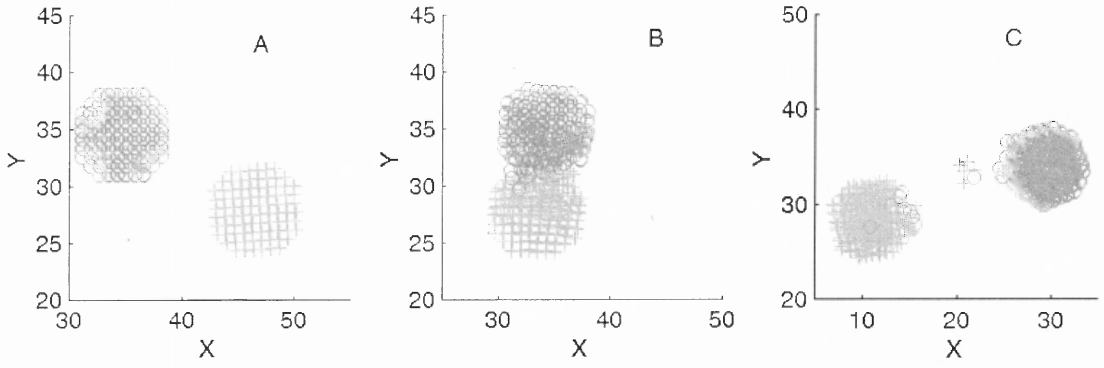


**Figure 2.15** Particle positions at τ =1, 6000, 10000 where the offset = 0.75 D and the relative velocity is 10 times higher.

So the offset play a major role in the collision determining whether the particles will stick or bounce off at a definite range of initial relative velocity.

**2.1.2.3 The Effect of Initial Relative Velocity when Offset is Fixed:** Here the offset is kept fixed to be 0.75 D and the particles each made of 336 molecules (and with parallel lattice planes) are collided with different initial relative velocities. Figure 2.16 shows the variation of dimensionless relative velocity with respect to dimensionless time at different constant initial relative velocities. This figure demonstrates how with the increase of initial relative velocity the oscillation increases till the value of initial relative velocity = $5 \times 1.8 \times 10^{11}$. As the initial relative velocity is increased to $10 \times 1.8 \times 10^{11}$ the oscillation decreases.

**2.1.2.4 Effect of Orientation when Offset is Fixed:** The same particles that were mentioned above were given rotation in different ways and collided with the initial relative velocity of $1.8 \times 10^{11}$. In figure 2.17 it is shown that the oscillations are more or less same whatever might be the angle between the planes. The cases where planes are parallel, at an angle 30, mirror reflection after rotation of 15 and 30 degrees are simulated.

**2.1.2.5 Effect of Size When Offset is Fixed:** The sizes of the particles are just increased while keeping the lattice plane parallel and the offset fixed. The initial relative velocity is fixed to be same of earlier case ($1.8 \times 10^{11}$). In figure 2.18

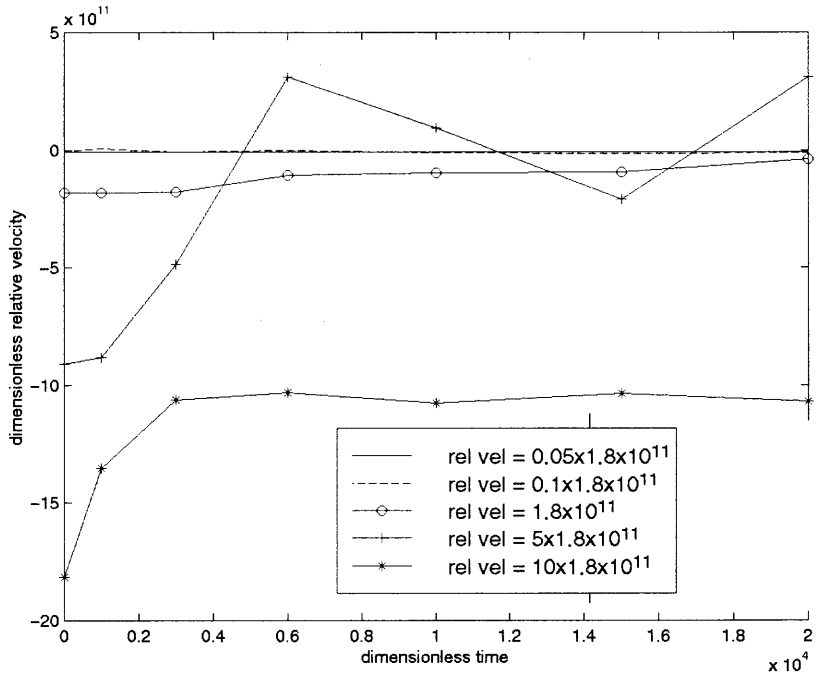


**Figure 2.16** Variation of relative velocity with time at different constant initial relative velocities.

it is evident that the oscillations decrease with the increase in particle size. Here particle size increases as the number of molecules present in each particle is changed. The numbers of molecules tried here are 152, 240, 336.

**2.1.2.6 When the Offset = 1.2 D:** The 3D particles are kept at an offset of 1.2D with their lattice plane parallel and the initial relative velocity is varied. When the initial relative velocity is less than or equal to $1.8x10^{11}$, then the particles become attached while passing each other. If the velocity is 10 times higher than $1.8x10^{11}$, the particles just pass each other without sticking to each other. In figure 2.19 it is shown the particles made of 336 molecules and plane parallel

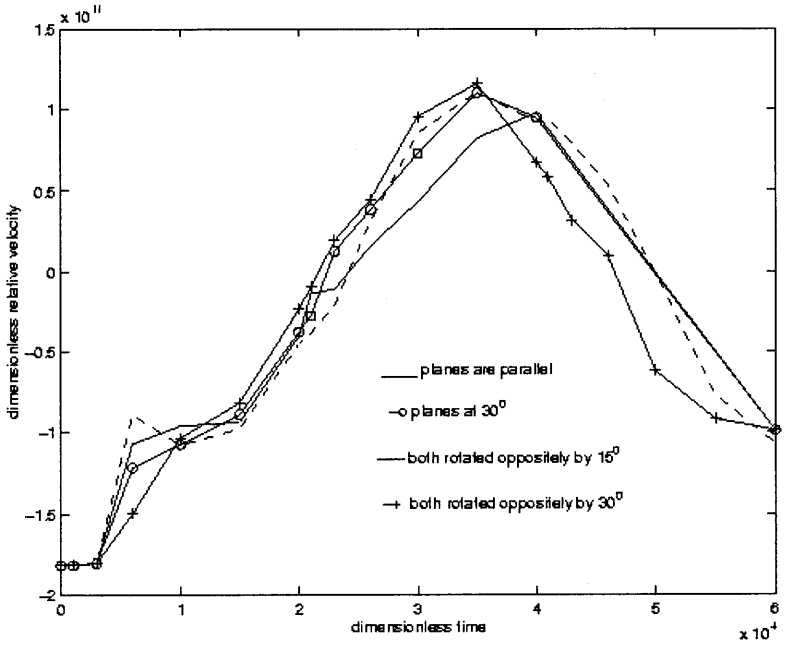


**Figure 2.17** Variation of relative velocity with time at different orientations of the lattice planes.

are brought closer by the relative velocity of $1.8 \times 10^{11}$. The 3 plots show the projection of the positions of the particle on xy plane at $\tau$ = 1, 10000,25000. The particles are getting attached while passing by the Lennard-Jones attractive force. If the velocity is increased by ten times we can see the same particles do cross each other instead of getting adhered (as shown in figure 2.20 for $\tau$ =1, 6000).

As it is observed that the higher velocity and offset has an effect on the sticking and non-sticking in particle collisions, a systematic study has been carried out changing the binding energy $\varepsilon$ in the model with the initial relative velocity to determine the critical initial velocity needed for the transition from sticking to non-sticking condition of the particles.

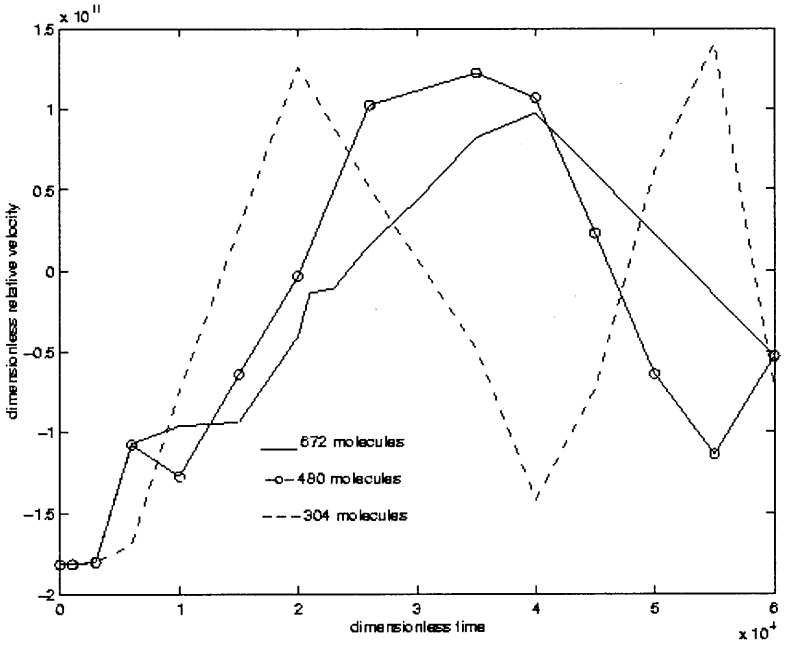


**Figure 2.18** Variation of relative velocity with time at different particle sizes.

The following table shows the variation of critical initial relative velocity with the binding energy used in the Lennard-Jones model.

**Table 2.3** The binding energy of LJ potential and the corresponding critical velocities.

| Binding energy(ε) (J/molecule) | Crit. Vel (non dimensional) | Original critical vel(m/s) |
|---|---|---|
| $1.725 \times 10^{-21}$ | $2 \times 1.8 \times 10^{11}$ | 3.723 |
| $1.725 \times 10^{-21} \div 5$ | $0.25 \times 1.8 \times 10^{11}$ | 0.465 |
| $1.725 \times 10^{-21} \div 10$ | $0.9 \times 1.8 \times 10^{11}$ | 1.675 |
| $1.725 \times 10^{-21} \div 100$ | $0.9 \times 1.8 \times 10^{11}$ | 1.675 |

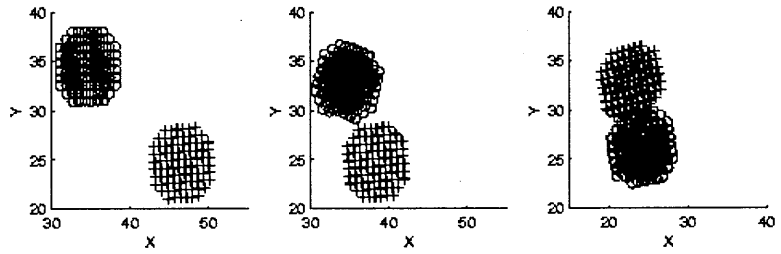


**Figure 2.19** Particle positions at t =1,10000,20000 where the offset is 1.2 D.

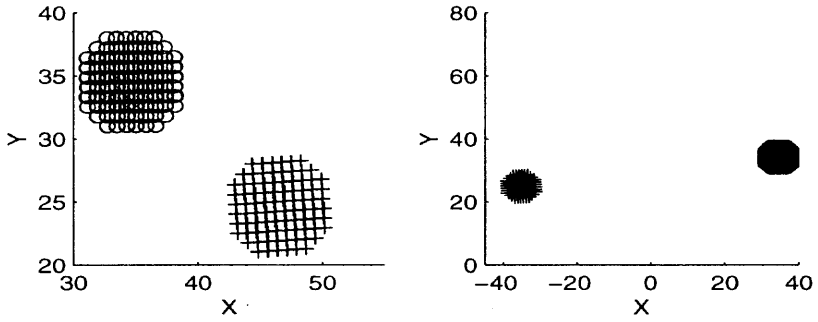


**Figure 2.20** Particle positions at t = 1,6000 when the offset is 1.2 D but the initial relative velocity is 10 times higher.

## 2.2 Comparison of MD Simulation with Models of Adhesions

In order to investigate and compare the mentioned molecular level model with existing models in literature of particle adhesion, an effort has been made to try to simulate two particles under van der Waals force. JKR, DMT, MP theories are applicable for particles bigger than the micron range, whereas van der Waals force is the elementary level force

which acts between two atoms. Here we tried to compare the MD simulation results with van der Waals theory and JKR theory.

Two Lennard-Jones almost spherical particle of diameter 2.5 nm is formed and kept close enough ( $4\,\mathring{A}$ ) to experience the van der Waals force. Each particle contains 336 molecules of Argon. No external force or velocities are given to the particles.

It is observed that the van der waals force brings the particles together and they maintain the attached state until 5000 dimensionless time. In Fig. 2.21 the projection of the position of the two particles(marked with 'o' and '+' signs) in XY plane is shown at $\tau$ = 5000. It is observed that the particles after coming in contact remain experiencing the adjustments of the molecules inside themselves. Molecules near the interface are more disturbed than the molecules on the other part of the spheres.

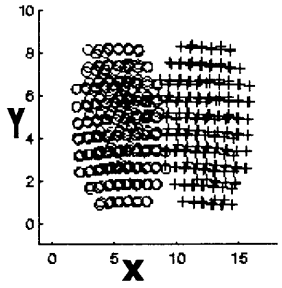


**Figure 2.21** Two nanoparticles are stuck with each other under van der waals forces.

The temperature of the particles( calculated from their kinetic energy ) increases with the time as they come in contact in a fluctuating manner. After $\tau$ = 3000 the temperature gets stabilized ( shown in Fig2.22). In Fig 2.23 the x-coordinate(dimension less) of the mass centers of the particles are plotted with respect of

dimensionless time. At $\tau = 0$ the particles are approximately $4\,\mathring{A}$ apart. The van der waals force of attraction bring them in contact at approximately $\tau = 200$. Then the particles continue their contact with oscillatory trajectories.

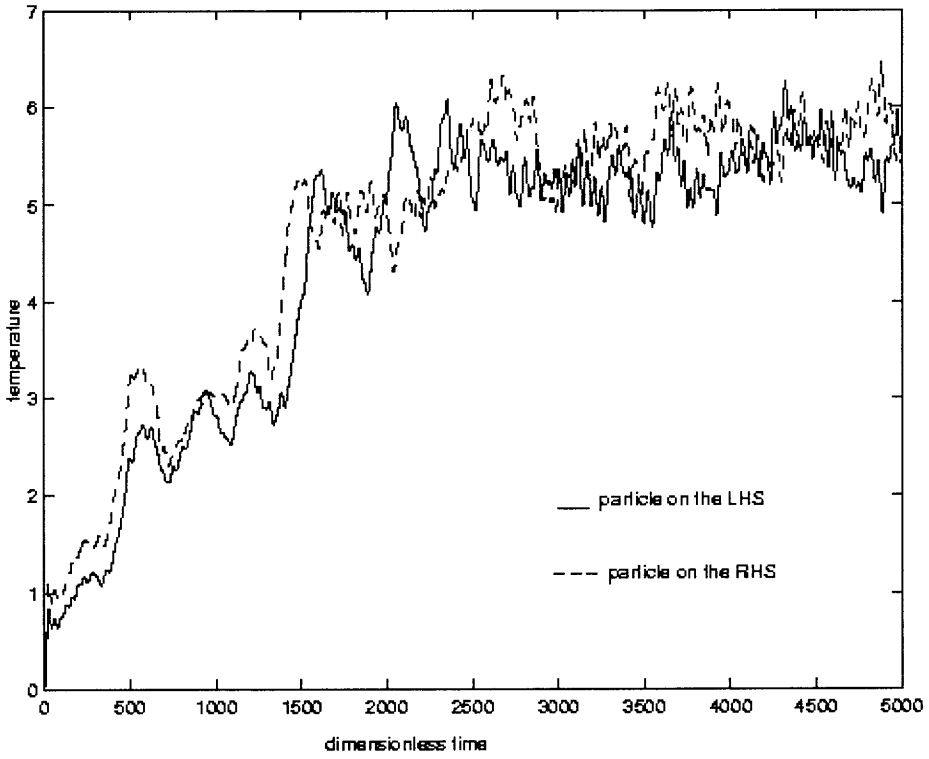


**Figure 2.22** The temperatures for 2 particles under van der Waals force.

The van der waals force F is defined to be:

$$F = \frac{AR}{12D^2} \tag{4}$$

where A is the Hamaker's contant ; R is the radius of the spherical particle and D is the distance between two particles. As in the simulation, the average normal force between

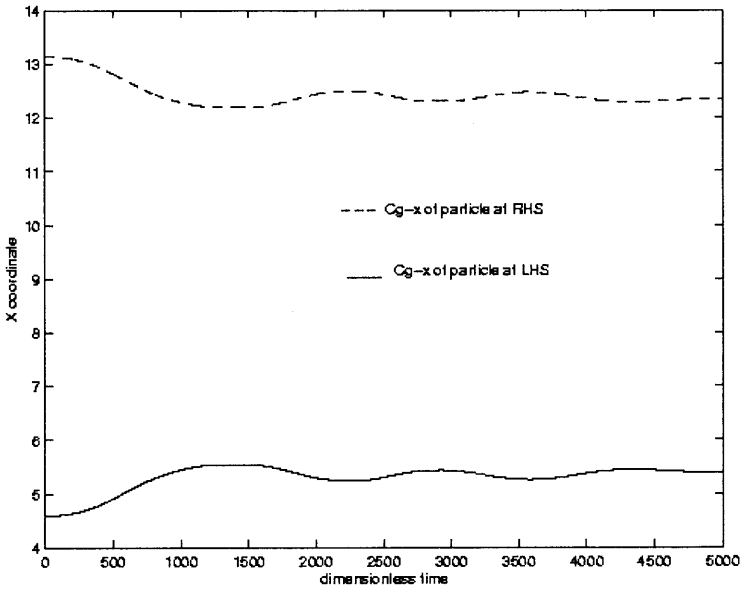


**Figure 2.23** The change of abscissa of the center of gravity of the particles(on right and left-hand sides) with dimensionless time.

the spheres( x component of the dimensionless force acting between two) is evaluated to be 1.35 dimensionless units in the time span of $\tau$ equals to 1 to 200. So the dimensional force is approximately $7 \times 10^{-12}$ N. In order to verify the simulation results it is necessary to calculate force using the equation (4).The Hamakers constant of solid argon is not available from the literature. But the Hamakers constant is related to the surface energy of the solid argon by the relation given by Israelachvili [23] as $\gamma = A/(24\pi d_o^2)$ ,$d_o$ is the interfacial contact separation and if we put all the parameters for argon then

$$A = 2.1 \times 10^{-21} \times \gamma \qquad (5)$$

The surface energy $\gamma$ for solid Argon is 43 erg/cm$^2$ , so $A = 9.03 \times 10^{-20}$ J. Then the vand der Waals force from equation (4) is calculated to be $58 \times 10^{-12}$ N which is more than what is obtained from MD simulations but in the same order of magnitude.

JKR theory proposes that in the absence of external load the diameter of the area of contact is related to the work of adhesion of the material ($w_A$) , radius R and a parameter K related to the mechanical properties of the material by the following equation:

$$a_o^3 = \frac{6\pi w_A R^2}{K} \qquad (6)$$

and $$K = \frac{4}{3\pi(k_1 + k_2)} \qquad (7)$$

where $$k_i = (1-\gamma_i)/\pi E_i \qquad (8)$$

here $\gamma$ and E are the Poisson's ratio and Young's Modulus of the material. For solid Argon Poisson's ratio ($\gamma$ ) = 0.347 and Young's Modulus (E) = $2.58 \times 10^9$ Pa. As in this case two spheres are made of same material, $k_1 = k_2 = 2.64 \times 10^{-11}$ . Now using equation (7) K is calculated to be $2.643 \times 10^9$, and finally from equation (6) the diameter of the area of contact is 0.77 nm . The diameter of contact from the Fig 2.21 is approximately 1.1 nm. A considerable difference in the values of the diameter is expected as JKR is applicable for particles in millimeter size range.

## 2.3 Simulation of Relatively Bigger Particles

To perform the same sort of direct numerical simulation of bigger particles, *i.e.* for D~ 1μm, more number of molecules has to be used to create the particles. The earlier computer program where the force was calculated by adding the contributions of all other particle thus could not be used because of the relatively large memory and simulation

time requirements. The force is therefore calculated using the so called chaining mesh[24] which exploits the fact that the Lennard-Jones potential is short ranged, and thus the contribution of the particles that are far away to the force is negligible.

The total short-range part of force on a particle i at position $x_i$ is given by the sum of the interparticle short-range forces

$$F_i^{sr} = \sum_{j=1}^{N_p} f_{ij}^{sr} \qquad (13)$$

The elementary method of evaluating $F_i^{sr}$ is to sweep through all the particles j = 1,2,,3...$N_p$, test whether the separation $r_{ij} = | x_i - x_j |$ is less than $r_e$, and, if so, compute $f_{ij}^{sr}$ and add it to $F_i^{sr}$. Such an approach is clearly impractical, because for each of the $N_p$ values of i one would have to test $N_p$ - 1 separation $r_{ij}$ giving an operation's count scaling as $N_p^2$.

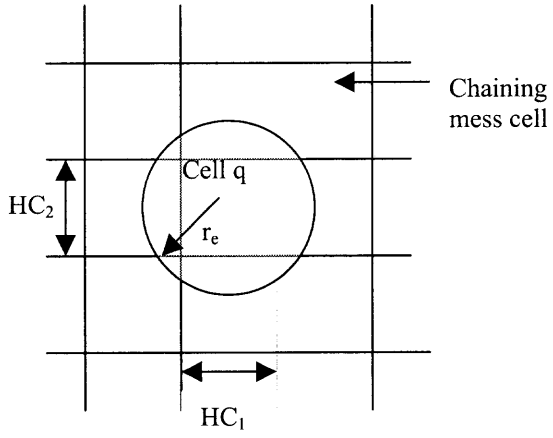


**Figure 2.24:** In the short-range force calculation, the computational box is divided into chaining cells. Contributions to the force $F_i^{sr}$ on particle i in cell q are nonzero only for particles j in cell q and the neighboring cells.

### 2.3.1 The Chaining Mesh

The computational cost of locating those particles j which contribute to the short-range force on particle i is greatly reduced if the particle coordinates are ordered such that the tests for locating particles j such that $r_e \geq r_{ij}$ need only be performed over a small subset $N_n$ of the total number of particles $N_p$. $r_e$ is the cutoff or search radius. It is for the reason that the chaining mesh is introduced. The chaining mesh (in 3 dimensions) is a regular lattice of $(M_1 \times M_2 \times M_3)$ cells, covering the computational box (of side $L_1 \times L_2 \times L_3$) in much the same manner as the $(N_1 \times N_2 \times N_3)$ cells of the much finer charge potential mesh. The number of cells $M_s$ along the s direction is given by the largest integer less than or equal to $L_s / r_e$. Consequently, the lengths of the sides of the cells of the chaining mesh are always greater than or equal to the cutoff radius $r_e$.

The Figure 2.24. depicts a chaining mesh in two dimensions. Typically, the side lengths of the chaining mesh cells $HC_s$ are between three and four times greater than the side lengths $H_s$ of the cells of the charge potential mesh. The circle of radius $r_e$ centered on particle i in chaining cell q delineate the area in which particle j must lie if they are to have a nonzero contribution to $F_i^{sr}$. Since $HC_s \geq r_e$ for all s, it follows that those particles j which have nonzero contributions to $F_i^{sr}$ must either lie in the small cell q as particle i or in one of the eight neighboring cells. If the particle coordinates are sorted into lists for each chaining cell, then to find the force $F_i^{sr}$ on particle i involves approximately $9N_c$ tests, where $N_c = N_p / M_1 M_2$ is the average number of particles per chaining cell. Therefore, if Newton's third law is used the total number of tests in finding all the short-range forces is approximately $N_n N_p \cong 4.5 N_c N_p$ as compared with $N_p^2$ for the elementary

approach. Similarly, in three dimensions, sorting coordinates into chaining cells gives the number of tests $N_n N_p \sim 13 N_c N_p$.

### 2.3.2 The Linked Lists

For serial computers ( but not necessarily for vector or array processors machines) it is computationally more efficient to sort the coordinates addresses rather than the coordinates themselves. Address sorting is made possible by introducing the linked-list array LL. If we let HOC(q) be the head-of-chain table entry for chaining cell q, and let LL(i) be the link coordinate for the particle i, then the procedure for sorting coordinates into list for each chaining cells by means of address sorting is summarized as follows:

**1.** Set HOC(q) = 0 for all q.

**2.** Do for all particles i.

(a) locate cell containing particle

q: = int ( $x_1 / HC_1, x_2 / HC_2, x_3 / HC_3$)

(b) add particle i to head of list for cell q

LL(i): = HOC(q)

HOC(q): = i

In two dimensions, the third component of q and x are omitted. The speed and simplicity of creating the linked-list from the scratch make it pointless saving and updating them time step by time step. The whole sorting process requires only three real arithmetic operations per particle in three dimensions or two in two dimensions.

Once the HOC and LL tables have been filled, a zero entry in HOC(q) indicates that there are no particles in chaining cell q. A nonzero entry gives the address of the coordinates of the first particle in the list. The link coordinate of a particle either gives the address of the coordinates of the next particle in the list, or is zero to indicate the end of the list. Therefore, given HOC and LL, coordinates in each cell can be looked up without any searching.

The numerical simulation of two dimensional particles is done by this new approach. The number of molecules needed to simulate the collisions of the sub-micron sized particles ~50,000. The two identical particles, each containing 15208 molecules and the diameters of 0.05 μm, were placed at a distance of 200 dimensionless units from each other where they were allowed to equilibrate to an equilibrium kinetic energy of 0.0125 $\varepsilon$ per molecule. The lattice planes of the colliding particles are parallel to each other. The calculations were started by placing these two particles in their equilibrated configurations at a distance of 2 dimensionless units and giving them the initial velocity of $1.816 \times 10^{8}$ dimensionless units towards each other. Figure 2.25 shows the molecular positions, trajectories, and the interface shape during collision. For the left particle the molecules are shown as open circles, and for the right particle are shown using "+" symbol. The particles come in contact at t = 7000, which causes the molecules at the interface to be agitated, and then the two particles, join together. The particles remain joined after the initial impact at least up to $\tau$ =10000, the time interval for which the simulations were performed.

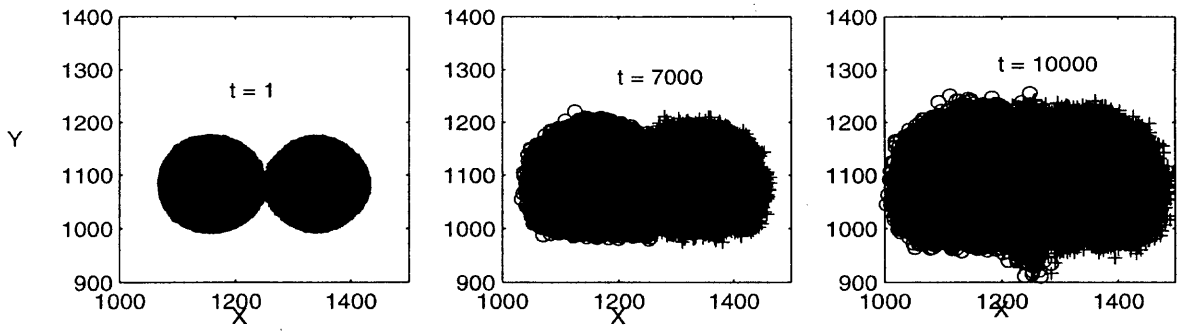


**Figure 2.25**: The particle positions at t=1,7000,10000 are shown.

## 2.4 Conclusions

The direct numerical simulations of the collision mechanics show that for the nano-sized particles factors such as the relative velocity, particles diameters, attractive potential strength, the relative orientations of the particles are important. The merging and melting of crystal structure increases with increasing relative velocity. Simulations show that when the crystalline planes for the colliding particles are parallel, the molecules near the surface mix, and this is not present when the crystalline planes are at an angle of 30 degrees. The effect of the mentioned parameters to the relative velocity of the particles after collision is also checked. The relative velocity is found to be less when the particles are bigger, the initial relative velocity is higher and the lattice planes are not parallel within two of the particles. Nanoparticles are seen to stick to each other in head on collisions. Oblique collisions are also tried where the particles bounce when there is an

offset of 0.75 D and the relative velocity is very high. In oblique collision the effect of orientation of plane is found to be not that important. But the size of the particle is important as the relative velocity of particles decrease with the increase in particle size.

The existing laws of adhesion as described in section 1.3.1, are not valid in submicron range. Therefore, the MD simulation is done on one hand to verify the laws of adhesion and on the other hand to come up with a new law or equation which is appropriate for submicron particle colliding with a micron size particle. However, the computation and memory requirements for submicron size particles, and their collision with even larger particles were prohibitive and hence were beyond the scope of the thesis. Thus the results presented here are preliminary and further work is recommended.

The MD simulation of the real material is another area of research. The MD of the collision of the real material can be tried with GULP[41] to check nano particle collision mechanics. During the course of the thesis, preliminary work has been done to develop the nano particles of alumina. However, more work is required to create stable alumina particles.

# CHAPTER 3

# EVALUATION OF DEFORMATION AND ENERGY OF ADHESION

In MAIC process the coating takes place for continuous and random collisions of the particles as the powder system attain a fluidized state. The guest particles collide with host particles and stick onto the host surface as an agglomerate. Later that host collides with other host or a magnetic particle so that the guest embedded and distributed on its own surface. In order to investigate the effect of the velocity of impaction (by which the guest approaches the host or vice-versa) the plastic deformation and the energy associated in the adhesion, the analytical model of Rogers et al.[10] is followed.

## 3.1 The Model of Particle-Surface Collision

The collision between two bodies is considered to take place in two stages. The first stage starts at the moment of initial contact of the bodies and is characterized by the pure elastic deformations of the two bodies. As the impact progresses, the pressure between the two bodies increases until the peak pressure reaches the elastic yield limit $\sigma_Y$ of the softer of the two bodies. This marks the end of the first stage. As only elastic deformations occur during this phase, the Hertz equations may be applied. From these Rogers [10] had shown that the elastic yield limit is only attained for impact velocities "v" greater than limiting elastic velocities $\psi$, given by

$$\psi = \left(\frac{2\pi}{3K}\right)^2 \left(\frac{2}{5\rho}\right)^{0.5} \sigma_Y{}^{0.5} \qquad (1)$$

where $\rho$ is the density of impacting particle

$$K = \frac{4}{3\pi(k_1 + k_2)} \qquad (2)$$

with $k_i = ( 1 - \nu_i) / \pi E_i$ where $\nu_i$ and $E_i$ are the Poisson's ratio and the elastic modulus of the two types of particles(for i = 1, 2).

The energy stored in elastic deformations at the end of the first stage is $\frac{m\psi^2}{2}$. From Hertz equations, Rogers[10] showed that the centers of the two bodies have approached during first stage by a distance $h_e$ , given by

$$h_e = \left(\frac{2\pi y}{3k}\right)^2 R \qquad (3)$$

where $R$ is the radius of the smaller particles; see Bitter[30] .

The second stage of impact, which continues until the impacting bodies have zero relative velocity, is characterized by a growth of a region of plastic deformation in the softer of the two bodies. It is assumed that elastic limit remains constant through out the impact, *i.e.*, work-hardening effects are assumed to be negligible. The area of plastic deformation is surrounded by an annulus of elastic deformation (as shown in figure 3.1). This is equal, at any time during the second stage of impact, to the area at the end of the first stage of impact. Assuming the average pressure over the annulus is the same as that between the bodies at the end of the first stage of impact, it can be shown that the energy stored as elastic deformations in the annular region, $Q_e$, is $m\psi^2/2$ . The energy stored as elastic deformation in the area of plastic deformation at the end of second stage, $Q_{pe}$, is given by

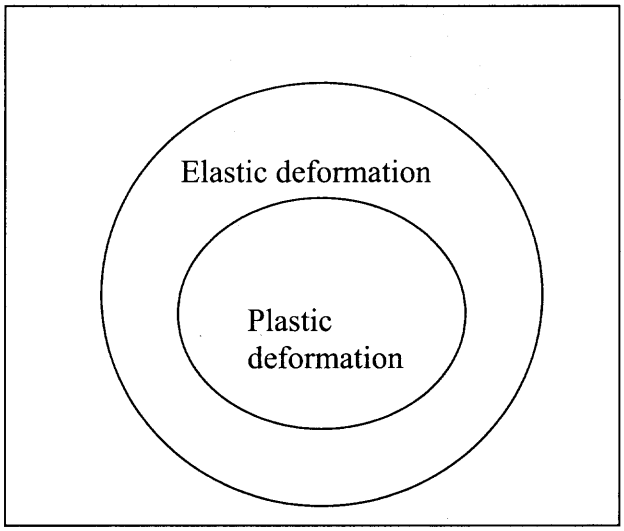


**Figure 3.1** The plastic and elastic areas within the area of contact.

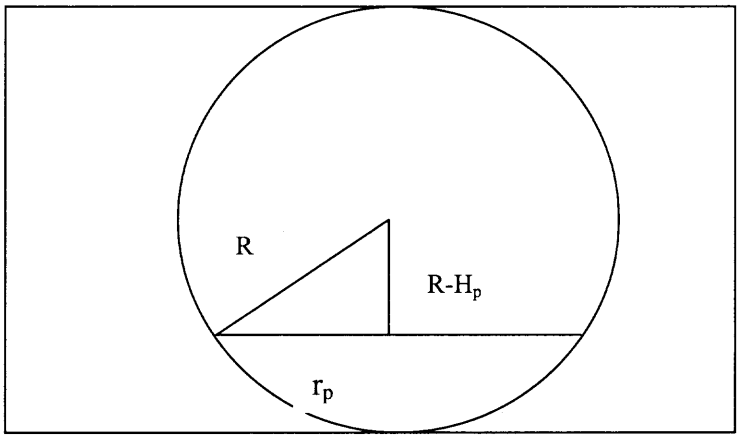


**Figure 3.2** The radius of deformation $r_p$ and the depth of deformation $H_p$.

$$Q_{pe} = \frac{h_e \pi r_p^2 y}{2} \approx h_e \pi R H_p y \qquad (4)$$

where $r_p$ is the projected radius of the area of plastic deformation, and for small plastic deformation, $r_p^2 = 2RH_p$ , where $H_p$ is the depth of the permanent deformation resulting

from the impact. The energy expended in producing this deformation, $Q_p$, is given by

$$Q_p = \int_0^{H_p} \pi r^2 y dH \tag{5}$$

where $r$ is the instantaneous projected radius of the area of plastic deformation, and $H_p$ is the depth of equivalent permanent deformation. From equations (1) through (5) $Q_{pe}$ can be derived to be

$$Q_{pe} = \frac{15}{4}\left(Q_e Q_p\right)^{1/2} \tag{6}$$

From the conservation of energy criterion it is known that

$$mv^2/2 = Q_e + Q_{pe} + Q_p$$

and hence

$$Q_p = \left( \frac{\left(2mv^2 - m\psi^2/8\right)^{1/2} - \left(15m\psi^2/8\right)^{1/2}}{2} \right)^2$$

and

$$Q_{pe} = \left(\frac{15m\psi^2}{8}\right)^2 \left( \frac{\left(2mv^2 - m\psi^2/8\right)^{1/2} - \left(15m\psi^2/8\right)^{1/2}}{2} \right)$$

Using equation (4) $r_p$ can be expressed as

$$r_p^2 = \frac{2Q_{pe}}{h_e \pi y}$$

The depth of plastic deformation can be evaluated as $H_p = \frac{r_p^{\,2}}{2R}$

The total adhesive energy $U_T$ is the sum of $U_M$ and $U_S$ where

$$U_M = P_0\left(\frac{P_1^{2/3} + 2P_0P_1^{-1/3}}{3K^{2/3}R_C^{1/3}}\right) \tag{7}$$

and

$$U_S = \Delta\gamma\pi\left(\frac{R_C P_1}{K}\right)^{2/3} \tag{8}$$

where $P_0$ is the external force applied to the contacting bodies, and

$$P_1 = P_0 + 3\Delta\gamma\pi R_C\left[\left(P_0 + 3\Delta\gamma\pi R_C\right)^2 - P_0^{\,2}\right]^{1/2} \tag{9}$$

$\Delta\gamma$ is the surface adhesive energy per unit area of contact, and the contact geometry parameter $R_C$ is defined by

$$\frac{1}{R_C} = \frac{1}{R_1} + \frac{1}{R_2}$$

$$\therefore R_C = \frac{R_1R_2}{R_1 + R_2}$$

## 3.2 A Sample Calculation

Herein, a typical calculation for evaluating the real energy involved in the adhesion phenomenon between spherical host and guest particle is shown. The guest and host particles are taken to be of PMMA (Polymethyl methacrylate) and alumina respectively. The steps of the calculation are the same used by Rogers and Reed [10]. Table 3.1 contains the physical, mechanical and surface properties of PMMA and Alumina [29,30,31].

**Table 3.1** The properties of PMMA and Alumina

| | PMMA | Alumina |
|---|---|---|
| Density ($kg/m^3$) | 1190 | 3970 |
| Modulus of Elasticity | 3300 MPa | 345 GPa |
| Poisson's Ratio | 0.5 | 0.26 |
| Yield Stress ( MPa) | 5-15 | 70 |
| Hardness (Knoop) | 21 | 2100 |
| Dispersive surface energy | 35.9 $mJ/m^2$ | 100 $mJ/m^2$ |
| Polar surface energy | 4.3 $mJ/m^2$ | 540 $mJ/m^2$ |

The radii of the alumina and PMMA particles are taken as 100 nm and 100 micron, respectively, in accordance with size ranges of MAIC process. As the size differences is quite high, the equations of Rogers *et.al.*[20] for a sphere impacting a plane surface is utilized in the following calculations.

In order to calculate the minimum velocity of impaction for plastic deformation the following calculations are done.

$$k_1 = k_{\text{alumina}} = \frac{(1-0.26)}{\pi \times 345 \times 10^9} = 6.827 \times 10^{-13}\ \text{m}^2/\text{N}$$

$$k_2 = k_{\text{PMMA}} = \frac{(1-0.5)}{\pi \times 3300 \times 10^6} = 4.822 \times 10^{-11}\ \text{m}^2/\text{N}$$

and from equation(2)

$K = 8.6771 \times 10^9\ \text{N/m}^2$

Therefore using equation (1) we get

$$\psi = \left(\frac{2\pi}{\pi \times 8.6771 \times 10^9}\right)^2 \left(\frac{2}{5 \times 3970}\right)^{0.5} \left(15 \times 10^6\right)^{2.5} = 1.14 \times 10^{-3}\ \text{m/s}$$

The approach of two spheres during first stage of collision is given by

$$\therefore h_e = \left(\frac{2\pi \times 15 \times 10^6}{3 \times 8.6771 \times 10^9}\right)^2 \times 100 \times 10^{-9} = 2.96 \times 10^{-12}\ \text{m}$$

Let us consider the impacting velocity be $v = 0.001$ m/s, the mass $m$ is of alumina

$$m = \frac{4\pi\left(100 \times 10^{-9}\right)^3 \times 3970}{3} = 1.66 \times 10^{-17}\ \text{kg}$$

Then

$$Q_p = 1.66 \times 10^{-17} \left( \frac{\left(2 \times 0.001^2 - \left(5.09 \times 10^{-4}\right)^2 / 8\right)^{1/2} - \left(15\left(5.09 \times 10^{-4}\right)^2 / 8\right)^{1/2}}{2} \right)^2$$

$\therefore Q_p = 1.79 \times 10^{-25}$ Joule.

and

$$Q_{pe} = \left( \frac{15 \times 1.66 \times 10^{-17} \left(5.09 \times 10^{-4}\right)^2}{8} \right)^2 \left(1.79 \times 10^{-25}\right)^{1/2} = 2.69 \times 10^{-24} \text{ Joule}$$

Using equation (4) we get

$$r_p^2 = \frac{2Q_{pe}}{h_e \pi y} = \frac{2 \times 2.69 \times 10^{-24}}{2.96 \times 10^{-12} \times \pi \times 15 \times 10^6} \text{ m}^2$$

$$\therefore r_p = 1.97 \times 10^{-10} \text{ m}$$

We can also get the depth of plastic deformation as

$$H_p = \frac{r_p^2}{2R} = \frac{3.8809 \times 10^{-20}}{2 \times 100 \times 10^{-9}} = 1.95 \times 10^{-13} \text{ m}$$

The contact geometry parameter $R_C$ can be estimated as

$$\frac{1}{R_C} = \frac{1}{R_1} + \frac{1}{R_2}$$

$$\therefore R_C = \frac{R_1 R_2}{R_1 + R_2} = 9.99 \times 10^{-8} \text{ m}$$

The external load is considered as the weight of the particle so that

$P_0 = mg = 1.66 \times 10^{-17} \times 9.81$ N

$\therefore P_0 = 1.631 \times 10^{-16}$ N

Using the value of $P_0$ in equation (9) we can calculate $P_1$ with the value of surface energy. According to Rogers[20]

$$\Delta\gamma = 2\,(\gamma_1^{d}\,\gamma_2^{d})^{1/2} + 2\,(\gamma_1^{m}\,\gamma_2^{m})^{1/2}$$

$$= 2\,(100 \times 35.9)^{1/2} + 2\,(540 \times 4.3)^{1/2}$$

$$= 216.207\ \text{mJ/m}^2 = 0.216\ \text{J/ m}^2$$

$$\therefore P_1 = 1.631\times10^{-16} + 3\times 0.216 \times \pi \times 9.99\times10^{-8} + [(1.631 \times 10^{-16} + 3 \times 0.216 \times \pi \times 9.99\times10^{-8})^2 - (1.631\times10^{-16})^2\,]^{0.5}$$

$$= 1.65 \times 10^{-8}\ \text{N}$$

Using equation (7) and (8) we get the mechanical and surface energy as

$$U_M = 1.631\times10^{-16}\left(\frac{\left(1.65\times10^{-8}\right)^{2/3} + 2\times\left(1.631\times10^{-16}\right)\left(1.65\times10^{-8}\right)^{-1/3}}{3\times\left(8.6771\times10^{9}\right)^{2/3}\left(9.99\times10^{-8}\right)^{1/3}}\right)$$

$$= 6.8625 \times 10^{-20}\ \text{J}.$$

And,

$$U_S = 0.216\pi\left(\frac{9.99\times10^{-8} \times 1.65\times10^{-8}}{8.6771}\times10^{-9}\right)^{2/3} = 3.486 \times 10^{-18}\ \text{J}.$$

In the Figure 3.3 the arc AB shows the original surface of PMMA and AB shows diameter of the area undergone plastic deformation. So in this case we know AC = $1.97 \times 10^{-10}$ m and we need to find AB. AO and BO are the radii = 100 micron.

We know

$$\frac{\mathbf{AC}}{\mathbf{AO}} = \frac{1.97 \times 10^{-10}}{100 \times 10^{-6}} = \sin\alpha$$

$$\therefore \alpha = 1.97 \times 10^{-6} \text{ rad.}$$

$$\therefore 2\alpha = 3.94 \times 10^{-6} \text{ rad.}$$

So for 40% of initial coating on the PMMA surface the angle the said surface makes with the center of the sphere will be $0.4 \times 2\pi$ rad. Then the energy requirement is $0.4 \times 2\pi / 3.94 \times 10^{-6}$ times of that calculated earlier.

$$\therefore U_{M,40\%} = \frac{0.4 \times 2\pi \times 6.8625 \times 10^{-26}}{3.94 \times 10^{-6}} = 4.377 \times 10^{-20} \text{ J}$$

$$\therefore U_{S,40\%} = \frac{0.4 \times 2\pi \times 3.486 \times 10^{-18}}{3.94 \times 10^{-6}} = 2.223 \times 10^{-12} \text{ J}$$

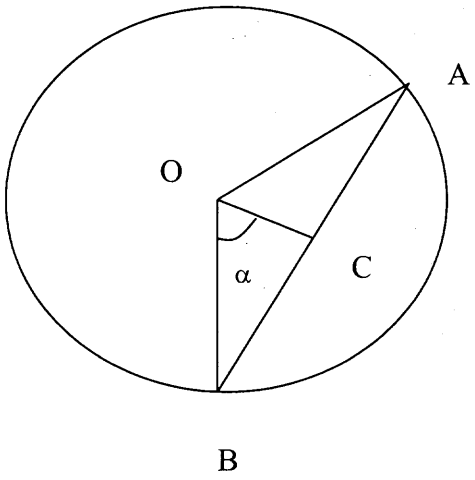


**Figure 3.3** The schematic shows the host particle (circle), and an arc AB as the original surface of PMMA, with AB the diameter of the area undergoing plastic deformation.

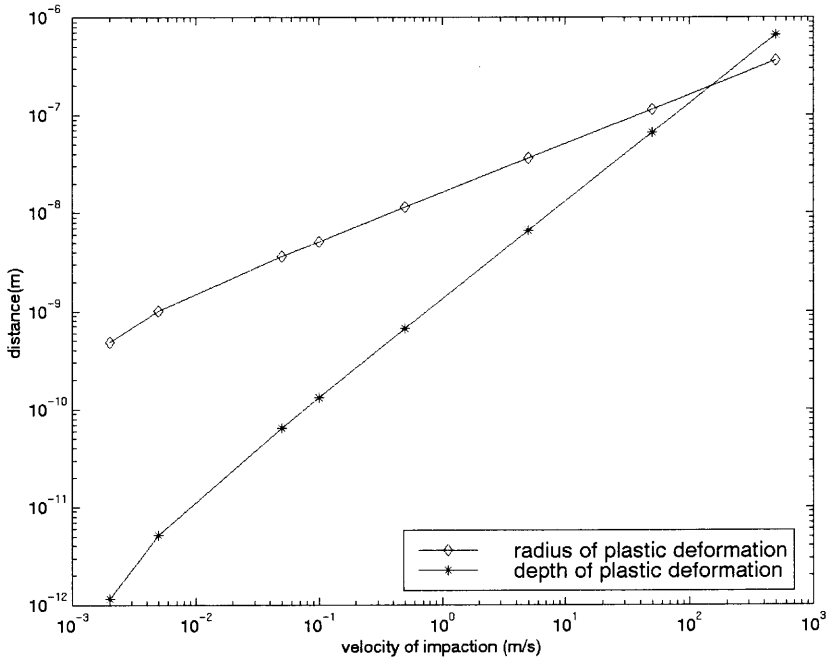


**Figure 3.4** The variation of depth and radius of deformation for the change of impaction velocity of the guest particle on the host particle.

### 3.3 The Variation of Deformation and Energy as a Function of Impaction Velocity and Guest Particle Size

The impaction velocity is varied while keeping the sizes of both host and guest particles constant . The radius of plastic deformation and the depth of permanent deformation are plotted in figure 3.4. All of the following plots are made in logarithmic scale due to the large differences in the orders of magnitude of the evaluated quantities. It is seen with the increase of impaction velocity the penetration depth and radius increase. The velocity required for half of the guest particle to be embedded in the host surface is close to 100 m/s. It is also evident from the slope of the curves that depth

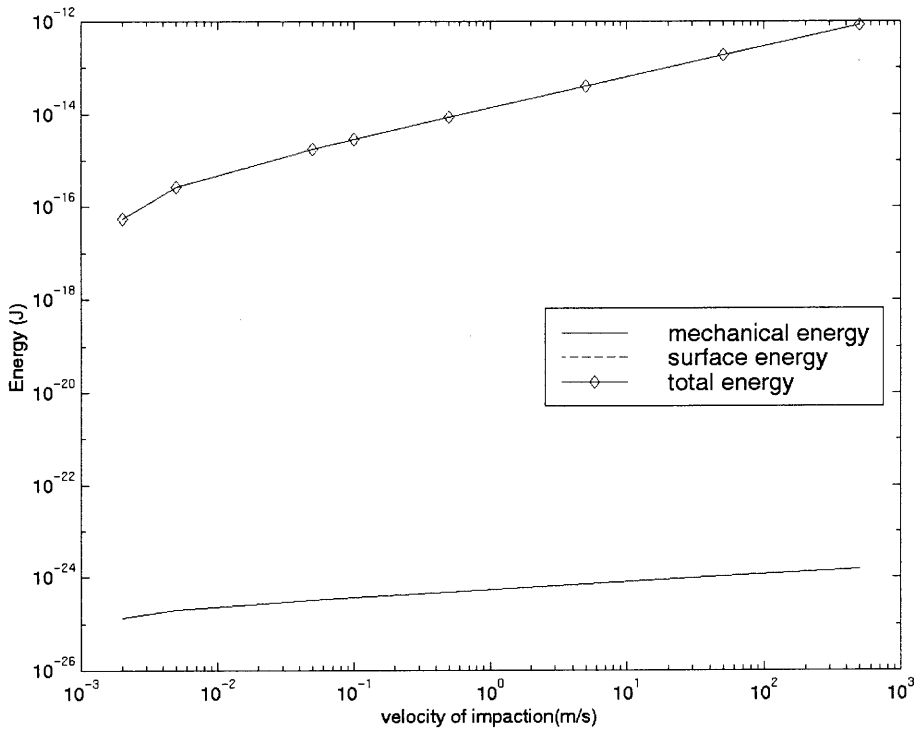


**Figure 3.5** The variation of mechanical and surface energies for the change of impaction velocity of the guest particle on the host particle.

of permanent deformation increases more rapidly then the radius of plastic deformation if the velocity of impaction increases. At the impaction velocity of 200 m/s the curves intersect and the depth becomes bigger than the radius of deformation. Figure 3.5 shows the plot of surface energy, mechanical energy and their sum (total adhesive energy) against the impaction velocity. All the energies increase with the increase of impaction velocity of the guest particle. The total adhesive energy is the sum of the surface and mechanical energies. In time, the surface energy becomes more dominant over mechanical or inertial energy and almost solely contributes to the total adhesive energy.

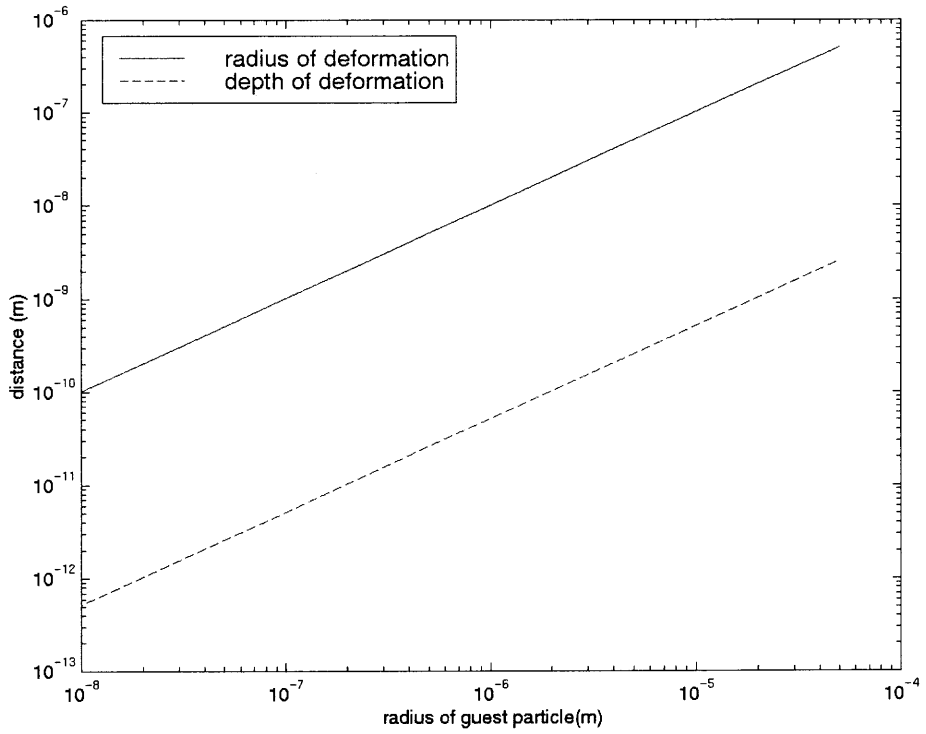


**Figure 3.6** The change of radius and depth of deformation with the variation of the radius of the guest particle. The impaction velocity is kept constant to 0.001 m/s.

Then the effect of the size of host particle is estimated keeping the guest particle radius constant as 200 micron and the impaction velocity fixed to 0.005 m/s. The size of guest particle(alumina) is a varied to evaluate corresponding depth and radius of deformation and pertinent energies (Figure 3.6 and 3.7). In Figure 3.6 it is seen that the radius and depth of deformation increases linearly. The slopes of both the curves are same and radius of deformation is found to be always more than the depth. The surface energy is found to be lot more than the mechanical energy and the total energy is mostly from surface energy (Figure 3.7). All the energies increase with radius of guest particle.

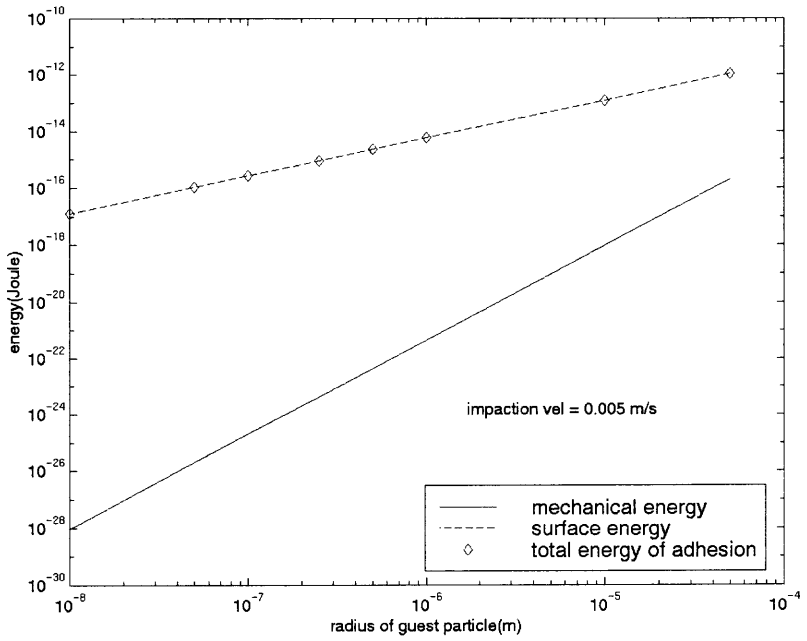


**Figure 3.7** The variation of mechanical, surface and total energy with the change of radius of host particle. The impaction velocity is kept constant to the value of 0.001 m/s.

Then the effect of size is calculated with a higher velocity of 10 m/s. In Figure 3.8 it is seen the slope of the radius and depth of deformation curves are same but the difference

in their values is less than that in Figure 3.6. In Figure 3.9 the surface energy is more

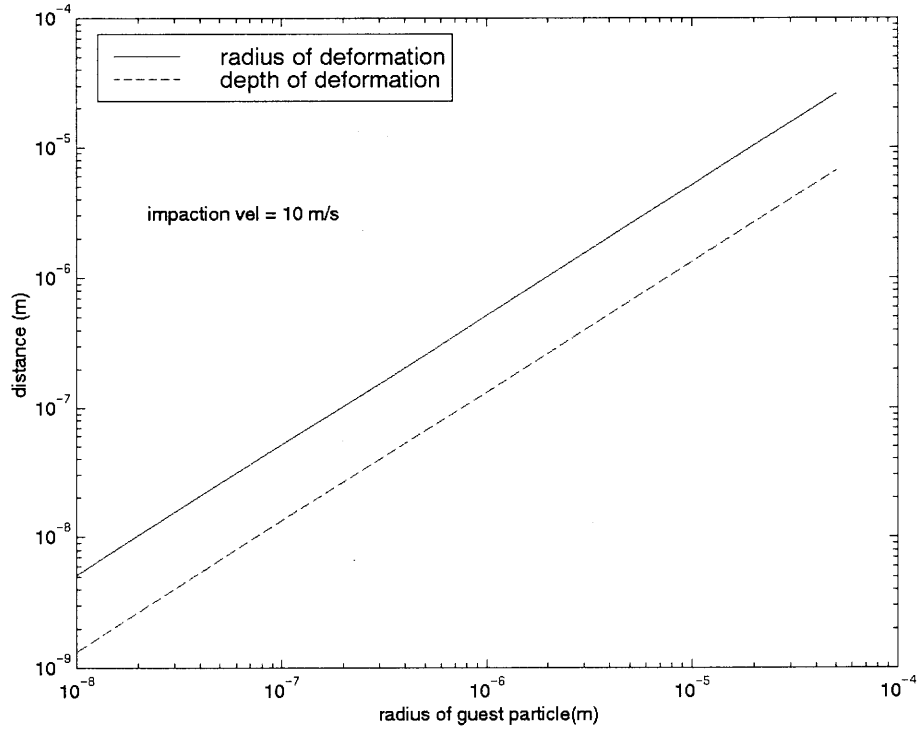


**Figure 3.8** The change of radius and depth of deformation with the variation of the radius of the guest particle. The impaction velocity is kept constant to 10 m/s.

more than the mechanical energy. The total energy is equal to surface energy for all radius of the guest particle.

## 3.4 Conclusions

In the case of head on particle collision, the appropriate velocity necessary to create a plastic deformation is estimated from a known model. The radius of plastic deformation is generally more than the depth of plastic deformation. The total energy of adhesion is the sum of surface and mechanical energy. This total energy is almost equal to the surface

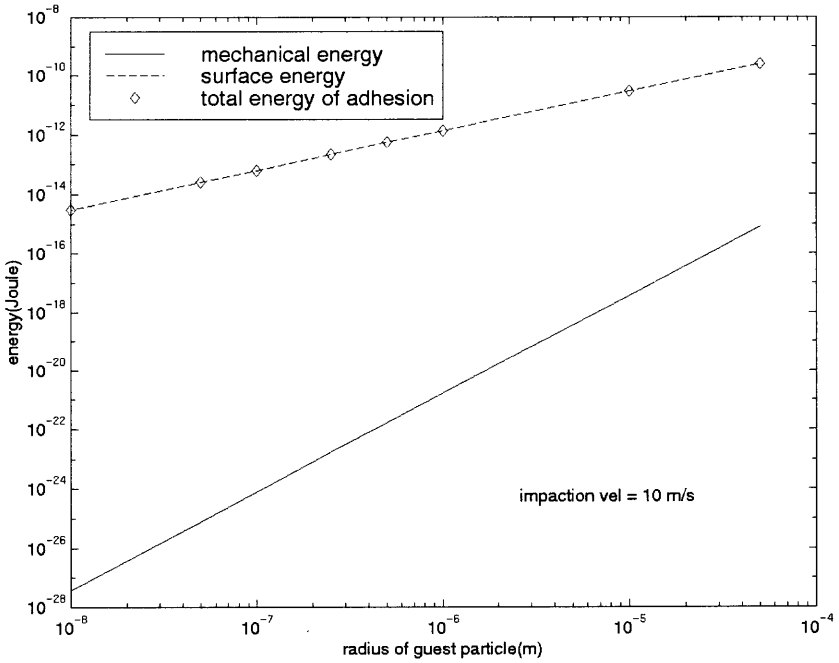


**Figure 3.9** The change of radius and depth of deformation with the variation of the radius of the guest particle. The impaction velocity is kept constant to be 10 m/s.

energy of adhesion in different ranges of the important parameters like particle size and impacting velocity.

In MAIC, though it is very unlikely for a guest to collide with a single host particle, the effective velocity necessary to create plastic deformation can be obtained from the discussed theory. In device or host scale modeling the MAIC system has to achieve such velocities of impaction between the host and guest particles. The applicability of the theory is further explained in chapter 4 where it aids to predicting the plastic deformation in the guest and the host particles. The deformation information also leads to the estimation of adhesion force between the particles.

# CHAPTER 4

# DEVICE AND HOST SCALE MODELING

## 4.1 Device and Host Scale Phenomena

In this dry particle coating process tiny guest particles are coated onto relatively larger host particles in order to create value added composite particulate. In an alternating magnetic field a time-dependent torque acts on the magnetic particles (non-spherical). The magnitude and direction of the torque depends on the relative orientation of the magnetic particles and the instantaneous magnetic field. The magnets experience a force and a torque while interacting within themselves. The torque causes magnetic particles to rotate and collide randomly with the core and secondary particles, as well as with each other. Therefore, both their orientation relative to the applied magnetic field and the torque acting on the magnetic particles can be assumed random. The random torque and the resulting random collisions among the magnetic and other particles cause the particulate mixture to fluidize. So the purpose of the device scale modeling is to simulate similar fluidized conditions and to check the effect of system parameters like external magnetic field, size and mass of the magnets etc. on the nature of fluidization of particles. An existing discrete element code[32] is used to the model the particle dynamics and hence the fluidization of magnetic particles.

The random collisions which take place in this process lead to the mixing and plastic deformation of particles. In particle scale modeling the collision of host particles in the system is studied. The same model of device scale which only has magnets is used

with other host or nonmagnetic particles to perform particle scale modeling. The normal velocity of impaction , the normal and tangential forces during the collision are estimated and compared with the result presented in chapter three for host and guest collision.

## 4.2 Device Scale Modeling

Molecular dynamics method is used in the field of theoretical chemistry and fluid mechanics to achieve a deterministic solution of the N-body problem. Discrete element method is very popular to model particle dynamics. The major difference between molecules of fluid and bulk particulate is their interaction models. Energy dissipation is essential to granular systems, while energy conservation is the characteristics of fluid systems. The model of the interaction of granular particles have been developed using two different approaches, namely hard and soft sphere models. Hard sphere model considers the particles to be hard spheres that undergo instantaneous, binary collisions. Post-collision velocity is calculated as function of approach velocity and particle properties like the coefficient of friction, normal and tangential restitution coefficient. The Soft sphere model or "Latching spring model" developed by Walton and Braun[33,34], on the other hand, allows colliding particles to overlap, and the interaction force is a function of this relative overlap among other factors. Collisions last for multiple time steps and Newton's equation is solved to estimate the velocity and position of the particle at every time step.

### 4.2.1 General Algorithm and Structure of the DEM Code

In the DEM code all the entities like particles and the boundaries are each separately considered as a discrete element. The initial coordinates for particles are generated via a random number generator. A radii expansion technique is used to determine an initial configuration for the system. Then all the initial and boundary conditions are superimposed to initialize the simulation. The time increment, usually called time step, is significantly smaller than the typical time taken for a collision to ensure a sufficient degree of accuracy. The mechanical interaction force which acts only while particles are colliding within themselves or with the wall. In each time step the following steps are performed:

(a) estimating the neighbor list of each of the particle.

(b) the force and torque is calculated for those pair of particle which are in contact.

(c) the force and torque acting on each particle is the sum of same calculated trying pairwise interaction between particles.

(d) a second order finite difference algorithm developed by Verlet is employed to solve equations of motion of the system of interacting particle to estimate the positions , orientations, linear and rotational velocities

The flow diagram of the algorithm is shown below:

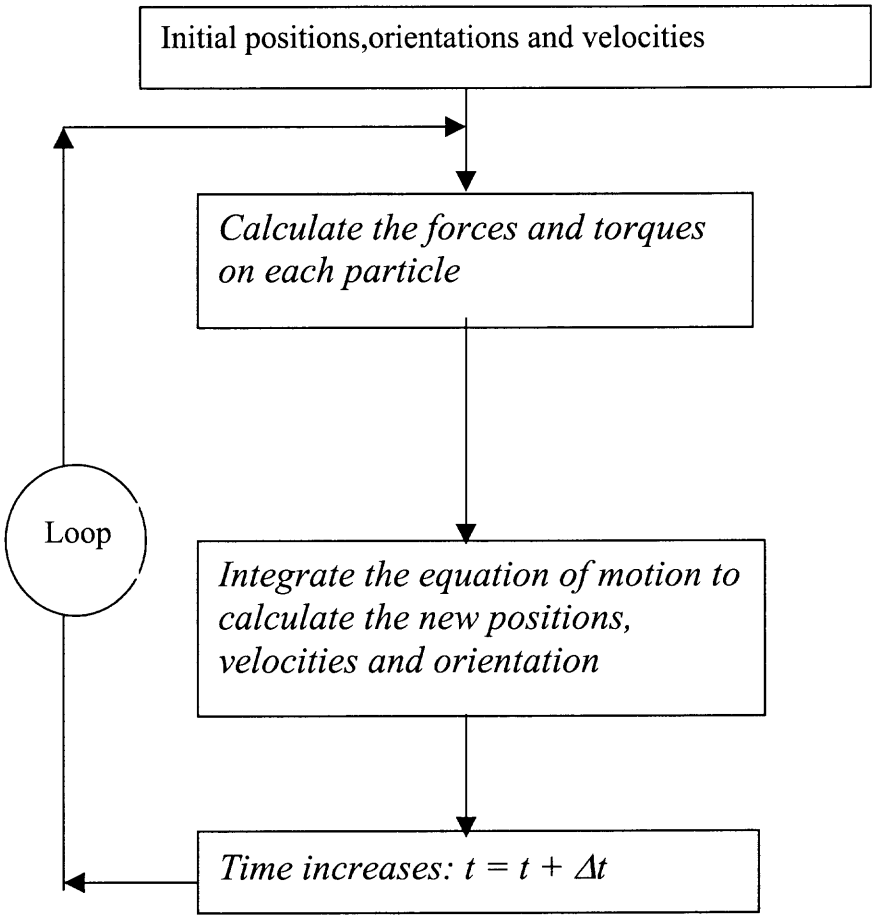


**Figure 4.1** The flow diagram of the discrete element modeling.

### 4.2.2 The DEM Code for Device Scale Modeling

The simulation code used in current studies has been modified from the mentioned uniform shearing flow code developed by Walton *et.al.*() to a hopper flow code by Dr Maher Moaker and Dr Muzzio. The source code **rgflow.c** for flow of particle in hopper comprises different functions which exit in filenames of :

(1) **datain.c** (2) **forces.c** (3) **integ.c** (4) **update.c** (5) **zones.c** (6) **findrad.c** (7) **init.c** (8) **xvprint.c**

**rgflow.c**

This is the main program which calls 8 other functions to run the discrete element algorithm. The variables like position, transnational and rotational velocity, force, torque displacement and quaternion of all the particles in the system are all defined here. After the initialization is done by **init.c** the dynamics allocation of memory for each of the variable mentioned above is achieved. The algorithm of discrete element method is followed thereafter iteratively. In the algorithm in each time step the force between the particles and that of the particle and wall in calculated. Newton's equation of motion is solved to find out the positions, velocities and quaternion of each of the particle. At definite time interval the position and orientation of the particles are printed out.

**datain.c**

The main program calls this routine to read the input to the program such as the number of the types of the particles, their radii and masses. The hopper dimensions and the collision parameters such as spring constant of particle-particle and particle-wall collision, co-efficient of restitution, co-efficient of friction are also read from the input

file. It also reads the maximum time of simulation, timestep of printing ASCI and binary data, the value of gravity, the number of timesteps during each collision, search distance to determine the appropriate number of neighbors and some other flag values which determine the effectivity of different sorts of forces. Finally it calculates the simulation volume, the total particle volume and hence the packing ratio of particles in the system.

**init.c**

In this function the initialization of particle system is done. The particles are arranged randomly and a translational velocity is given to all of them. The initial rotational velocity is set to be zero. The quaternion of all the particles are set to zero.

**findrad.c**

The main program needs this function to get rid of the initial overlap of the particles during the random positioning of the particle in the earlier routine. This function follows the DEM algorithm where in each time step it calculates the force acting between the particles and integrate thereafter the Newton's equation of motion to find out the new position of the particles.

**zones.c**

Initially in this function the simulation volume is splitted into number of cubic volumes(cells) according to the users input. In each timestep of the DEM run this function is called as it specifies the zone in which each particle is located. Moreover, it also finds out the list of neighboring zones associated with each particle. For each particle It finds out 26 neighboring zones in three dimensions.

**update.c**

As mentioned above that the list of zones are composed in each run for each of the particles, the particles in each of the zones are also traced out. If the distance between the

particle in the neighboring zone and the main particle is less than a specified search distance then the former particle gets added into the latter's neighbor list.

**xvprint.c**

This function is called after findrad and at regular intervals to print out the positions, velocities and orientation of all of the particles. It is also capable to dump the coordinates, velocities and the link list of all the particles into an unformatted sequential file in binary format. This binary file can be read by this function itself to start a new run of particle dynamics.

**forces.c**

In DEM algorithm this function is used in every timestep. Initially the forces and torque for each particle are set to be zero. Then the inter particle forces and particle-wall forces are calculated using Walton-Braun's latching model. The model gives the normal and tangential force and the axial torque for each of the particle colliding within themselves or with the wall. The force or torque in three Cartesian directions are evaluated.

**integ.c**

Newton's equation of motion for force and torque is written in second order finite difference scheme. Verlet's Leap-Frog method is employed to find out position and the Euler angles of the particle after the force and torque are calculated. Moreover the translational and rotational velocities are also evaluated in this function. The quaternion are calculated at the end from the Euler angles.

The computer simulation is performed on a three dimensional control volume and the recent modifications incorporated for this dissertation include:

(a) Consideration the torque equation for the external torque.

(b) Incorporate the force and torque for dipole-dipole interaction.

(c) Incorporate short and long ranged van der walls forces between particles and particle the wall.

(d) Estimating the transformation matrix of each particle with their positions and the quaternion for developing the animation of the particle dynamics.

The first three modifications are done in a modular manner in the existing routine of **forces.c** and the last change is done in **integ.c** and **init.c**.

### 4.2.3 The Force Calculation

The forces and torque acting on each particle is calculated in two different ways. Force in all the cases are generally calculated by adding up the forces(or torque) calculated in pairwise interaction of particles. In the other case the force ( or toque) is calculated separately for every particle. All of the different types of forces that might act on each particle in the system are shown below:

$$\sum \mathbf{F}_i = \mathbf{F}_{\text{external magnetic field}} + m_i\mathbf{g} + \mathbf{F}_{\text{Van der Waal}} + \mathbf{F}_{\text{interparticle magnetic force}} + \mathbf{F}_{\text{interparticle mechanical force}} \quad (1)$$

$$\sum \mathbf{T}_i = \mathbf{T}_{\text{external magnetic field}} + \mathbf{T}_{\text{interparticle magnetic torque}} + \mathbf{T}_{\text{torque in mechanical interaction}} \quad (2)$$

The force for external magnetic field and the gravitational force can be calculated independently whereas the other forces arise for pairwise interaction of particles.

So any particle in the system will be experiencing forces for external magnetic field, gravity, Van der Waal force due to particle-particle or particle-wall interaction, inter particle magnetic force(if particles are magnetic) and the interparticle mechanical force which arises during particle-particle or particle-wall collision. On the other hand the

torque acting on any particle comprises of the torque due to external magnetic field(if the particle is magnetic), interparticle magnetic torque( if the particle is magnetic) and interparticle mechanical torque which appears during particle-particle or particle-wall collision.

**4.2.3.1 Van der Waals Force:** Dispersion force is the one which act between all the atoms or molecules of substances and contributes maximum to the van der Waals force. Van der Waals force is play a major role in the important phenomena such as adhesion, physical adsorption and surface tension or energy. Their main features could be summarized as follows:

(a) They are long range forces and could be effective in the varied range of distance of 10nm to 0.2nm.

(b) They not only bring the bodies closer but also mutually orient them.

(c) The forces may be attractive or repulsive.

In our case the van der Waals force is calculated between the particles and between particle and the wall surface. The van der Waals force between two spherical particles of radius R separated by a small distance D is given by: $F = AR / 12 D^2$ , where A is the conventional Hamaker constant. Typical value for Hamakers constants of condensed phases, whether solid or liquid, is $10^{-19}$ Joule for interaction across the vacuum[23]. For two unequal spherical particles of radius $R_1$ and $R_2$ separated by a small distance D is given by

$$F = \frac{A}{6D^2} \quad \frac{R_1 R_2}{R_1 + R_2} \tag{3}$$

For a spherical particle of radius R the interaction force with a wall surface is

$$F = AR/6D^2 \quad (4)$$

The van der Waals force is effective when the particles are in contact within themselves or with the wall. The distance between particles or particle and wall (considered A above) Is considered to be 4 x $10^{-10}$ m when they are in contact and the real distance is used when there is no contact. However, Israelachvili[23] recommends the use of D = 1.65 x $10^{-10}$ meter.

**4.2.3.2 Mechanical Interaction Force and Torque**: Normal force

The normal force during contact, $F_N$ is as follows in two different phases of collsion:

$$F_N = \begin{cases} K_1\alpha, & \text{for loading} \\ K_2(\alpha - \alpha_0), & \text{for unloading} \end{cases} \quad (5)$$

Where $\alpha$ is the overlap between the contacting spheres . The unloading spring constant $K_2$ is greater than $K_1$ , the loading spring constant. $\alpha_0$ is the relative overlap where the unloading force is set to zero. This model of normal force produces binary collisions with constant coefficient of restitution given by $e = \sqrt{K_1/K_2}$ , where e is independent of the relative velocity of impact.

**Tangential force**

Walton and Braun's initial one dimensional model approximate Mindlin's (1949) elastic frictional sphere contact force model. This tangential friction force model of Walton() is a two dimensional extension of that 1D model. In that earlier model the effective tangential stiffness of a contact decreases with tangential displacement until it is zero

when full sliding takes place. In the later two dimensional surface force model the displacement perpendicular to the existing friction force and the tangential displacement parallel to the current friction force are considered separately . They are added vectorially and the combination is checked with the total friction force limit of $\mu F_N$. So the effective tangential stiffness in the direction parallel to the existing friction force is given by:

$$\mathbf{K_T} = \begin{cases} \mathbf{K_0}\left(1 - \dfrac{\mathbf{T} - \mathbf{T}^*}{\mu \mathbf{F_N} - \mathbf{T}^*}\right)^{\gamma} & \textbf{for} \quad \mathbf{T} \quad \textbf{increasing} \\ \mathbf{K_0}\left(1 - \dfrac{\mathbf{T}^* - \mathbf{T}}{\mu \mathbf{F_N} + \mathbf{T}^*}\right)^{\gamma} & \textbf{for} \quad \mathbf{T} \quad \textbf{decreasing} \end{cases} \tag{6}$$

Where and $\mu$ is the coefficient of friction; $K_0$ is the initial tangential stiffness; T is the current tangential force magnitude; $T^*$ starts as zero and is subsequently set to the value of the total tangential force of T, whenever the magnitude changes from increasing to decreasing, or vice versa. $\gamma$ is a fixed parameter set to 1/3. The usage of this friction model involves some and vector and algebraic manipulation since the direction of the surface normal at contact changes continuously during a typical contact. The simulation model assumes that the displacements from one time step to the next are relatively small. When two spheres i and j are in contact we let $\hat{k}_{ij}$ be the current unit vector from the center of sphere i to sphere j, ( *i.e* $\hat{k}_{ij} = (r_j - r_i) / | r_j - r_i |$ , where $r_i$ is the radius vector for the location of sphere i,). The vector $\hat{k}_{ij}$ is also the unit normal at the contact point

between spheres j and i. The tangential force from the previous time step, $T_{old}$ , is projected onto the current tangent plane,

$$\begin{aligned} \mathbf{T_o} &= \hat{\mathbf{k}}_{\mathbf{ij}} \times \mathbf{T_{old}} \times \hat{\mathbf{k}}_{\mathbf{ij}} \\ &= \mathbf{T_{old}} - \hat{\mathbf{k}}_{\mathbf{ij}} \left( \hat{\mathbf{k}}_{\mathbf{ij}} \bullet \mathbf{T_{old}} \right) \end{aligned} \tag{7}$$

This normalization of the projected friction force to the old magnitude is done, so that $|T| = |T_{old}|$, to evaluate a new starting value for the friction force T before adding in the effects of displacements during the last time step.

A unit vector in the direction of this starting friction force $\hat{t} = T/|T|$, is used in several subsequent steps. The relative surface displacement during the last time step is projected onto the contact tangent plane .

$$\begin{aligned} \Delta \mathbf{s}^{\mathbf{n-1/2}} &= \left[ \hat{\mathbf{k}}_{\mathbf{ij}} \times \left( \mathbf{v}_{\mathbf{j}}^{\mathbf{n-1/2}} - \mathbf{v}_{\mathbf{i}}^{\mathbf{n-1/2}} \right) \times \hat{\mathbf{k}}_{\mathbf{ij}} + \mathbf{r_i} \left( \overset{\rightarrow}{\omega}^{\mathbf{n-1/2}} \times \hat{\mathbf{k}}_{\mathbf{ij}} \right) + \mathbf{r_j} \left( \overset{\rightarrow}{\omega}^{\mathbf{n-1/2}} \times \hat{\mathbf{k}}_{\mathbf{ij}} \right) \right] \Delta \mathbf{t} \\ &\approx \Delta \mathbf{r_{ij}} - \hat{\mathbf{k}}_{\mathbf{ij}} \left( \hat{\mathbf{k}}_{\mathbf{ij}} \bullet \Delta \mathbf{r_{ij}} \right) + \left[ \mathbf{r_i} \left( \overset{\rightarrow}{\omega}^{\mathbf{n-1/2}} \times \hat{\mathbf{k}}_{\mathbf{ij}} \right) + \mathbf{r_j} \left( \overset{\rightarrow}{\omega}^{\mathbf{n-1/2}} \times \hat{\mathbf{k}}_{\mathbf{ij}} \right) \right] \Delta \mathbf{t}, \end{aligned} \tag{8}$$

Where $\Delta r_{ij} = r_{ij}^{n} - r_{ij}^{n-1}$ is the change in the relative position vector during the last time step. V is the velocity, and $\vec{\omega}$ the angular velocity, and r the sphere radius, with subscripts i and j indicating sphere I or J and the $\Delta t$ is the timestep. The displacement parallel to the "old" friction force is

$$\Delta s_{\parallel} = \left( \Delta s^{n-1/2} \bullet \hat{t} \right) \hat{t} \tag{9}$$

And the displacement perpendicular is

$$\Delta \mathbf{s}_{\perp} = \Delta \mathbf{s}^{\mathbf{n}-1/2} - \Delta \mathbf{s}_{\parallel} \tag{10}$$

The effect of the displacement parallel to the existing friction force is treated almost identically with the 1-dimentional WB model with the exception that the value of T is always positive(it is the magnitude of a vector in this 2-D model). If the value of the normal force, $F_N$ , changes from one time step to the next, then the value of $T^*$ in Eq.(5) is scaled in proportion to the change in normal force.

$$\mathbf{T}^{*'} = \mathbf{T}^{*} \left| \mathbf{F}_{\mathbf{N}}^{\mathbf{n}} / \mathbf{F}_{\mathbf{N}}^{\mathbf{n}-1} \right| \tag{11}$$

The effective incremental tangential stiffness, $K_T$, is determined from Eq.(5) with $T^*$ substituted for $T^*$. A new value for the component of the friction force parallel to the old friction force, $T_{\parallel}$, is calculated,

$$\mathbf{T}_{\parallel} = \mathbf{T} + \mathbf{K}_{\mathbf{T}} \Delta \mathbf{s}_{\parallel} \tag{12}$$

If both of the conditions hold,

$$\left( \Delta \mathbf{s}^{\mathbf{n}-1/2} \bullet \hat{\mathbf{t}} \right) \; < \; 0 \; \textbf{and} \; \; \mathbf{T} + \left( \Delta \mathbf{s}^{\mathbf{n}-1/2} \bullet \hat{\mathbf{t}} \right) \mathbf{K}_{\mathbf{T}} \; < \; 0 \tag{13}$$

Are simultaneously true then, in effect, the direction of $T_{\|}$ has reversed, and in the model the sign of the effective remembered turning point, $T^*$ is changed, for the next time step so as to produce a smoothly varying slope using Eq(5).

Displacement perpendicular to the existing friction force is assumed to have no pre-existing surface strain and is, thus, treated as "new" displacement from the origin with an effective stiffness equal to the value of $K_0$ in Eq. (5), so that the perpendicular part of the tangential force becomes,

$$\mathbf{T}_{\perp} = \mathbf{K}_0 \Delta \mathbf{s}_{\perp} \tag{14}$$

The new tangential force is tentatively set equal to the vector sum of $T_{\|}$ and $T_{\perp}$,

$$\mathbf{T}' = \mathbf{T}_{\|} + \mathbf{T}_{\perp} \tag{15}$$

This value is checked to ensure that it dose not exceed the friction limit, $\mu F_N$, and if it does, it is scaled back so its magnitude equals that limit. When the exponent, $\gamma$, is set to zero, the model becomes linear.

**4.2.3.3 The Dipole-Dipole Interaction Force and Torque:** The magnetic particles in the system are considered to be dipole for simplicity. The dipoles rotate under external magnetic field and for dipole-dipole interaction. So each dipole is assumed to be with a local co-ordinate system. Each dipole $m_i$ is defined by $m_i = M\{dp_ix, dp_iy, dp_iz\}$; where M is the dipole moment of the magnetic particle and the $dp_ix$, $dp_iy$ and $dp_iz$ are the three unit vectors of the local co-ordinate system of the particle.

Then the torque, $\mathbf{T}_{ext}$, existing on a magnetic particle due to the external field is given by,

$$\mathbf{T}_{ext} = \mathbf{m} \times \mathbf{B}_{external} \tag{16}$$

where $\mathbf{m}$ is the magnetic dipole moment of the particle, and $\mathbf{B}_{external}$ is the magnetic flux density of the external field. While the exact expressions for the magnetic flux density in a finite sized field coil are complex, our first assumption is to consider the coil as an infinite length solenoid. Thus the $\mathbf{B}_{external}$ is given by

$$\mathbf{B}_{external} = \mu_o N I \hat{\mathbf{k}} = \mu_o N I_o \text{Sin}(\omega t) \hat{\mathbf{k}} \tag{17}$$

where $\mu_o$ is the permeability, $N$ is the number of turns per meter in the coil, $I$ is the current in the coil, given by $I = I_o \sin(\omega t)$, and $\hat{\mathbf{k}}$ is the unit vector in the direction of the solenoid axis. Since the current oscillates at the frequency of $\omega$, the external field also oscillates at the same frequency. Thus the torque (equation (16)) acting on the particle is time varying. If the torque were constant, a magnetic particle would tend to align itself with the flux and in the presence of any damping effects, it would eventually come to rest. However, since the flux is time-variant, its direction continuously switches, and the magnetic particle may not come to rest under small damping. As a result, the applied torque would cause the particle to spin. The torque for external field on any magnetic particle can be calculated by the following equation:

$$\begin{aligned} T_{ext} &= m_i \times B_{external} \\ &= M \{dp_ix, dp_iy, dp_iz\} \times \mu_o N I \{0,0,1\} \\ &= M\mu_o N I \{ dp_iy, - dp_ix, 0\} \end{aligned} \tag{17}$$

Apart from the effect of external field, particles themselves generate a magnetic field around them, and that field varies strongly with spatial position. This dipole-dipole induced flux density, $\mathbf{B}_{dipole}$ is given by [35]

$$\mathbf{B}_{dipole}=\frac{\mu_0}{4r^5\pi}\left[3(\mathbf{m}\cdot\mathbf{r})\mathbf{r}-r^2\mathbf{m}\right] \tag{18}$$

where the vector **r** is the position where the field is computed with respect to the dipole coordinate system and **m** is the magnetic dipole moment. Due to this field, in addition to generating a net torque, there is also a net magnetic force on the particle and the particle is subjected to translation in addition to rotation. The net force, **F,** acting on a magnetic particle due to the combined magnetic flux, **B** is [36]

$$\mathbf{F} = \nabla (\mathbf{m} \cdot \mathbf{B}) \tag{19}$$

and the net torque, **T** on a particle is

$$\mathbf{T} = \mathbf{m} \times \mathbf{B} \tag{20}$$

where **B** is the total magnetic flux density, which includes the external field. In case of a solenoid and a single magnetic particle, the magnetic flux density is uniform in space, hence there is no net magnetic force on the particle and there is only a net torque given by equation (16). Thus a simple equation for the rotational motion of a particle is

$$J\,\ddot{\theta} = \mathbf{m} \times \mathbf{B} \tag{21}$$

Let us derive the inter particle force and torque between magnetic particle i and j with magnetic dipole moment $m_i$ and $m_j$ respectively:

$$m_i = M\{\, dp_ix,\, dp_iy,\, dp_iz \,\} \tag{22}$$

$$m_j = M\{dp_jx,\, dp_jy,\, dp_jz\} \tag{23}$$

$dp_ix$, $dp_iy$, $dp_iz$ are the unit vectors of the local co-ordinate system situated in the center of mass of the particle i. The displacement vector of particle i from particle j is $r_{ij}$ which is as follows:

$$r_{ij} = \{x_i - x_j, y_i - y_j, z_i - z_j\}$$

$$\therefore r_{ji} = \{x_j - x_i, y_j - y_i, z_j - z_i\} \quad (24)$$

So the square of the inter particle distance will be

$$r_{ij}sq = (x_i - x_j)^2 + (y_i - y_j)^2 + (z_i - z_j)^2; \quad (25)$$

The magnetic density flux due to particle i and the center of mass of the particle j is given by equation 18. Lets assume $C_1 = \mu_0 / (4 \pi r_{ij}^5)$. Then from equation 3 we can write $b_i$ and $b_j$ the magnetic densities due to $m_j$ and $m_i$ respectively acting on other particle's mass center.

$$b_i = C_1 ( 3 (m_i \bullet r_{ji}) r_{ji} - r_{ji}sq\ m_i) \quad (26)$$

$$b_j = C_1 ( 3 (m_j \bullet r_{ij}) r_{ij} - r_{ij}sq\ m_j) \quad (27)$$

The force acting on particle I for the other particle j is given by:

$$Fij = \nabla_i ( f ) \text{ where } f = m_i . \bullet b_j \quad (28)$$

Then by the definition of the del operator we can we can write Fij in the form:

$$\mathbf{Fij} = \frac{\mathbf{df}}{\mathbf{dx_i}} + \frac{\mathbf{df}}{\mathbf{dy_i}} + \frac{\mathbf{df}}{\mathbf{dz_i}}$$

$$Fij = \{D[f, x_i], D[f, y_i], D[f, z_i]\} \quad (29)$$

The three components of Fij obtained will be as follows:

$$(Fij)_x = C_1\ dp_iy\ M\ (-2\ dp_jy\ M\ (x_i - x_j) + 3\ dp_jx\ M\ (y_i - y_j)) + C_1\ dp_ix\ M\ (dp_jx\ M\ (x_i - x_j) + 3\ (dp_jx\ M\ (x_i - x_j) + dp_jy\ M\ (y_i - y_j) + dp_jz\ M\ (z_i - z_j))) + C_1\ dp_iz\ M\ (-2\ dp_jz\ M\ (x_i - x_j) + 3\ dp_jx\ M\ (z_i - z_j)) \quad (30)$$

$$(Fij)_y = C_1\ dp_ix\ M\ (3\ dp_jy\ M\ (x_i - x_j) - 2\ dp_jx\ M\ (y_i - y_j)) + C_1\ dp_iy\ M\ (dp_jy\ M\ (y_i - y_j) + 3\ (dp_jx\ M\ (x_i - x_j) + dp_jy\ M\ (y_i - y_j) + dp_jz\ M\ (z_i - z_j))) + C_1\ dp_iz\ M\ (-2\ dp_jz\ M\ (y_i - y_j) + 3\ dp_jy\ M\ (z_i - z_j)) \quad (31)$$

$$(Fij)_z = C_1\ dp_ix\ M\ (3\ dp_jz\ M\ (x_i - x_j) - 2\ dp_jx\ M\ (z_i - z_j)) + C_1\ dp_iy\ M\ (3\ dp_jz\ M\ (y_i - y_j) - 2\ dp_jy\ M\ (z_i - z_j)) + C_1\ dp_iz\ M\ (3\ (dp_jx\ M\ (x_i - x_j) + dp_jy\ M\ (y_i - y_j) + dp_jz\ M\ (z_i - z_j)) + dp_jz\ M\ (z_i - z_j)) \quad (32)$$

Similarly if the force on particle j is calculated for the effect of the magnetic flux density at its mass center due to the influence of i th particle the equation of force is as follows:

$fa = m_j.b_i$

$$\mathbf{Fji} = \frac{\mathbf{dfa}}{\mathbf{dx_j}} + \frac{\mathbf{dfa}}{\mathbf{dy_j}} + \frac{\mathbf{dfa}}{\mathbf{dz_j}}$$

The three components of Fji will be as follows:

$$(Fji)_x = C_1\ \ dp_jy\ M\ (-2\ dp_iy\ M\ (-x_i + x_j) + 3\ dp_ix\ M\ (-y_i + y_j)) + C_i\ dp_jz\ M\ (-2\ dp_iz\ M\ (-x_i + x_j) + 3\ dp_ix\ M\ (-z_i + z_j)) + C_1\ dp_jx\ M\ (dp_ix\ M\ (-x_i + x_j) + 3\ (dp_ix\ M\ (-x_i + x_j) + dp_iy\ M\ (-y_i + y_j) + dp_iz\ M\ (-z_i + z_j))) \quad (33)$$

$$(Fji)_y = C_1\ dp_jx\ M\ (3\ dp_iy\ M\ (-x_i + x_j) - 2\ dp_ix\ M\ (-y_i + y_j)) + C_1\ dp_jz\ M\ (-2\ dp_iz\ M\ (-y_i + y_j) + 3\ dp_iy\ M\ (-z_i + z_j)) + C_1\ dp_jy\ M\ (dp_iy\ M\ (-y_i + y_j) + 3\ (dp_ix\ M\ (-x_i + x_j) + dp_iy\ M\ (-y_i + y_j) + dp_iz\ M\ (-z_i + z_j))) \quad (34)$$

$$(Fji)_z = C_1\, dp_j x\, M\,(3\, dp_i z\, M\,(-x_i + x_j) - 2\, dp_i x\, M\,(-z_i + z_j)) + C_1\, dp_j y\, M\,(3\, dp_i z\, M\,(-y_i + y_j) - 2\, dp_i y\, M\,(-z_i + z_j)) + C_1\, dp_j z\, M\,(dp_i z\, M\,(-z_i + z_j) + 3\,(dp_i x\, M\,(-x_i + x_j) + dp_i y\, M\,(-y_i + y_j) + dp_i z\, M\,(-z_i + z_j))) \quad (35)$$

It is clear from above that the forces Fij and Fji are equal and opposite.

The inter particle torque is calculated using the equation $Tij = m_i \times b_j$ is the torque on particle I due to the field created by particle j. Similarly the torque on particle j due to the influence of particle i should be $Tji = m_j \times b_j$. Now if the RHS of the torque equation is expanded we get:

$$(Tij)_x = (m_i \times b_j)_x$$

$$= C_1\, dp_i z\, dp_j y\, M^2\, x_i^2 - C_1\, dp_i y\, dp_j z\, M^2\, x_i^2 - 2\, C_1\, dp_i z\, dp_j y\, M^2\, x_i\, x_j + 2\, C_1\, dp_i y\, dp_j z\, M^2\, x_i\, x_j + C_1\, dp_i z\, dp_j y\, M^2\, x_j^2 - C_1\, dp_i y\, dp_j z\, M^2\, x_j^2 - 3\, C_1\, dp_i z\, dp_j x\, M^2\, x_i\, y_i + 3\, C_1\, dp_i z\, dp_j x\, M^2\, x_j\, y_i - 2\, C_1\, dp_i z\, dp_j y\, M^2\, y_i^2 - C_1\, dp_i y\, dp_j z\, M^2\, y_i^2 + 3\, C_1\, dp_i z\, dp_j x\, M^2\, x_i\, y_j - 3\, C_1\, dp_i z\, dp_j x\, M^2\, x_j\, y_j + 4\, C_1\, dp_i z\, dp_j y\, M^2\, y_i\, y_j + 2\, C_1\, dp_i y\, dp_j z\, M^2\, y_i\, y_j - 2\, C_1\, dp_i z\, dp_j y\, M^2\, y_j^2 - C_1\, dp_i y\, dp_j z\, M^2\, y_j^2 + 3\, C_1\, dp_i y\, dp_j x\, M^2\, x_i\, z_i - 3\, C_1\, dp_i y\, dp_j x\, M^2\, x_j\, z_i + 3\, C_1\, dp_i y\, dp_j y\, M^2\, y_i\, z_i - 3\, C_1\, dp_i z\, dp_j z\, M^2\, y_i\, z_i - 3\, C_1\, dp_i y\, dp_j y\, M^2\, y_j\, z_i + 3\, C_1\, dp_i z\, dp_j z\, M^2\, y_j\, z_i + C_1\, dp_i z\, dp_j y\, M^2\, z_i^2 + 2\, C_1\, dp_i y\, dp_j z\, M^2\, z_i^2 - 3\, C_1\, dp_i y\, dp_j x\, M^2\, x_i\, z_j + 3\, C_1\, dp_i y\, dp_j x\, M^2\, x_j\, z_j - 3\, C_1\, dp_i y\, dp_j y\, M^2\, y_i\, z_j + 3\, C_1\, dp_i z\, dp_j z\, M^2\, y_i\, z_j + 3\, C_1\, dp_i y\, dp_j y\, M^2\, y_j\, z_j - 3\, C_1\, dp_i z\, dp_j z\, M^2\, y_j z_j - 2\, C_1\, dp_i z\, dp_j y\, M^2\, z_i\, z_j - 4\, C_1\, dp_i y dp_j z\, M^2\, z_i\, z_j + C_1\, dp_i z\, dp_j y\, M^2\, z_j^2 + 2\, C_1\, dp_i y\, dp_j z\, M^2\, z_j^2 \quad (36)$$

$$(Tij)_y = (m_i \times b_j)_y$$

$$= 2\,C_1\,dp_iz\,dp_jx\,M^2\,x_i^2 + C_1\,dp_ix\,dp_jz\,M^2\,x_i^2 - 4\,C_1\,dp_iz\,dp_jx\,M^2\,x_i\,x_j - 2\,C_1\,dp_ix\,dp_jz\,M^2\,x_i\,x_j + 2\,C_1\,dp_iz\,dp_jx\,M^2\,x_j^2 + C_1\,dp_ix\,dp_jz\,M^2\,x_j^2 + 3\,C_1\,dp_iz\,dp_jy\,M^2\,x_i\,y_i - 3\,C_1\,dp_iz\,dp_jy\,M^2\,x_j\,y_i - C_1\,dp_iz\,dp_jx\,M^2\,y_i^2 + C_1\,dp_ix\,dp_jz\,M^2\,y_i^2 - 3\,C_1\,dp_iz\,dp_jy\,M^2\,x_i\,y_j + 3\,C_1\,dp_iz\,dp_jy\,M^2\,x_j\,y_j + 2\,C_1\,dp_iz\,dp_jx\,M^2\,y_i\,y_j - 2\,C_1\,dp_ix\,dp_jz\,M^2\,y_i\,y_j - C_1\,dp_iz\,dp_jx\,M^2\,y_j^2 + C_1\,dp_ix\,dp_jz\,M^2\,y_j^2 - 3\,C_1\,dp_ix\,dp_jx\,M^2\,x_i\,z_i + 3\,C_1\,dp_iz\,dp_jz\,M^2\,x_i\,z_i + 3\,C_1\,dp_ix\,dp_jx\,M^2\,x_j\,z_i - 3\,C_1\,dp_iz\,dp_jz\,M^2\,x_j\,z_i - 3\,C_1\,dp_ix\,dp_jy\,M^2\,y_i\,z_i + 3\,C_1\,dp_ix\,dp_jy\,M^2\,y_j\,z_i - C_1\,dp_iz\,dp_jx\,M^2\,z_i^2 - 2\,C_1\,dp_ix\,dp_jz\,M^2\,z_i^2 + 3\,C_1\,dp_ix\,dp_jx\,M^2\,x_i\,z_j - 3\,C_1\,dp_iz\,dp_jz\,M^2\,x_i\,z_j - 3\,C_1\,dp_ix\,dp_jx\,M^2\,x_j\,z_j + 3\,C_1\,dp_iz\,dp_jz\,M^2\,x_j\,z_j + 3\,C_1\,dp_ix\,dp_jy\,M^2\,y_i\,z_j - 3\,C_1\,dp_ix\,dp_jy\,M^2\,y_j\,z_j + 2\,C_1\,dp_iz\,dp_jx\,M^2\,z_i\,z_j + 4\,C_1\,dp_ix\,dp_jz\,M^2\,z_i\,z_j - C_1\,dp_iz\,dp_jx\,M^2\,z_j^2 - 2\,C_1\,dp_ix\,dp_jz\,M^2\,z_j^2 \qquad (37)$$

$$(Tij)_z = (m_i \times b_j)_z$$

$$= -2\,C_1\,dp_iy\,dp_jx\,M^2\,x_i^2 - C_1\,dp_ix\,dp_jy\,M^2\,x_i^2 + 4\,C_1\,dp_iy\,dp_jx\,M^2\,x_i\,x_j + 2\,C_1\,dp_ix\,dp_jy\,M^2\,x_i\,x_j - 2\,C_1\,dp_iy\,dp_jx\,M^2\,x_j^2 - C_1\,dp_ix\,dp_jy\,M^2\,x_j^2 + 3\,C_1\,dp_ix\,dp_jx\,M^2\,x_i\,y_i - 3\,C_1\,dp_iy\,dp_jy\,M^2\,x_i\,y_i - 3\,C_1\,dp_ix\,dp_jx\,M^2\,x_j\,y_i + 3\,C_1\,dp_iy\,dp_jy\,M^2\,x_j\,y_i + C_1\,dp_iy\,dp_jx\,M^2\,y_i^2 + 2\,C_1\,dp_ix\,dp_jy\,M^2\,y_i^2 - 3\,C_1\,dp_ix\,dp_jx\,M^2\,x_i\,y_j + 3\,C_1\,dp_iy\,dp_jy\,M^2\,x_i\,y_j + 3\,C_1\,dp_ix\,dp_jx\,M^2\,x_j\,y_j - 3\,C_1\,dp_iy\,dp_jy\,M^2\,x_j\,y_j - 2\,C_1\,dp_iy\,dp_jx\,M^2\,y_i\,y_j - 4\,C_1\,dp_ix\,dp_jy\,M^2\,y_i\,y_j + C_1\,dp_iy\,dp_jx\,M^2\,y_j^2 + 2\,C_1\,dp_ix\,dp_jy\,M^2\,y_j^2 - 3\,C_1\,dp_iy\,dp_jz\,M^2\,x_i\,z_i + 3\,C_1\,dp_iy\,dp_jz\,M^2\,x_j\,z_i + 3\,C_1\,dp_ix\,dp_jz\,M^2\,y_i\,z_i - 3\,C_1\,dp_ix\,dp_jz\,M^2\,y_j\,z_i + C_1\,dp_iy\,dp_jx\,M^2\,z_i^2 - C_1\,dp_ix\,dp_jy\,M^2\,z_i^2 + 3\,C_1\,dp_iy\,dp_jz\,M^2\,x_i\,z_j - 3\,C_1\,dp_iy\,dp_jz\,M^2\,x_j\,z_j - 3\,C_1\,dp_ix\,dp_jz\,M^2\,y_i\,z_j + 3\,C_1\,dp_ix\,dp_jz\,M^2\,y_j\,z_j$$

$$- 2\,C_1\,dp_i y\,dp_j x\,M^2\,z_i\,z_j + 2\,C_1\,dp_i x\,dp_j y\,M^2\,z_i\,z_j + C_1\,dp_i y\,dp_j x\,M^2\,z_j^2 - C_1\,dp_i x\,dp_j y\,M^2\,z_j^2 \quad (38)$$

Similarly the components of the torque on particle j in the influence of the particle number i are as follows:

$$(Tji)_x = (m_j \times b_i)_x$$

$$= - C_1\,dp_i z\,dp_j y\,M^2\,x_i^2 + C_1\,dp_i y\,dp_j z\,M^2\,x_i^2 + 2\,C_1\,dp_i z\,dp_j y\,M^2\,x_i\,x_j - 2\,C_1\,dp_i y\,dp_j z\,M^2\,x_i\,x_j - C_1\,dp_i z\,dp_j y\,M^2\,x_j^2 + C_1\,dp_i y\,dp_j z\,M^2\,x_j^2 - 3\,C_1\,dp_i x\,dp_j z\,M^2\,x_i\,y_i + 3\,C_1\,dp_i x\,dp_j z\,M^2\,x_j\,y_i - C_1\,dp_i z\,dp_j y\,M^2\,y_i^2 - 2\,C_1\,dp_i y\,dp_j z\,M^2\,y_i^2 + 3\,C_1\,dp_i x\,dp_j z\,M^2\,x_i\,y_j - 3\,C_1\,dp_i x\,dp_j z\,M^2\,x_j\,y_j + 2\,C_1\,dp_i z\,dp_j y\,M^2\,y_i\,y_j + 4\,C_1\,dp_i y\,dp_j z\,M^2\,y_i\,y_j - C_1\,dp_i z\,dp_j y\,M^2\,y_j^2 - 2\,C_1\,dp_i y\,dp_j z\,M^2\,y_j^2 + 3\,C_1\,dp_i x\,dp_j y\,M^2\,x_i\,z_i - 3\,C_1\,dp_i x\,dp_j y\,M^2\,x_j\,z_i + 3\,C_1\,dp_i y\,dp_j y\,M^2\,y_i\,z_i - 3\,C_1\,dp_i z\,dp_j z\,M^2\,y_i\,z_i - 3\,C_1\,dp_i y\,dp_j y\,M^2\,y_j\,z_i + 3\,C_1\,dp_i z\,dp_j z\,M^2\,y_j\,z_i + 2\,C_1\,dp_i z\,dp_j y\,M^2\,z_i^2 + C_1\,dp_i y\,dp_j z\,M^2\,z_i^2 - 3\,C_1\,dp_i x\,dp_j y\,M^2\,x_i\,z_j + 3\,C_1\,dp_i x\,dp_j y\,M^2\,x_j\,z_j - 3\,C_1\,dp1y\,dp_j x\,M^2\,y_i\,z_j - 3\,C_1\,dp1y\,dp_j x\,M^2\,y_j\,z_j + 4\,C_1\,dp_i z\,dp_j x\,M^2\,z_i\,z_j + 2\,C_1\,dp_i x\,dp_j z\,M^2\,z_i\,z_j - 3\,C_1\,dp_i y\,dp_j y\,M^2\,y_1\,z_j + 3\,C_1\,dp_i z\,dp_j z\,M^2\,y_i\,z_j + 3\,C_1\,dp_i y\,dp_j y\,M^2\,y_j\,z_j - 3\,C_1\,dp_i z\,dp_j z\,M^2\,y_j\,z_j - 4\,C_1\,dp_i z\,dp_j y\,M^2\,z_i\,z_j - 2\,C_1\,dp_i y\,dp_j z\,M^2\,z_i\,z_j + 2\,C_1\,dp_i z\,dp_j y\,M^2\,z_j^2 + C_1\,dp_i y\,dp_j z\,M^2\,z_j^2 \quad (39)$$

$$(Tji)_y = (m_j \times b_i)_y$$

$$= C_1\,dp_i z\,dp_j x\,M^2\,x_i^2 + 2\,C_1\,dp_i x\,dp_j z\,M^2\,x_i^2 - 2\,C_1\,dp_i z\,dp_j x\,M^2\,x_i\,x_j - 4\,C_1\,dp_i x\,dp_j z\,M^2\,x_i\,x_j + C_1\,dp_i z\,dp_j x\,M^2\,x_j^2 + 2\,C_1\,dp_i x\,dp_j z\,M^2\,x_j^2 + 3\,C_1\,dp_i y\,dp_j z\,M^2\,x_i\,y_i - 3\,C_1\,dp_i y\,dp_j z\,M^2\,x_j\,y_i + C_1\,dp_i z\,dp_j x\,M^2\,y_i^2 - C_1\,dp_i x\,dp_j z\,M^2\,y_i^2 - 3\,C_1\,dp_i y$$

$dp_jz\ M^2\ x_i\ y_j + 3\ C_1\ dp_iy\ dp_jz\ M^2\ x_j\ y_j - 2\ C_1\ dp_iz\ dp_jx\ M^2\ y_i\ y_j + 2\ C_1\ dp_ix\ dp_jz\ M^2\ y_i\ y_j + C_1\ dp_iz\ dp_jx\ M^2\ y_j^2 - C_1\ dp_ix\ dp_jz\ M^2\ y_j^2 - 3\ C_1\ dp_ix\ dp_jx\ M^2\ x_i\ z_i + 3\ C_1\ dp_iz\ dp_jz\ M^2\ x_i\ z_i + 3\ C_1\ dp_ix\ dp_jx\ M^2\ x_j\ z_i - 3\ C_1\ dp_iz\ dp_jz\ M^2\ x_j\ z_i - 3\ C_1\ dp_iy\ dp_jx\ M^2\ y_i\ z_i + 3\ C_1\ dp_iy\ dp_jx\ M^2\ y_j\ z_i - 2\ C_1\ dp_iz\ dp_jx\ M^2\ z_i^2 - C_1\ dp_ix\ dp_jz\ M^2\ z_i^2 + 3\ C_1\ dp_ix\ dp_jx\ M^2\ x_i\ z_j - 3\ C_1\ dp_iz\ dp_jz\ M^2\ x_i\ z_j - 3\ C_1\ dp_ix\ dp_jx\ M^2\ x_j\ z_j + 3\ C_1\ dp_iz\ dp_jz\ M^2\ x_j\ z_j + 2\ C_1\ dp_iz\ dp_jx\ M^2\ z_j^2 - C_1\ dp_ix\ dp_jz\ M^2\ z_j^2$ (40)

$(Tji)_z = (m_j \times b_i)_z$

$= -C_1\ dp_iy\ dp_jx\ M^2\ x_i^2 - 2\ C_1\ dp_ix\ dp_jy\ M^2\ x_i^2 + 2\ C_1\ dp_iy\ dp_jx\ M^2\ x_i\ x_j + 4\ C_1\ dp_ix\ dp_jy\ M^2\ x_i\ x_j - C_1\ dp_iy\ dp_jx\ M^2\ x_j^2 - 2\ C_1\ dp_ix\ dp_jy\ M^2\ x_j^2 + 3\ C_1\ dp_ix\ dp_jx\ M^2\ x_i\ y_i - 3\ C_1\ dp_iy\ dp_jy\ M^2\ x_i\ y_i - 3\ C_1\ dp_ix\ dp_jx\ M^2\ x_j\ y_i + 3\ C_1\ dp_iy\ dp_jy\ M^2\ x_j\ y_i + 2\ C_1\ dp_iy\ dp_jx\ M^2\ y_i^2 + C_1\ dp_ix\ dp_jy\ M^2\ y_i^2 - 3\ C_1\ dp_ix\ dp_jx\ M^2\ x_i\ y_j + 3\ C_1\ dp_iy\ dp_jy\ M^2\ x_i\ y_j + 3\ C_1\ dp_ix\ dp_jx\ M^2\ x_j\ y_j - 3\ C_1\ dp_iy\ dp_jy\ M^2\ x_j\ y_j - 4\ C_1\ dp_iy\ dp_jx\ M^2\ y_i\ y_j - 2\ C_1\ dp_ix\ dp_jy\ M^2\ y_i\ y_j + 2\ C_1\ dp_iy\ dp_jx\ M^2\ y_j^2 + C_1\ dp_ix\ dp_jy\ M^2\ y_j^2 - 3\ C_1\ dp_iz\ dp_jy\ M^2\ x_i\ z_i + 3\ C_1\ dp_iz\ dp_jy\ M^2\ x_j\ z_i + 3\ C_1\ dp_iz\ dp_jx\ M^2\ y_i\ z_i - 3\ C_1\ dp_iz\ dp_jx\ M^2\ y_j\ z_i - C_1\ dp_iy\ dp_jx\ M^2\ z_i^2 + C_1\ dp_ix\ dp_jy\ M^2\ z_i^2 + 3\ C_1\ dp_iz\ dp_jy\ M^2\ x_i\ z_j - 3C_1dp_izdp_jyM^2\ x_j\ z_j - 3C_1dp_iz\ dp_jxM^2y_i\ z_j + 3C_1dp_izdp_jxM^2y_j\ z_j + 2C_1\ dp_iy\ dp_jx\ M^2\ z_i\ z_j - 2C_1\ dp_ix\ dp_jy\ M^2\ z_i\ z_j - C_1dp_iy\ dp_jx\ M^2\ z_j^2 + C_1dp_ixdp_jy\ M^2\ z_j^2$ (41)

### 4.2.4 Determination of Transformation Matrix for Animation

The quaternion vector is derived from the Euler angles and necessary to determine the orientation of each of the particles. At **init.c** during the initialization the first three quaternion q1, q2, q3 are set to zero for all particles. The last member of the quaternion, q4 is assigned to 1. In all the timesteps the quaternion are updated in **integ.c** using the

quaternion of the earlier timestep and the current rotational velocities. Then the transformation matrix ( rotmat[i][j] , where i is the particle number and j = 0,1,2…15, in C language the numbering of array element starts at zero) for each of the particle is determined using the following equations:

rotmat[i][0] =- q1×q1 + q2×q2 – q3×q3 + q4×q4;

rotmat[i][5] = q1×q1 - q2×q2 - q3×q3 + q4×q4;

rotmat[i][10]=- q1×q1 - q2×q2 + q3×q3 + q4×q4;

rotmat[i][4] =-2.0× (q3×q4 + q1×q2);

rotmat[i][1] = 2.0 × (q3×q4 - q1×q2);

rotmat[i][8] = 2.0 × (q2×q3 - q1×q4);

rotmat[i][2] = 2.0 × ( q2×q3 + q1×q4);

rotmat[i][9] =-2.0 × (q2×q4 + q1×q3);

rotmat[i][6] = 2.0 × (q2×q4 - q1×q3);

The four other elements of this matrix are the Cartesian co-ordinates of the particle and 1 in the homogenous transformation matrix.

rotmat[i][3] = 0.0; rotmat[i][7] = 0.0; rotmat[i][11]= 0.0; rotmat[i][15]= 1.0;

Each of the magnetic particle has its own local coordinate system and it changes its direction at every timestep for the rotation. So the unit vectors specifying the coordinate system will be transformed by the 3×3 part of the transformation

matrix(rotmat) which accounts for the rotation. The updating of the unit vectors of the local coordinate system(newdpx, newdpy, newdpz) for particle number i is done in the following steps.

newdpx = rotmat[i][0] × dpx[i] + rotmat[i][4] × dpy[i] + rotmat[i][8] × dpz[i];

newdpy = rotmat[i][1] × dpx[i] + rotmat[i][5] × dpy[i] + rotmat[i][9] × dpz[i];

newdpz = rotmat[i][2] × dpx[i] + rotmat[i][6] × dpy[i] + rotmat[i][10] × dpz[i];

where dpx[i], dpy[i] and dpz[i] were the unit vectors of the local co-ordinate system at earlier time step and the current.

### 4.3 Device Scale Simulation Results

In this section, results from a preliminary simulation study are presented. The cases considered in this section were selected to provide a qualitative explanation of the experimental results presented in this paper, and to examine the scalability of this approach. In this study, a rectangular simulation box of size 2.5 cm × 2.5 cm × 6 cm was used. This size is selected to approximately match the experimental apparatus. Later in this section (see 4.3), we discuss the issue of the scale-up of this unit. Initially, the particles, magnetic and/or non-magnetic, were placed randomly throughout the box, and were allowed to fall under gravity. The inter-particle interactions, other than the magnetic ones, include a Hertz-like normal contact with a linear spring that has a different value of stiffness for loading and unloading [34], a Hertz-Mindlin type tangential compliance [17], and friction. The particles were considered to be non-cohesive.

We note that the magnetic field used in our simulations was assumed to be generated by an infinite solenoid. Thus as may be observed from equation (6), if a single particle in the system was initially aligned with the direction of the magnetic flux, it would not experience any torque, and would remain at rest. The actual coils used in our experiments were not like a solenoid, and have a rotating magnetic field (direction of the field itself is rotating), thus the simulation results presented here represent a conservative case.

### 4.3.1. Simulation of Magnetic Particles under Various Conditions

The first series of results consider the motion of the magnetic particles alone. While the behavior of the 1g of magnets within 40g of cornstarch would be much different than that of 1g of magnets alone, these results show the nature of fluidization and the effect of various parameters on fluidization. First, we show the effect of the varying the mass (or total amount) of magnets within the simulation box.

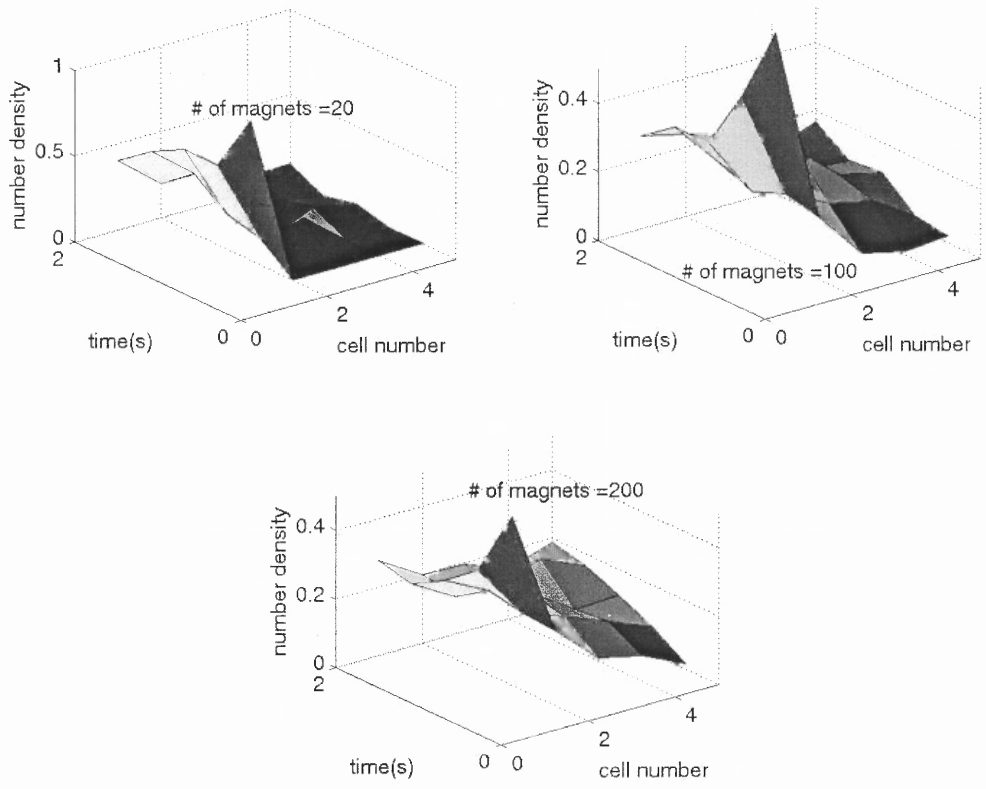


**Figure 4.2** Simulation results for number density evolution of the magnetic particles as a function of the total mass of magnets.

The state of fluidization is shown by considering the number density distribution in the box. The box is divided into five horizontal cells, and the number density within each cell (number of particles in the cell divided by the total number of particles in the simulation volume) is computed as a function of time. Here, the number density values vary between 0 and 1, where the value of 1 for a given cell means that all the particles in the box are in that cell. Hence a uniform distribution would be indicated by a constant value of 0.2 in each cell. In Fig. 4.2, three cases of the number of magnets within the box are considered, 20 magnets, 100 magnets, and 200 magnets (e.g. 100 magnets correspond to 3.2 g mass for a spherical particle of 2.36 mm). The time evolution of the number density is shown

for each case. At each time, the results shown are instantaneous snap-shots of the number density distribution. As can be observed, the state of fluidization increases as the total mass of the magnets increases. Since the amount of fluidization may affect the flowability of the material to a great extent, these results are in line with the experimental results[37](in section 3.2, and in Fig. 5). Moreover, the time evolution indicates that the fluidization is fairly random and does not change significantly with time after 1 sec.

In Fig. 4.3, the effect of the magnetic flux density on fluidization is examined. The simulation cell was the same size and 50 magnets were placed in the cell. The flux density was varied by increasing the number of turns of the coil at a constant current of 5 A. Three cases are shown, 5600 amp-turns/m, 28000 amp-turns/m, and 56000 amp-turns/m. Note that the scale of the plot in the last two cases is different from the first one. As can be expected, the state of fluidization, indicated by a more uniform distribution of the magnets, is higher in the case of 56000 amp-turns/m. These results are in line with the experimental results[37]( in section 3.3, and in Fig. 6). It is noted that the state of fluidization denoted by the number density distribution is only one of several indications of increased flowability. Another way to increase the magnetic flux density is by increasing the current. This is shown in the next set of results, where instead of plotting the number density evolution, we plot the averaged number density distributions during the simulation time period of from 1 to 5 sec. The results are plotted in Fig. 4.4, showing a distinct increase in fluidization as the current is increased. The increase in the

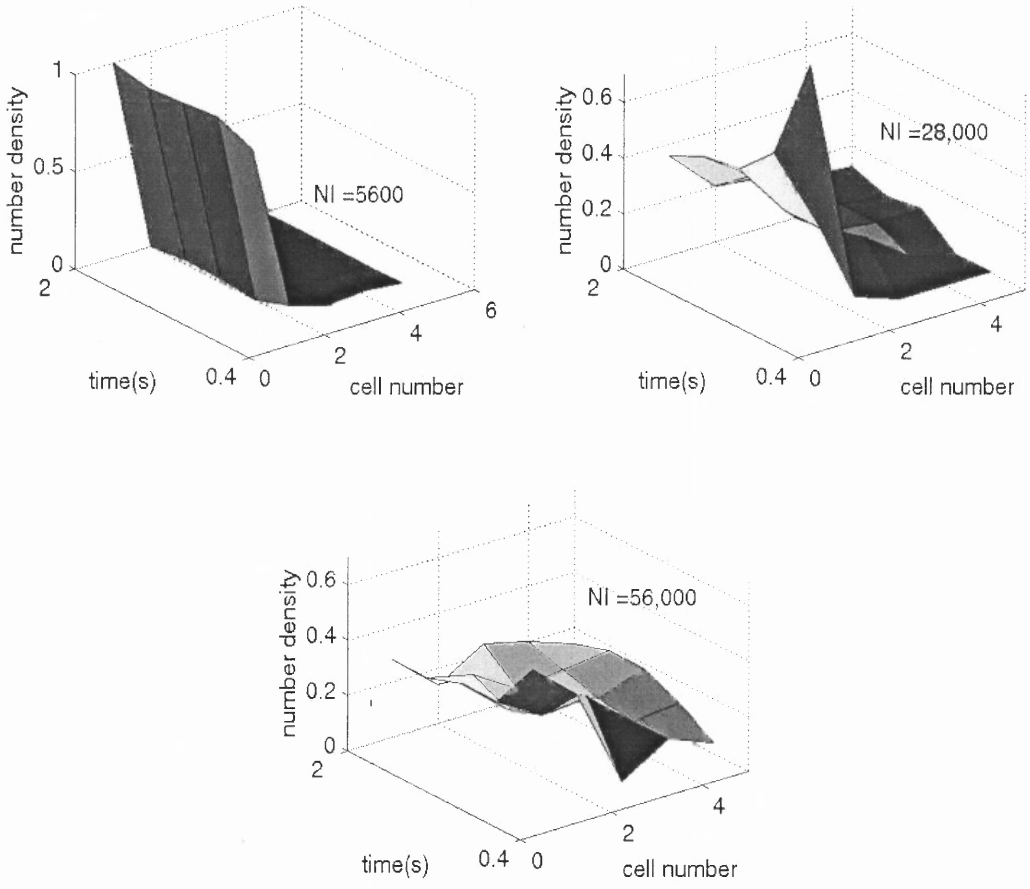


**Figure 4.3** Simulation results for number density evolution of the magnetic particles as a function of the magnetic field strength (varied by changing the number of turns in the coil).

fluidization from 5 amps to 10 amps is less significant than as from 1 amp to 5 amps. Next, the effect of varying the magnet size while keeping the total mass of the magnets constant is considered. Three magnet sizes were considered, and the averaged number density distributions during the simulation time period from 1 to 5 sec are plotted in Fig. 4.5. The total mass of the magnets in each case is the same, 1.6 grams.

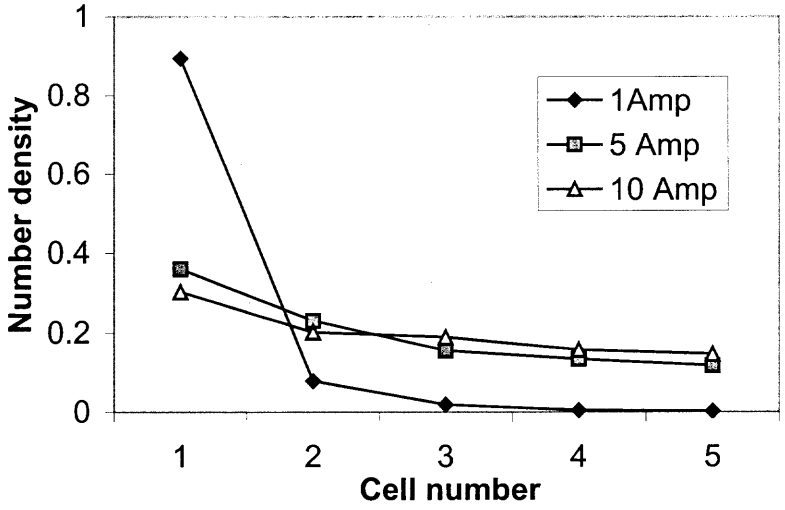


**Figure 4.4** Simulation results for the time-averaged number density of magnetic particles as a function of the magnetic field strength (varied by changing the current in the coil).

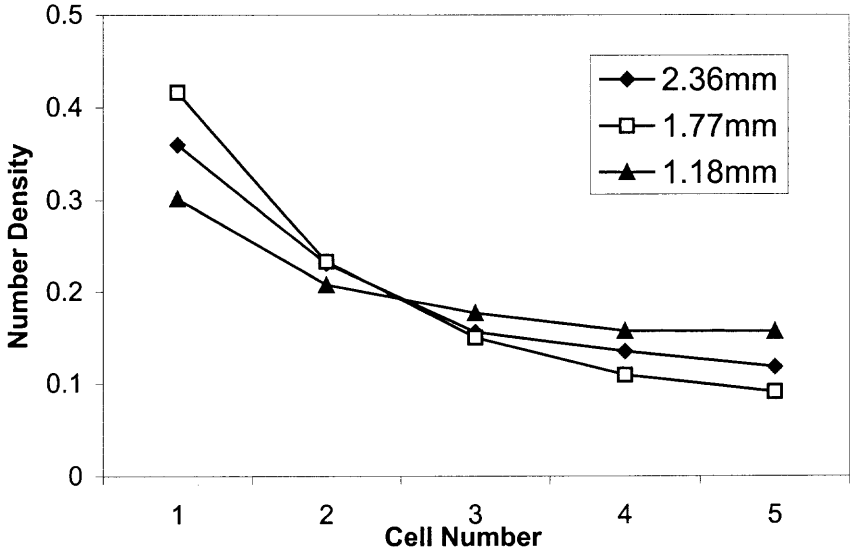


**Figure 4.5** Simulation results for the time-averaged number density of magnetic particles as a function of the size of magnetic particle(keeping total mass of magnets constant at 1.6g).

These results indicate that one cannot determine the total effect of the change in magnetic particle size on the powder flow by looking at the fluidization of the magnets alone.

### 4.3.2 Simulation of The Mixture of Magnetic and Nonmagnetic Particles

The second series of results are for the case of mixture of magnetic and non-magnetic particles. This system has 50 magnetic particles and 1000 non-magnetic particles of density 1.19 g/cc (magnets have a density of 4.7 g/cc). While the number ratio of magnetic and non-magnetic particles is not comparable to a real system , we can get some indication of the ability of magnets to fluidize non-magnets due to collisions. The results

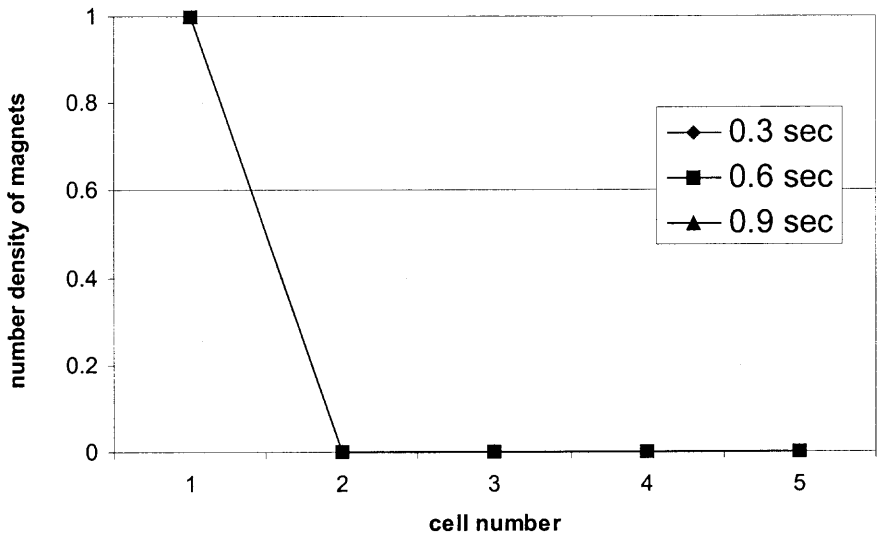


**Figure 4.6(a)** Simulation results for number density evolution of magnets in a mixed system.

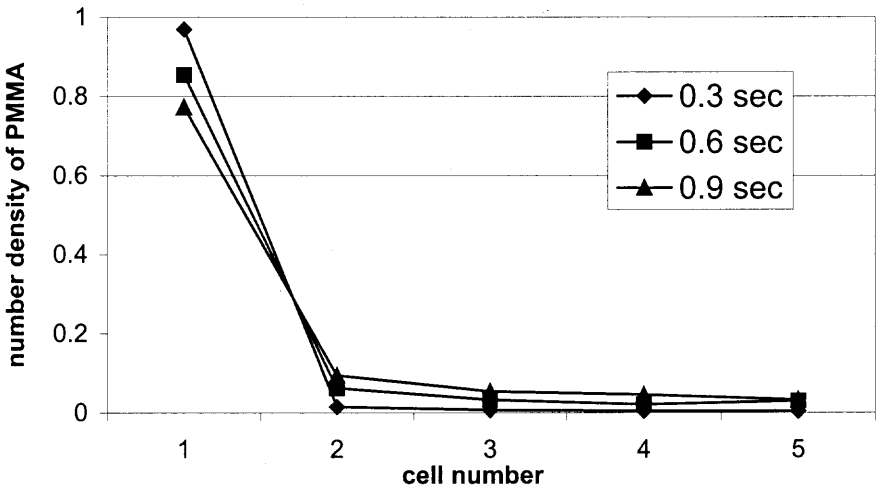


**Figure 4.6(b)** Simulation results for number density evolution of non magnetic particles in a mixed system.

are shown in Fig. 4.6, where (a) shows the number density distribution of magnetic particles as a function of time (each of the three curves is at a different time), and (b) shows the same for the non-magnetic particles. Both types of particles are fluidized, however, at the end of the run (0.9 sec), the magnets show very little fluidization, but they are able to fluidize the non-magnets. In these figures, it appears that when non-magnets are placed along with magnets, the fluidization level of the magnets significantly diminishes. However, for the flow of the non-magnets to occur, only a small level of agitation may be required. To understand how all the non-magnetic particles are affected, we present more results. In Fig. 4.7, the average of the displacement (normalized by the particle diameter) of 1000 non-magnets is plotted from time 0.2 sec until 0.3 sec, indicating that within a time span of 0.1

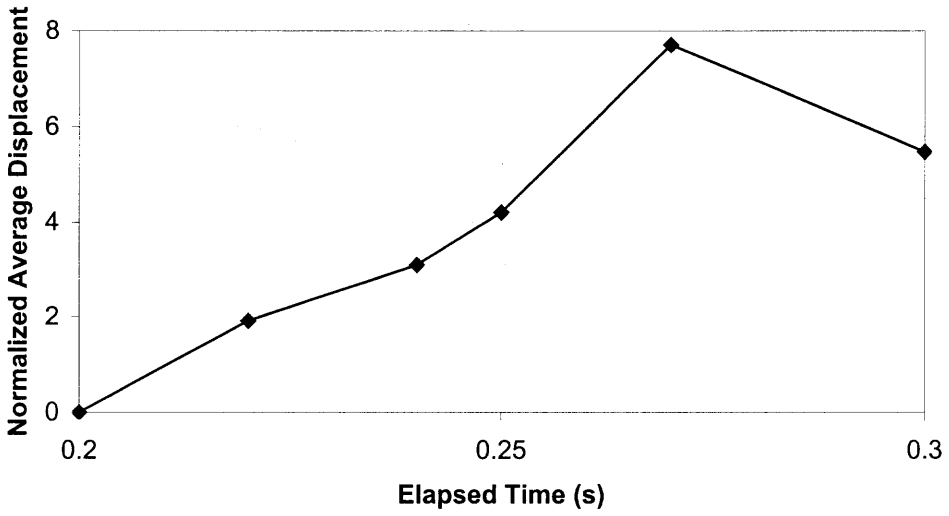


**Figure 4.7** Normalized displacement of non-magnetic particles with course of time.

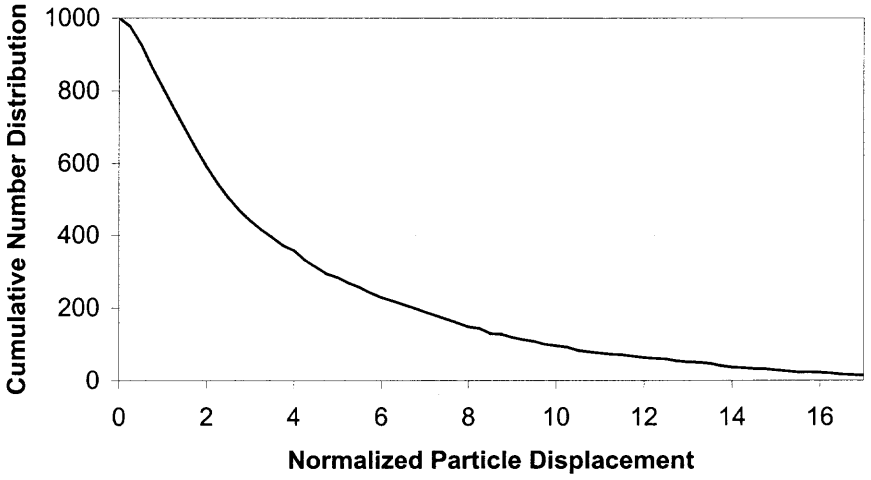


**Figure 4.8** Cumulative number distribution of the non magnetic particles.

sec, the average displacement of non-magnets is as high as 6 to 8 particle diameters. Another plot, in Fig. 4.8, shows the cumulative number distribution of the amount of

displacement experienced by 1000 non-magnets from time 0.2 sec to 0.25 sec. As can be seen, the plot indicates that the majority of the particles, i.e., over 80%, moved more than 1 particle diameter during this time, while over half of them moved more than 2.5 particle diameters. Thus these simulation results show that it is possible for the magnets to cause sufficient motion of the non-magnets so as to initiate powder flow. Excessive computational time required in making these calculations has prevented us from running the simulation for a longer period of time. We anticipate that in a time period of about 1 sec, most particles would have moved a much larger distance.

### 4.3.3 Simulations of The Magnetic Particles in Scaled-up Boxes

As mentioned before, we have selected a simulation cell size that is comparable to the experimental apparatus. In this section, we show simulation results for larger cell/box sizes. In this device, when it is scaled up, there is no need to increase the size of the magnets to compensate for a larger apparatus size assuming that the powder material is the same. In other words, for the same powder material, there is no need for any direct relation between the particle size and the cell size. In fact, this is the advantage of this approach. However, in order to excite the larger mass of powder in a larger apparatus, one must have more magnetic particles as the powder volume goes up. It is then expected that in the scale up of this device, the magnetic particle size, properties, and the magnetic field will be kept the same, but the number of magnetic particles per unit volume will be kept constant, and accordingly the total number of magnetic particles will be increased as the box size goes up.

To illustrate this point, simulations were carried out for four different sizes of cells – the original size (2.5 cm × 2.5 cm × 6 cm), one and a half times each dimension (i.e. 3.75 cm × 3.75 cm × 9 cm), doubling each dimension, and quadrupling each dimension. Thus in terms of volume, they are, the original volume, and 3.375, 8, and 64 times the original volume respectively. In each case, the total number of magnetic particles per unit volume is kept the same. To show that these systems are roughly equivalent in terms of magnetic excitation intensity, we have computed various diagnostic quantities; (1) the degree of fluidization, (2) average rotational velocity of the magnetic particles, and (3) average translational velocity of the magnetic particles, for each cell size. The results for the degree of fluidization are shown in Fig. 4.9 after 1.2 sec of elapsed time (the results at other times are similar). As can be seen, the differences between the results for different cell sizes are not significant, and the differences can be mostly attributed to wall-effects, because for smaller cells, the particles may travel a shorter distance before hitting a wall. Fig. 4.10 shows the time evolution of the rotational velocity averaged over all the magnets for each cell size. Here, the differences between the various cell sizes are insignificant. Fig. 4.11 shows the time evolution of translational velocity averaged over all the magnets for each cell size. In this case, the differences between various cell sizes are small and the larger cells show higher velocities. This behavior may also be attributed to wall-effects, as the particles in a larger cell may be able to travel further without hitting a wall. These three figures indicate that one can achieve essentially the same "scale" of magnetic fluidization and excitation by just keeping the number of particles per volume the same.

The simulation volume is also varied keeping the height constant to 6cm.The other dimensions of the box are increased by 1.5,2 and 4 times. In Fig 4.12 the number density plots at times t = 0.3, 0.9, 1.5, 1.8 seconds. The plots at t =0.3 and 0.9s it is seen that the differences between plots at different volumes are not that significant. But at higher times t = 1.5s and

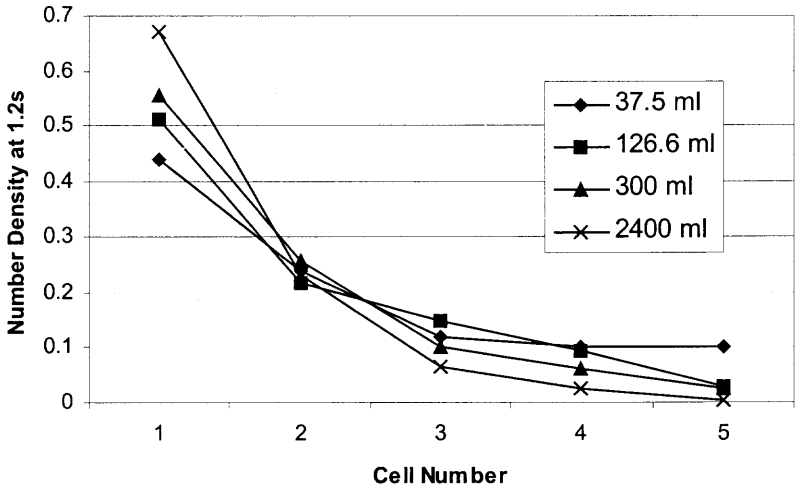


**Figure 4.9** The number densities of magnetic particles in different simulation volumes at t = 1.2s.

1.8s the differences grow higher. The average translational and rotational velocities in this constant-height scale up is plotted in Fig 4.13. The translational velocity increases with the increase of the box size in contrary to the changing-height scale up cases. The average rotational velocities of different volumes are very different from each other and don't have specific trend with the elapsed time. So scaling up of simulation box with a constant external magnetic field needs the mass of the magnets remain proportional to the volume of the box rather than the area of the box.

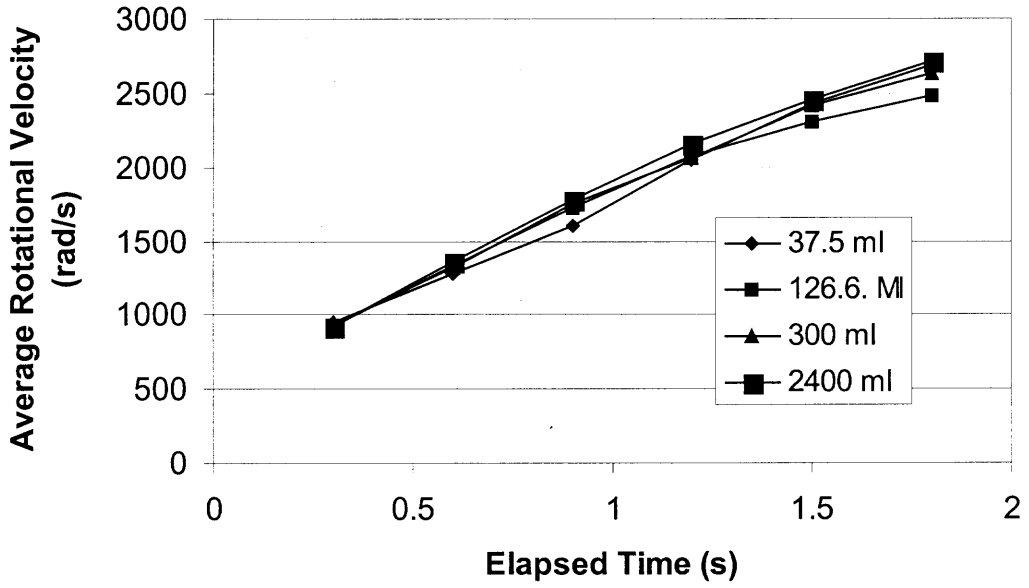


**Figure 4.10** The average rotational velocities of magnetic particle with time at different simulation volumes.

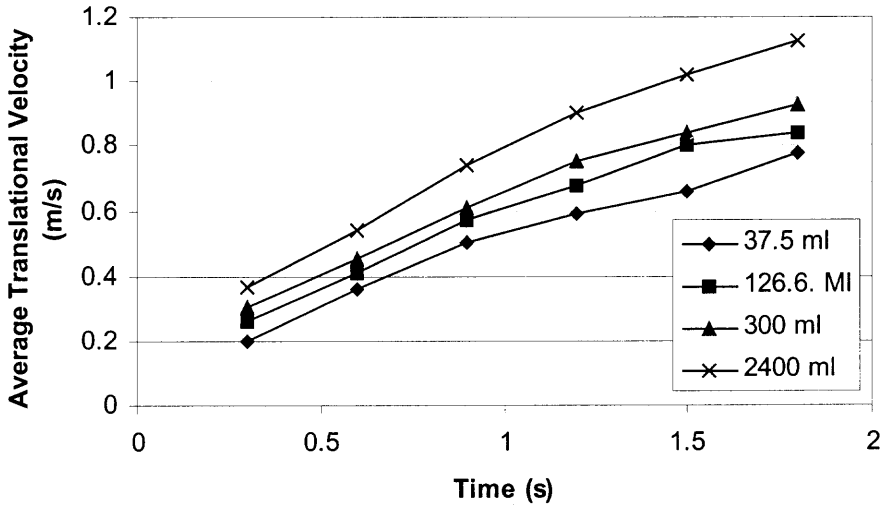


**Figure 4.11** The average translational velocity with course of time in different simulation volumes.

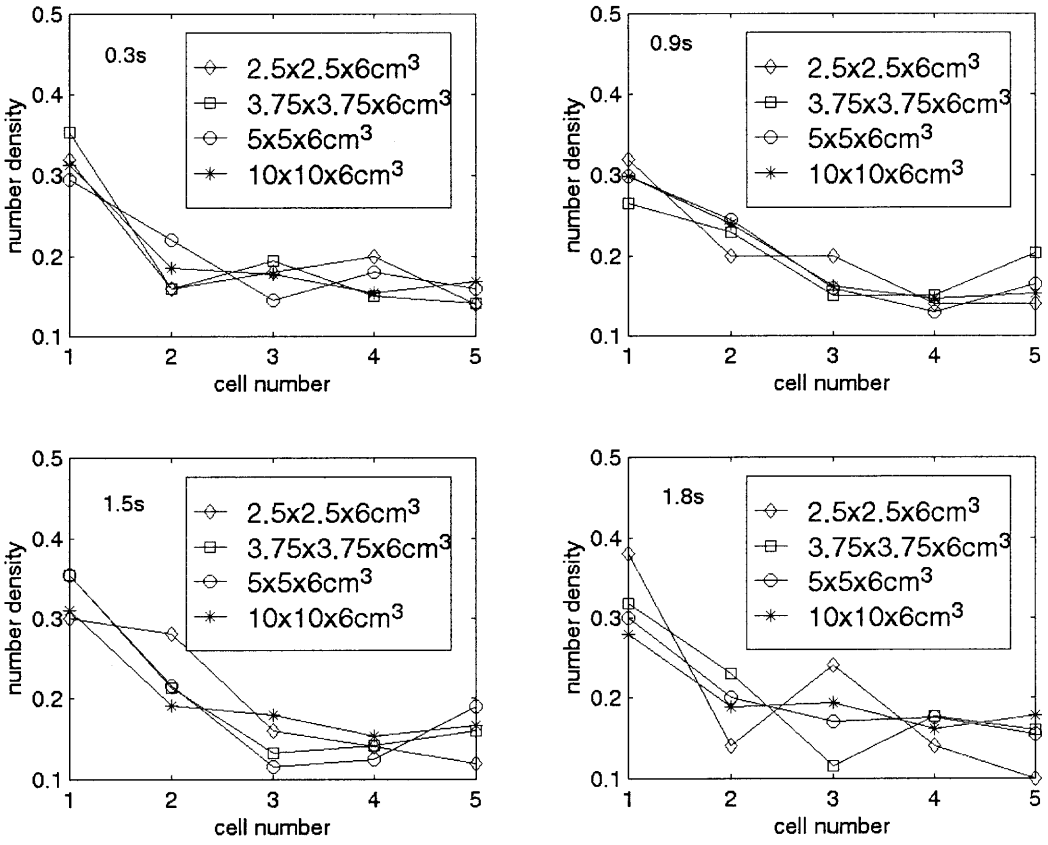


**Figure 4.12** The number densities of magnetic particles at different simulation volume at different time as t=0.3,0.9,1.5 and 1.8seconds.

### 4.3.4 The Effect of Frequency of Current

The current flowing through the solenoid is considered to be $I = I_0 \sin(2\pi f t)$. The effect of changing the frequency f of the current is tried to system of 50 magnets(1.6 gm) and within a simulation volume of 37.5 ml. $I_0$ is kept constant at 5 Amperes. The average translational velocities for the magnetic particles are calculated at different times as shown in Fig 4.14. At lower times the translational velocity fluctuates with the frequency of the current in accordance to the experimental results. In higher t the average translational velocity decrease with increase of frequency. But in almost all the cases the

velocity increase with time in a given frequency. In Figure 4.15 the variation of the average rotational velocity of magnetic particles is shown.

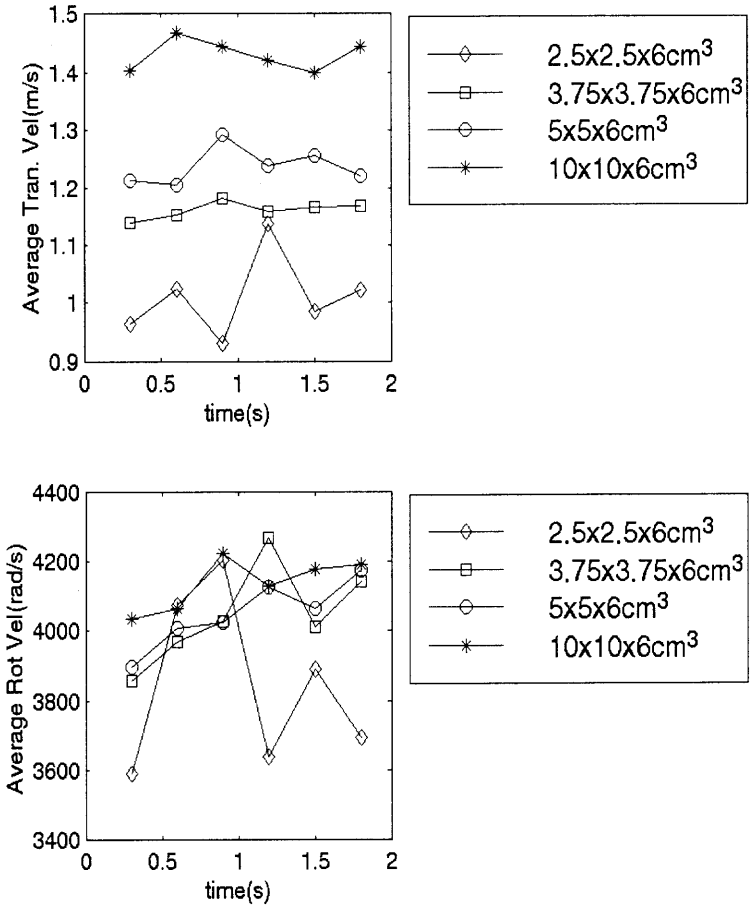


**Figure 4.13** The variation of translational and rotational velocities of magnets in different simulation volumes.

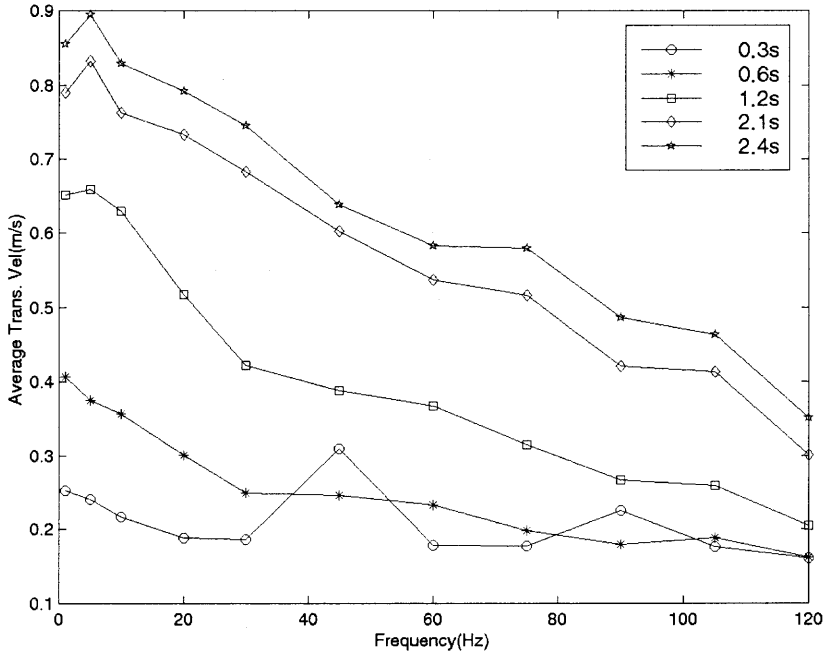


**Figure 4.14** The average rotational velocities of magnetic particle with frequency at different simulation volumes.

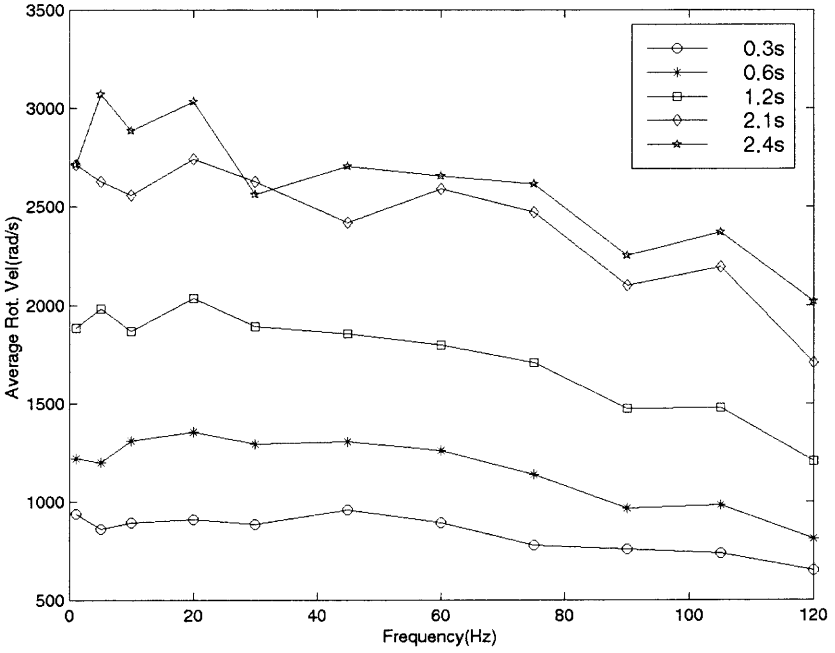


**Figure 4.15** The variation of average rotational velocity with frequency at different times.

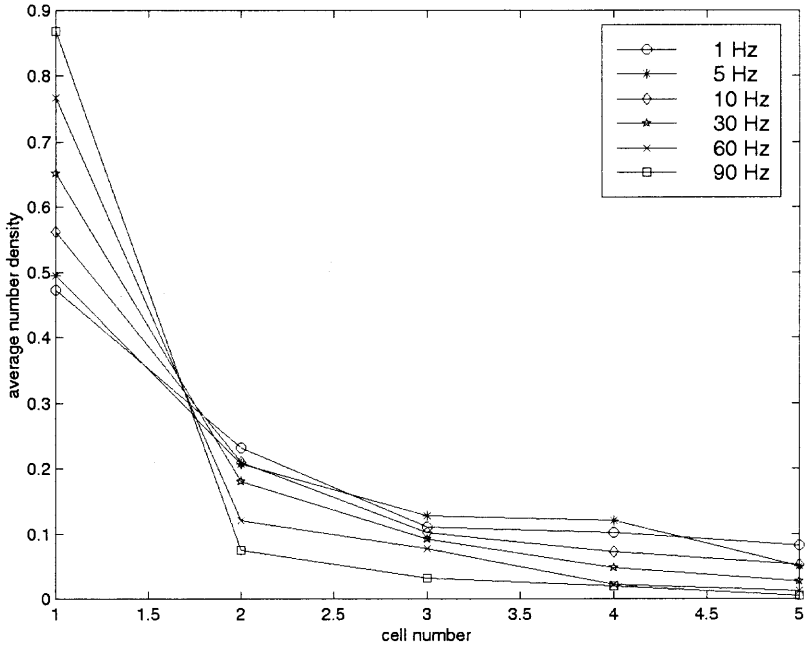


**Figure 4.16** The average number density of magnetic particles plotted against cell numbers.

The average rotational velocity is found to be non fluctuating initially. Later with time the velocity start fluctuating. In Figure 4.16 the average number density of the magnetic particles are plotted against the cell numbers. It is generally seen that with increase in frequency the fluidization is decreased.

### 4.3.5 Comparison of Velocities from Experiments and Simulation

The motion of the magnetic particle in MAIC play an important role to make the bed fluidized and let the system having enough collisions necessary for coating. High speed video camera is used to record the motion of magnets in MAIC at a rate of 500 frames per second. A glass bottle of radius 2.5 cm and height 6cm is filled with 1.6 gm of magnets. The external magnetic field is generated by a C-coil. The bottle is positioned horizontally and vertically above the C-coil. The C-coil is connected to the line voltage

(110 V, 60 HZ, 1.1 A) and the motion of the magnets is recorded by the video camera. The magnetic field due to C-coil in its vicinity is approximately 35 mT. Table 4.1 shows the results from the experiment where the bottle is kept vertical over the C-coil. In course of time rotational velocities of 6 of the particles are measured from the digital image of the frames. Figure 4.17 shows the first three frames of the recorded motion of magnetic particles and the way the rotational velocity is calculated. The rotational velocity of the magnet

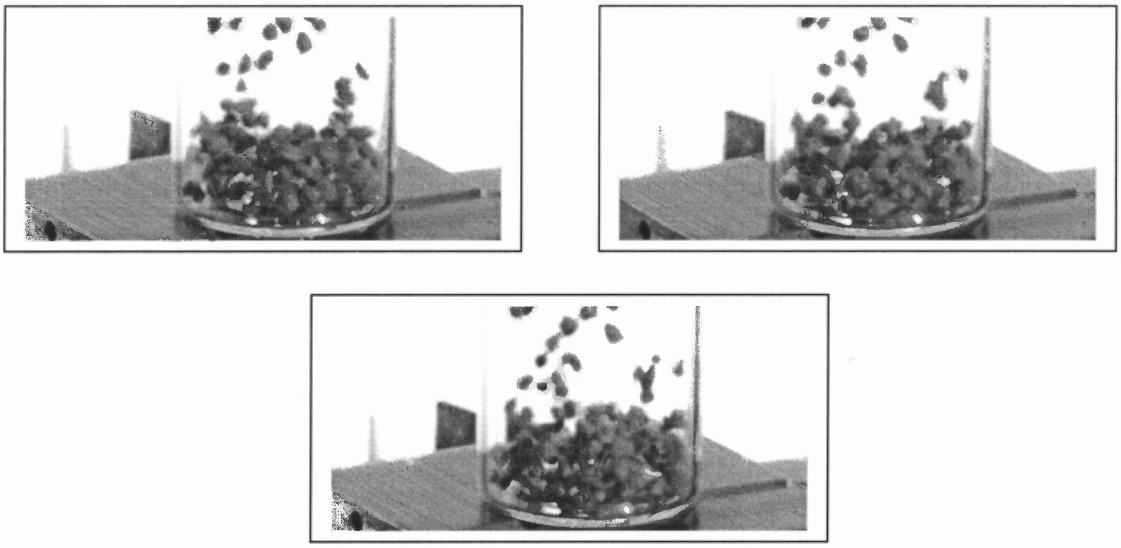

**Figure 4.17** The first, second and third frame of the recorded experiments.

nearest to the right wall of the bottle is calculated. That magnet if observed closely in seen to gone through 0.75 of cycle of rotation in following second and third frame.

**Table 4.1** Measurement of rotational velocities when bottle is vertical.

| Cycles | Frames | Frame number | Velocity(rad/s) |
|---|---|---|---|
| 0.75 | 2 | 1,2,3 | 1178 |
| 1 | 4 | 1,2,3,4,5 | 785 |
| 0.25 | 2 | 28,29,30 | 392 |
| 0.375 | 2 | 80,81,82 | 588 |
| 0.25 | 2 | 170,171,172 | 392 |
| 0.5 | 2 | 451,452,453 | 785 |

The average rotational velocity is calculated to be 686 rad/s. The translational velocities are also measured for this particular case and shown in table 4.2. Velocities are measured for 6 particles in this experiments. The tables 4.3 and 4.4 contains the estimation of velocities while the bottle is in horizontal position over the C-coil.

**Table 4.2** Measurement of translational velocities when bottle is vertical.

| Distance(cm) | Frames | Frame number | Velocity(cm/s) |
|---|---|---|---|
| 0.42 | 4 | 11,12,13,14,15 | 53 |
| 0.33 | 4 | 11,12,13,14,15 | 42 |
| 0.27 | 3 | 25,26,27,28 | 44 |
| 0.375 | 4 | 80,81,82,83,84 | 18 |
| 0.17 | 2 | 170,171,172 | 84 |
| 0.25 | 3 | 451,452,453,454 | 43 |

The average translational velocity of the cases above is 48 cm/s

**Table 4.3** Measurement of rotational velocities when bottle is horizontal.

| Cycles | Frames | Frame number | Velocity(rad/s) |
|---|---|---|---|
| 0.25 | 2 | 10,11,12 | 392 |
| 0.5 | 2 | 31,32,33 | 785 |
| 0.5 | 2 | 41,42,43 | 785 |
| 0.25 | 2 | 62,63,64 | 392 |
| 0.375 | 3 | 62,63,64 | 392 |

The average of the rotational velocities of the above calculations is 550 rad/s.

**Table 4.4** Measurement of translational velocities when bottle is horizontal.

| Distance(cm) | Frames | Frame number | Velocity(cm/s) |
|---|---|---|---|
| 0.32 | 3 | 50,51,52,53,54 | 53 |
| 0.4 | 3 | 50,51,52,53 | 67 |
| 0.32 | 3 | 31,32,33,34 | 53 |
| 0.4 | 3 | 31,32,33,34 | 67 |
| 0.2 | 2 | 41,42,43 | 50 |

The average velocity of the five cases is 58 cm/s.

The numerical model is then tried to estimate the translational and rotational velocities. with similar parameters in the experiments in the Figure 4.18 shows the

average translational and rotational velocities at different current and time. The results corresponding the 5 Amps

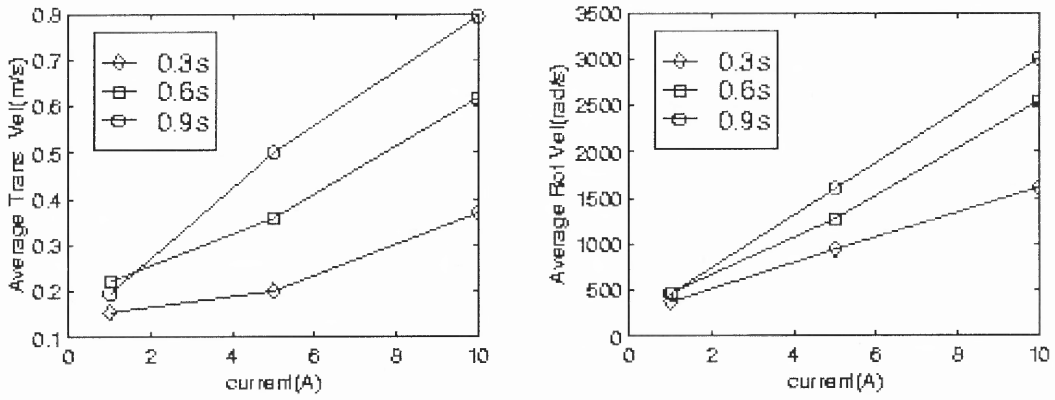


**Figure 4.18** The variation of velocities of magnet as function of current in the coil.

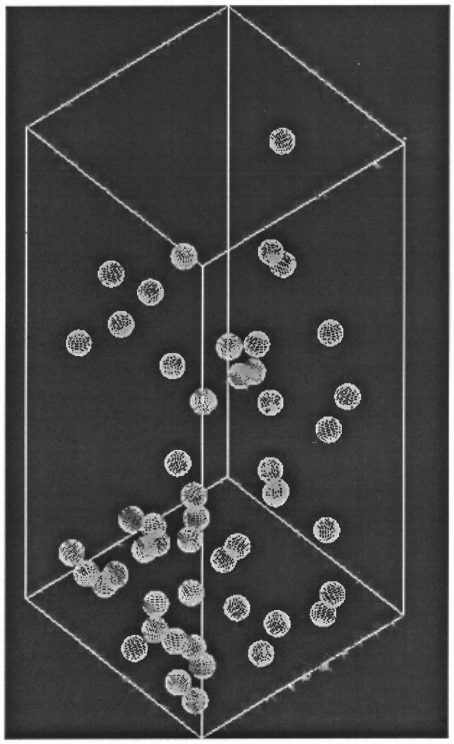

**Figure 4.19** A snapshot of magnets being fluidized in the simulation box.

is corresponding to the experimental one (with 35 mT external field). The average rotational and translational velocity from the three points (corresponding to t = 0.3, 0.6, 0.9s ) is approximately 1200 rad/s. and 40 cm/s respectively against 686 rad/s and 48cm/s of the experimental averages.

The dipole moment of the magnetic particles used in this modeling is 0.26 emu. If the magnetic dipole moment of the particles are considered to be 0.52 emu (as measured in experiments) the fluidization of the particles appear very lately and the velocity profiles of the magnetic particles also become close to experimental values. In figure 4.20 the average translational and rotational velocities are plotted, where the averages are approximately 18 cm/s and 500 rad/s. The positions and the orientations of the particles are used to generate an animation of particle dynamics in the simulation volume. Figure 4.19 shows the snapshot of the animation where the magnets are in a fluidized state. OpenGL [38] and X/Motif programming[39] is used to generate the animation of the movement of the magnets and also the case of magnets with PMMA.

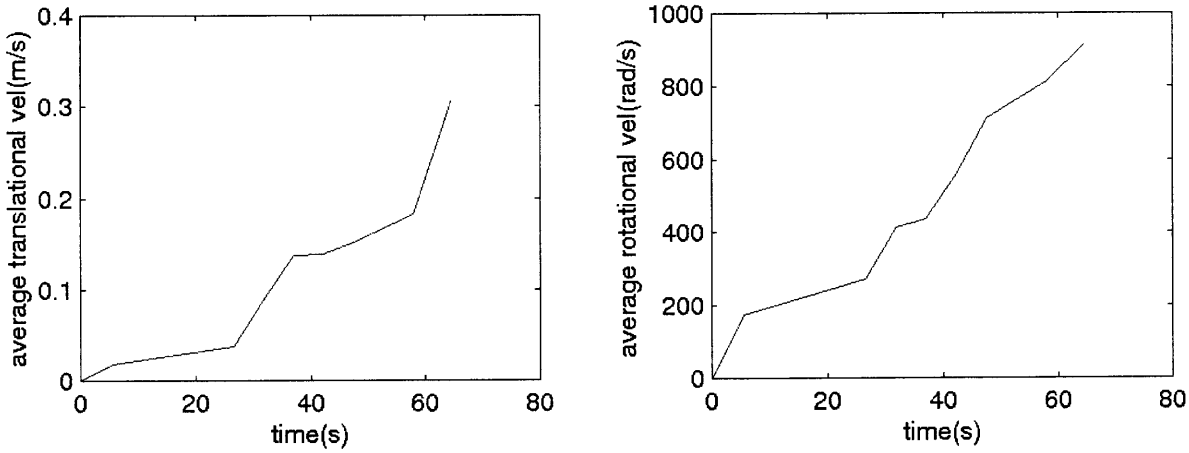


**Figure 4.20** The average translational and rotational velocities with time.

## 4.4 Host Scale Modeling

The host scale modeling is actually started in section 4.3.2 as the DEM of magnets and non-magnets are tried. The average velocities for the two component system (magnets & non-magnets or hosts) are also estimated till t = 1.4s ( as it goes beyond 0.9s result presented in section 4.3.2 ). In figure 4.21 the variation of average rotational and translational velocities with time is shown for magnets and PMMA particles. PMMA has the same size of 200 micron where the magnets are of diameter 2.36mm. Here the magnetic particles are found to be moving slower than the case where they were alone. The PMMA particles being smaller and lighter are moving with higher rotational and translational velocities. The average translational velocity for the PMMA particles are almost twice that of the magnetic particles. Whereas the PMMA particles are rotating in an average velocity which is one order higher than that of the magnets. Moreover, the average number densities of the magnets and PMMA are plotted against the cell number. Results are in the same fashion with figure 4.6(a) and 4.6(b) where the number densities till 0.9 s were shown. Here the PMMA particles are found to be more fluidized being agitated by the movement of magnetic particles.

The instantaneous translational and rotational velocity distribution of the magnets and PMMA particles at t=0.7s is shown in Figure 4.22, 4.23, 4.24, 4.25 and 4.26. In Figure 4.22 the frequency distribution of translational velocities of 50 magnets is plotted. The average velocity in that time is approximately 0.22 m/s, though some particles are moving faster at 1 m/s.

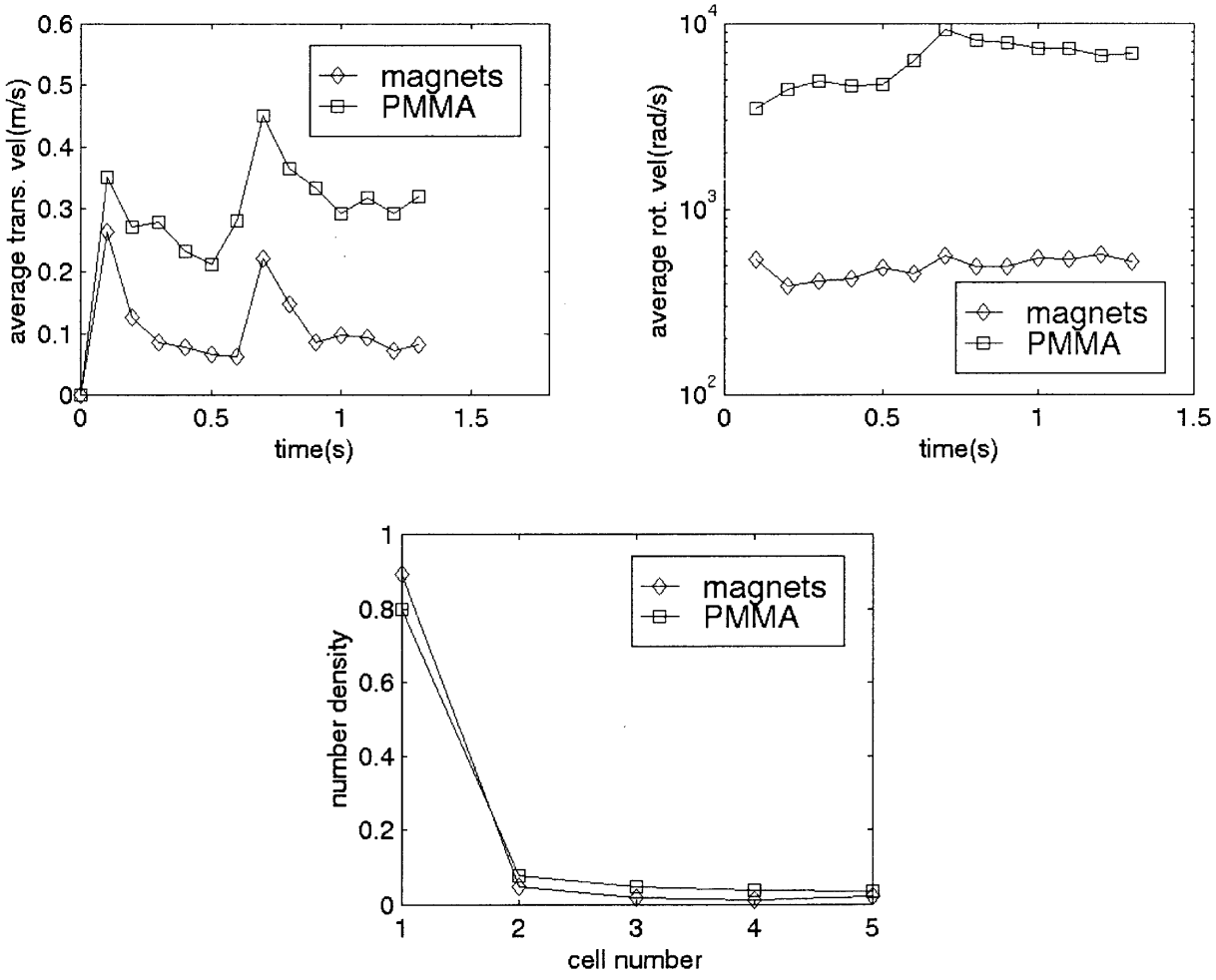


**Figure 4.21** The average rotational and translational velocities are plotted against time. The figure at the bottom shows the variation of average number density with the cell number.

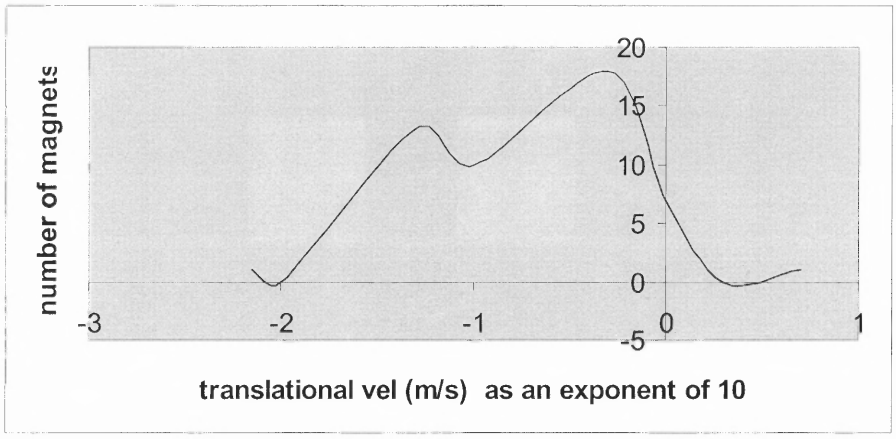


**Figure 4.22** The translational velocity(m/s) distribution of magnets.

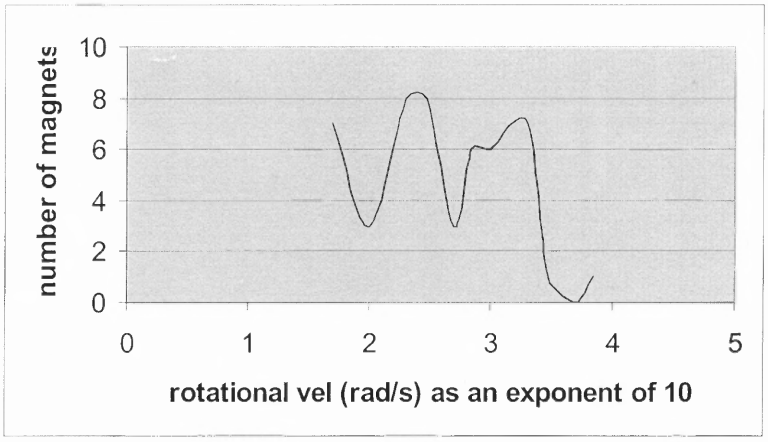


**Figure 4.23** The rotational velocity(rad/s) distribution of magnets.

The rotational velocity distribution for the magnets is shown in Figure 4.23. The average velocity is approximately 561 rad/s and the maximum velocity attained by some magnetic particles are close to 6000 rad/s. In Figure 4.24 the cumulative translational velocity of

PMMA is shown. The average translational velocity is calculated to be 0.45 m/s which is higher than the same of magnetic particles. In this typical magnet-host simulation the guest particles are not being considered because nanometer sized guest particles(alumina of 200nm diameter) make the timestep of simulation 3 order less than what is tried here. But the virtual presence of the guest particles are considered within the system to investigate the effect of host-guest virtual collisions with the velocities attained by the host(PMMA) itself in this simulation. This assumption is only valid if the guest particles are stagnant and the drag due to the particles is nominal and thus cant affect the host velocities. According to Rogers. et al. [10] the minimum velocity the guest needs to possess while impacting and causing any plastic deformation to the host is dependent on the mechanical and physical properties of the particles( equation 1 in chapter 3), which is $1.14 \times 10^{-3}$ m/s. velocities. In the figure 4.24 the relative velocities(between a host and a guest particle) necessary to make plastic deformation on the host surface is also shown. The minimum and the higher velocities necessary to make different depth of deformation in taken from the depth of deformation curve in Figure 3.2 which are shown as vertical lines in figure 4.24. Almost all the host particles are moving with a higher velocity than the minimum relative velocity necessary for plastic deformation. It is assumed that there is no external normal load applied to the particles.15% of the PMMA particles are possessing a velocity higher than 1m/s which is adequate to make 1nm depth of deformation on its own surface by 100 nm guest particles. This depth of deformation is only 1% of the radius of the guest and so the velocity achieved by the simulation is not high enough. The increase in external magnetic field or the magnetic dipole moment of the magnetic particle can make the PMMA particles moving in desired velocities (as high

as 100 m/s). In Figure 4.25 the translational velocity (rad/s) distribution of PMMA particles is shown. Almost 100 PMMA particles attain the translational velocity 10m/s which can result 5nm of plastic deformation after colliding with guest particle.

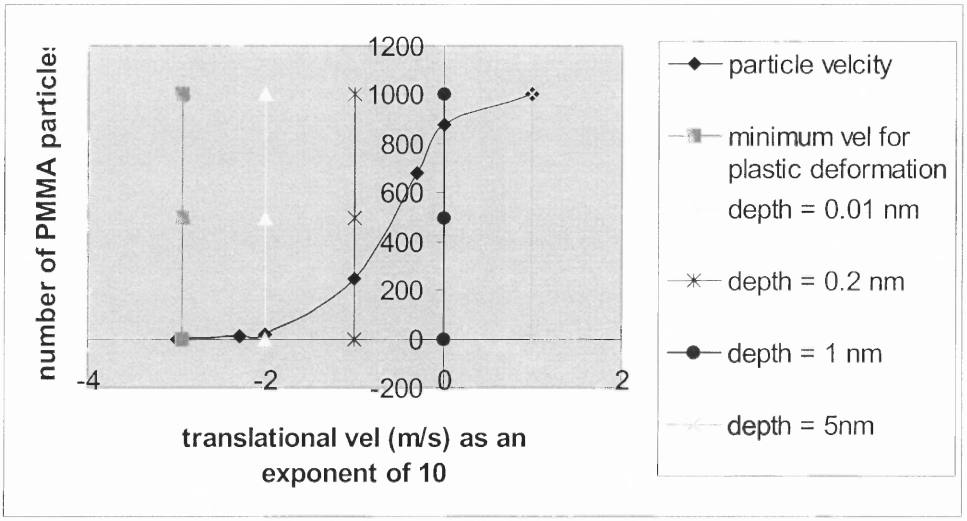


**Figure 4.24** The cumulative translational velocity distribution of PMMA particles.

The rotational velocity of the PMMA particles are plotted in figure 4.26.The average velocity is 9331 rad/s while some particles attain higher velocities close to $10^6$ rad/s. As an after effect of random collisions the PMMA particles being smaller and lighter than the magnets are found to be moving with higher velocities than the magnets.

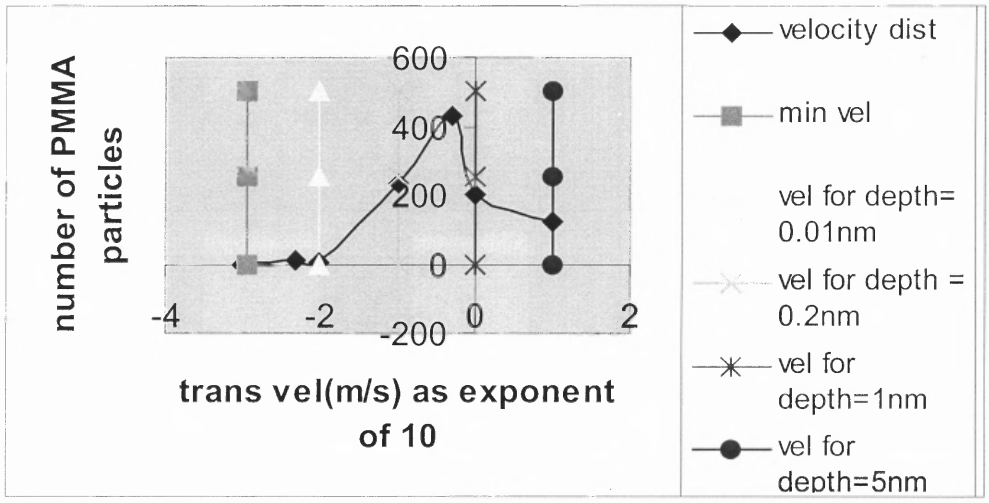


**Figure 4.25** The translational velocity distribution of PMMA particles.

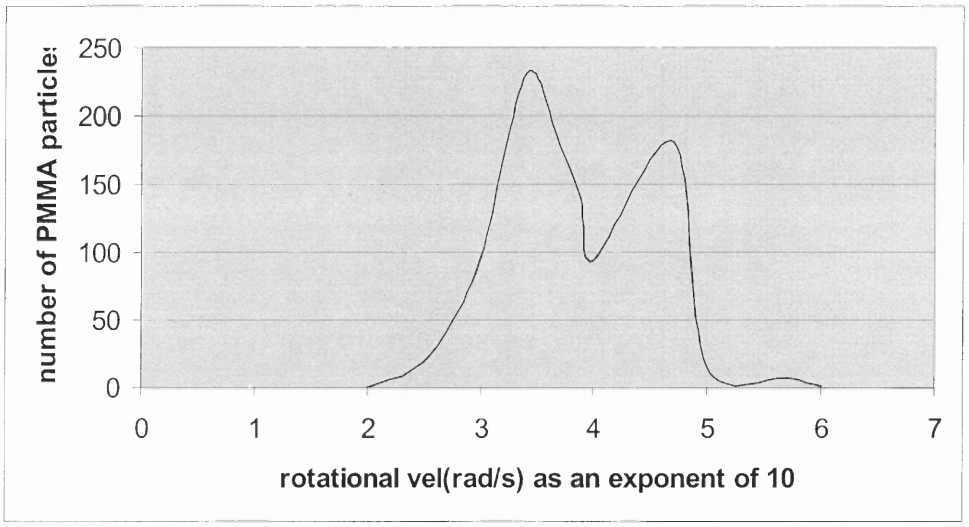


**Figure 4.26** The rotational velocity distribution of PMMA.

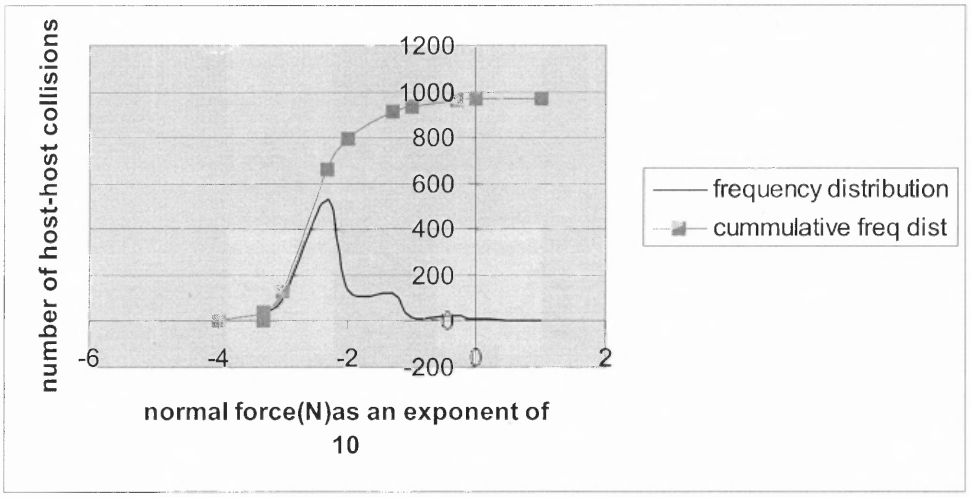


**Figure 4.27** The Cumulative and Freq. Dist. of normal force(N) of particle in contact in 968 collisions.

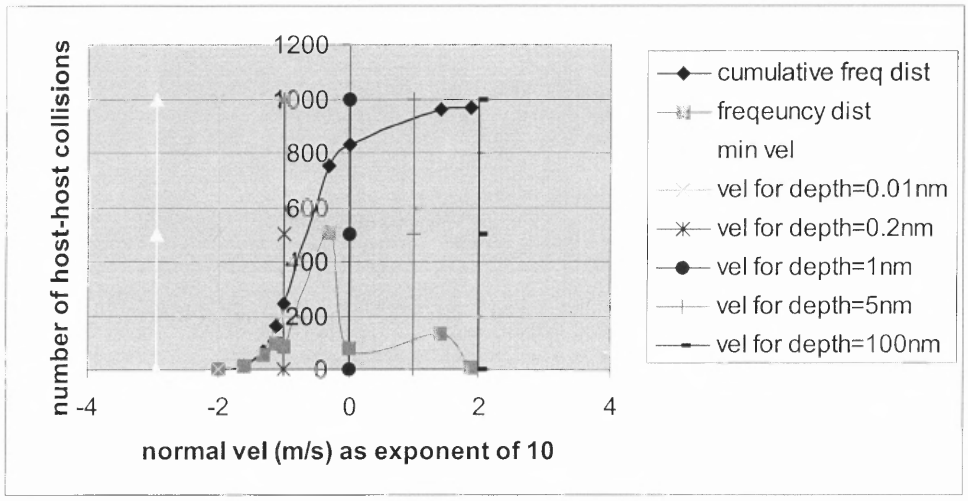


**Figure 4.28** The cumulative and frequency distribution of normal velocity (m/s) distribution for 968 collisions.

### 4.4.1 Estimation of Coating Time and Other Results

In order to investigate the effect of the velocities achieved in the system on the particle collision and the idealized coating time a similar two component (magnet +PMMA) simulation is run for 0.1s after the particles are deposited from a random distribution within the simulation space. In the time span of 0.1 s there are 17,887 of particle-particle and particle-wall collisions, out of which 2769 collisions are between particles. 968 collisions are between hosts. In MAIC coating mechanism, it is postulated that the coating takes place primarily as guest comes in contact with a host and then the same host collide with another host to get the guest embedded onto its surface. In this case it is assumed that the guest particles are sticking to the host surface when the host particles are in random collisions. Figure 4.27 illustrates the cumulative maximum normal force(during a collision) distribution between pairs of host particles in collisions. The normal force can be used in the Hertz's Law to evaluate the area of contact of the colliding particles(equation 42).

$$a^3 = \frac{3}{8}\left(\frac{1-\gamma^2}{E}\right)F_n D \qquad (42)$$

where a is the radius of contact, $F_n$ is the normal force, D is the diameter, $\gamma$ is the Poisson's Ratio and E is the Elastic modulus of the particle.

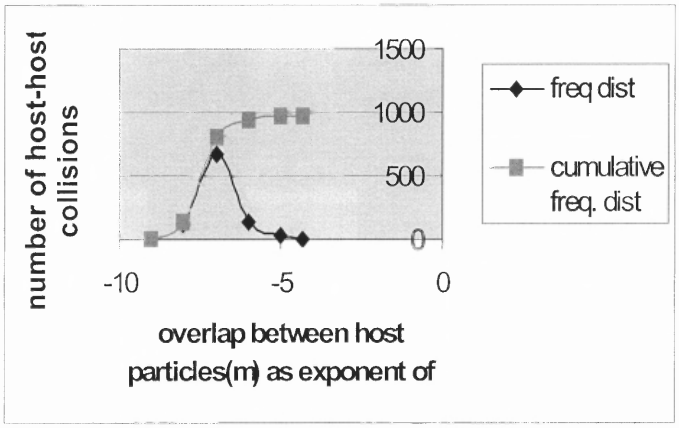


**Figure 4.29** The host-host overlap distribution in 968 collisions.

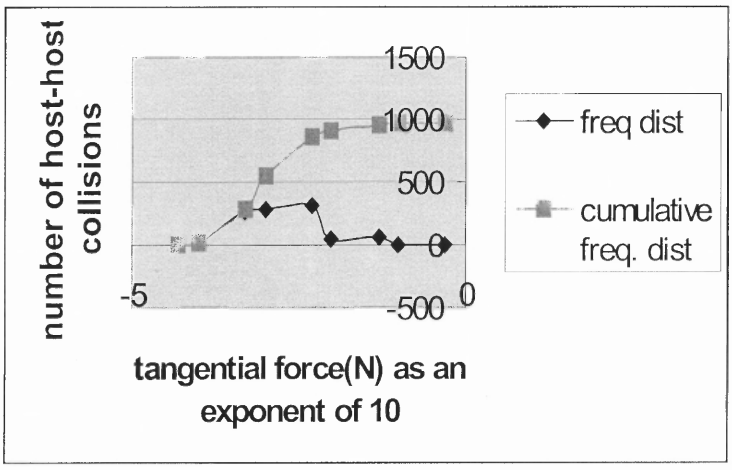


**Figure 4.30** The tangential force(N) distribution in 968 host-host collisions.

The total area of contact calculated for 968 collisions is $1.288 \times 10^{-7}$ $m^2$. The total surface area of 1000 PMMA (host) particles is $1000 \times 4 \times \pi \times (100 \times 10^{-6})^3 = 1.256 \times 10^{-4}$ $m^2$. As these 968 host-host collisions take place in 0.1 s , the total time need to cover the whole host surface area should be approximately 97.5 seconds.

The maximum normal velocity during the host-host collisions is also estimated and shown in Figure 4.28 as a cumulative distribution. The minimum velocity necessary to create a plastic deformation when one alumina (guest particle) of 200 nm is impacting on a PMMA sphere surface of 200 micron size is $1.14 \times 10^{-3}$ m/s [Rogers et al.]. In figure 4.28, most of the host particles are seen to achieve that normal velocity during the collisions. Almost 200 particles are having more than the velocity to create depth of deformation of 1nm. This is true if there is no external normal load acting between particles. The frequency distribution of the maximum overlap of the host particles during the collision is shown in figure 4.29. The average of maximum overlap is about 0.2 micron which is nominal to the host particle radius but equal to the diameter of the guest particle present in MAIC system and can be considered existing on the surface of the host particle. In very few collisions the overlap is as big as 10 micron. In figure 4.30 the frequency distribution of maximum tangential force is shown. It is seen that the tangential force is generally less than the normal force in the particle collisions. The average of the tangential force is about 4 mN.

Let us consider that guest particles(100nm diameter) are sitting on the host surface as hosts are colliding and the same normal force which the two hosts experienced in contact is also felt by the guest particle. Then guest particles can be considered impacting host particle at the velocities shown in figure 4.28.If the algorithm of Rogers et

al. is again employed to calculate the depth and radius of deformation on the host surface by the guest particle. The frequency distribution of depth of deformation is made in figure 4.31. The depth of deformation on the host surface can be considered as the part of embedded guest particle. More than 6% of the host particles have 10nm of guest embedded on their surface whereas 35% of host particles have 10nm or more of radius of plastic deformation. The frequency distribution of radius of deformation is shown in figure 4.32. So with the consideration of normal force in Rogers[10] model the amount of guest getting embedded to the host obviously increase.

As the guest particle sitting on the host surface is considered experiencing the same normal force between two colliding hosts, the existing contact mechanics theories (which are generally applicable for micron size or bigger particles) are helpful to find out the contact radius and the overlap between the host and the guest. The van der Waals attraction force generated due to the contact is responsible to keep the particles together. This attraction force is then compared with the force of separation suggested by different theories necessary to snatch the guest particle from the host surface.

The DMT theory[7] calculates the radius of contact using the same Hertz equation (42). The contact radius is shown in a frequency distribution plot in figure 4.33. Most of the guest particles are having a contact radius more than their own radius. It shows the force achieved in the model is adequate to make the contact radius atleast equal to the radius of the guest particle. The applicability of this theory for nano particles is under investigation by other research groups. The overlap between a spherical particle and a surface(of host particle) under external load

$$\alpha = \frac{3\pi\theta F_n}{4a} \qquad (43)$$

where $\alpha$ is the overlap, $F_n$ is the external load, a is the contact radius and $\theta$ is defined as $\left(1-\sigma^2\right)/\pi E$ . $\sigma$ and E are the Poisson's ratio and Young modulus of the spherical particle. The contact radius (calculated from equation 42) and the normal force is used in equation 43, to estimate the overlap between the guest particle and the host particle. Figure 4.34 shows the frequency distribution of the overlap between guest and host particle. The overlap is found to be one order more than the depth of plastic deformation shown in figure 4.31. Here also most of the guest particles have their overlap with the host more than it's own radius.

The popular JKR theory[6] provides the contact radius in an elastic contact between the guest and host surface in the following equation

$$a^3 = \frac{R}{K}\left\{P + 3w_A\pi R + \left[6w_A\pi RP + \left(3w_A\pi R\right)^2\right]^{0.5}\right\} \qquad (44)$$

$w_A$ is the work of adhesion for alumina and PMMA which is equal to 519.5 $mJ/m^2$ and K is used as calculated in chapter 3. The frequency distribution of the contact radius is calculated using eqaution 44 for all host-host collisions and plotted in figure 4.35. In this is figure it is seen the contact radius of most of the particles are even bigger than the same estimated from DMT theory. The contact radius in this case is always more than the radius of the guest particle. The normal force is so high that the guest particles are more than 100% elastically deformed.

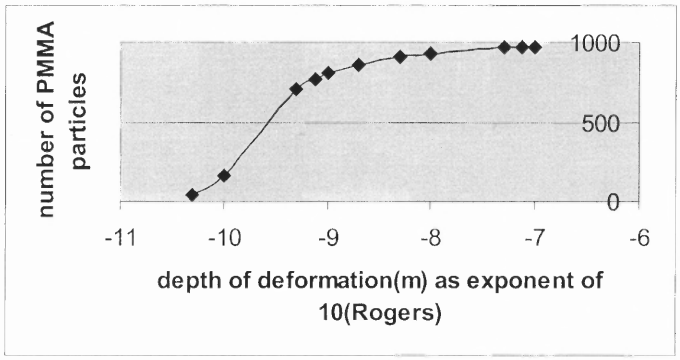


**Figure 4.31** The frequency distribution of depth of deformation(m) on PMMA particles.

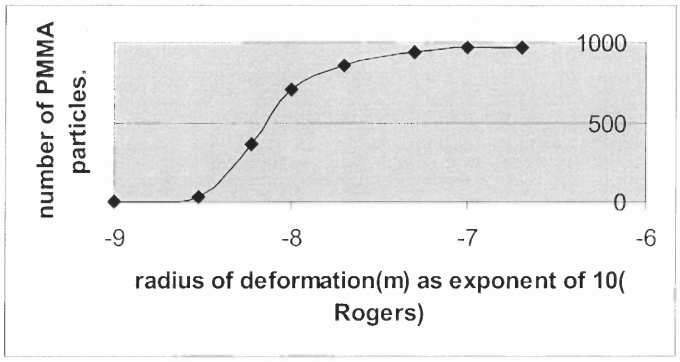


**Figure 4.32** The frequency distribution of radius of deformation(m) on PMMA particles.

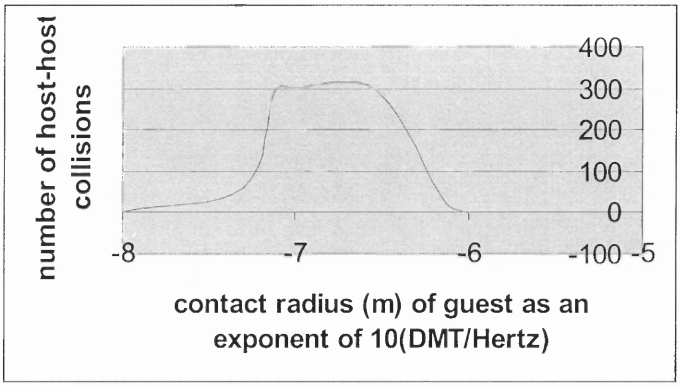


**Figure 4.33** The frequency distribution of contact radius(m) between guest and host particle.

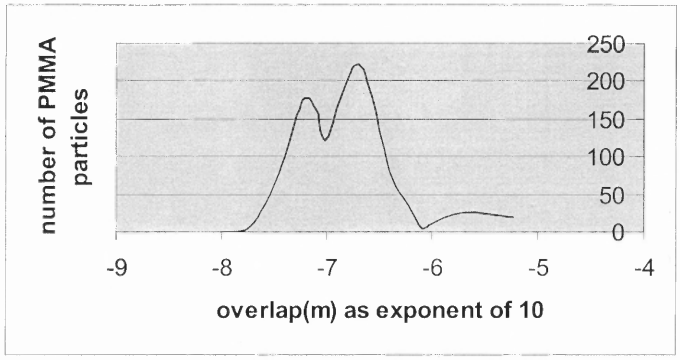


**Figure 4.34** The frequency distribution of overlap(m) (from DMT theory) between host(PMMA) and guest(Alumina).

The Maugis and Pollock theory[25] is an elastic-plastic theory and the radius of contact is given by:

$$a = \left( \frac{F_n + 2\pi w_A R}{3\pi Y} \right)^{0.5} \tag{45}$$

where Y is the yield stress of the alumina particle which is $7 \times 10^7$ Pa.

The frequency distribution of the contact radius calculated from equation 46 is shown in figure 4.36. The radius calculated here are more than that calculated from JKR and DMT theories. This shows the guest particles are all getting more than 100% plastic deformation in all of the host-host collisions.

After the guest and particle are coming in contact the attraction force which keeps them together is van der Waals force. The typical van der Waals force(without deformation) for the alumina guest particle of 200nm and PMMA guest particle of 200 μm is also estimated in the following steps.

Van der Waals force between two spheres of different material and radii is

$$F = \frac{A_{12} R_1 R_2}{6D^2 (R_1 + R_2)} \tag{46}$$

where $A_{12}$ is the Hamaker's Constant for two component system and D is the separation distance considered to be 4 Armstrong generally (Israelachvili [23] considered it to be 1.56 Amstrong) for surface imperfections. In this case $R_1$ and $R_2$ are 100nm and 100 μm respectively. $A_{12}$ in this case is $1.087 \times 10^{-19}$ J (calculated below) and the van der waal force from equation 46 is $1.13 \times 10^{-8}$ N ( if D = 4 Amstrong) and $6.65 \times 10^{-8}$ N (if D = 1.65 Amstrong). So the normal force generated in the host –host collision is of much higher order than the van der waals force between the guest and the host particle.

$$A_{12} = \sqrt{A_{PMMA} \times A_{alumina}}$$

$$= \sqrt{8.442 \times 10^{-20} \times 14 \times 10^{-20}}$$

$$= 1.087 \times 10^{-19} \text{ Joule}$$

The van der waal force due to deformation between the guest and host particle is a function of contact radius caused by deformation and is given by:

$$F_{def} = \frac{A_{12} \rho^2}{6z^3} \tag{47}$$

where $\rho$ is the radius of the contacting surface. The contact radius calculated earlier from DMT, JKR and MP theories is used in equation 47 to calculate the van der waals force of

attraction. In figures 4.37, 4.38, 4.39 and 4.40 that frequency distribution of the van der waals force is shown and they are calculated from DMT, JKR, MP and Roger's theories respectively. The radius of plastic deformation obtained from Rogers theory is found to be the most realistic one where the radius of deformation is always less than the radius of the guest particle.

The separation force $P_S$ which is necessary to tear of the guest from the host surface is dependent on the work of adhesion and the radius of the guest particle. As proposed by DMT the separation force $P_S = 2\pi\omega_A R$ and by JKR the same sort of force equals to $1.5\ \pi\omega_A R$. The separation force from DMT theory is shown in figure 4.37 along with the van der waals attraction force calculated using the radius calculated from DMT theory. It is seen that almost for all the guest particles the force of attraction is much more than the force of separation. But some particles are so loosely bound that could be torn off from the surface. In figure 4.38 the force of attraction for all the guest particles are more than the force of separation and so no guest particle can be snatched from the host surface. The separation force and the attraction are calculated using JKR theory. In figure 4.39 the force of attraction is calculated using MP theory for all the guest particles. The separation force opined by the JKR and DMT happened to be much less than the attraction force calculated. In figure 4.40 the van der Waals attraction force for the radius of plastic deformation calculated from Rogers is shown in frequency distribution plot. The separation force calculated from the DMT/JKR theory is seen to be more than the attraction force most of the hosts experiencing. 15% of the host particles will remain adhered with the guest particle as the separation force can not tear them apart.

The normal velocities and forces achieved by the hosts in the simulation are adequate to create sufficient embodiment of the guest particles onto the host particle surface.

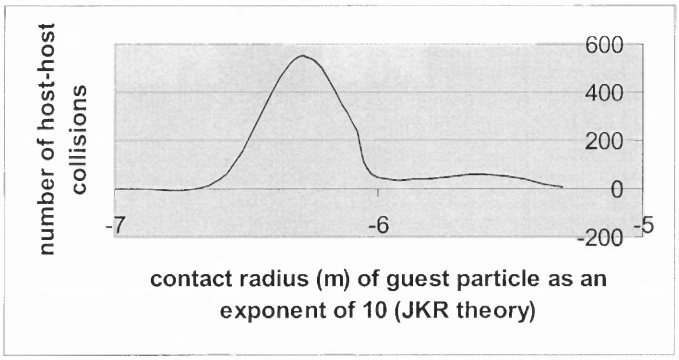


**Figure 4.35** The frequency distribution of contact radius between guest and host(JKR).

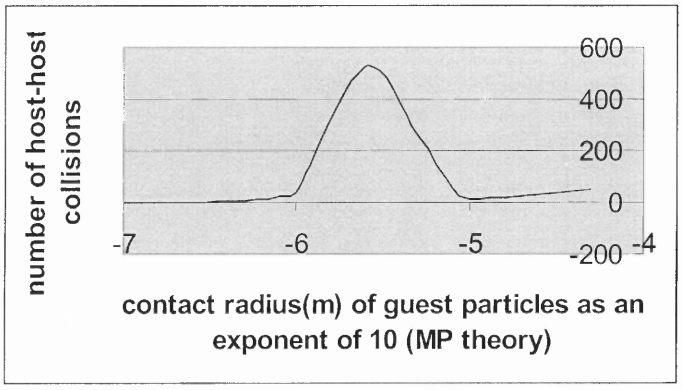


**Figure 4.36** The frequency distribution of contact radius between guest and host(MP).

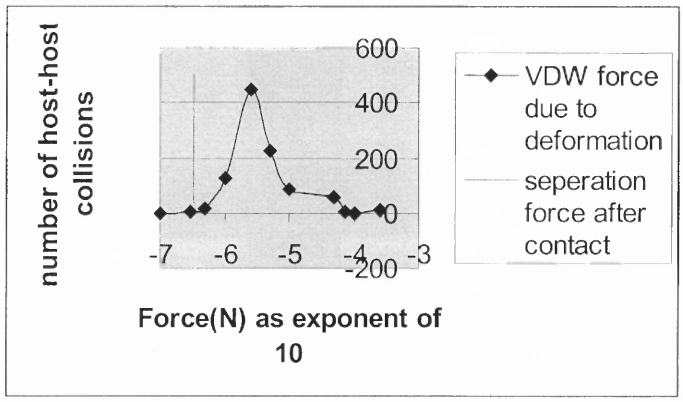


**Figure 4.37** The frequency distribution of the van der waals force between guest and host(DMT).

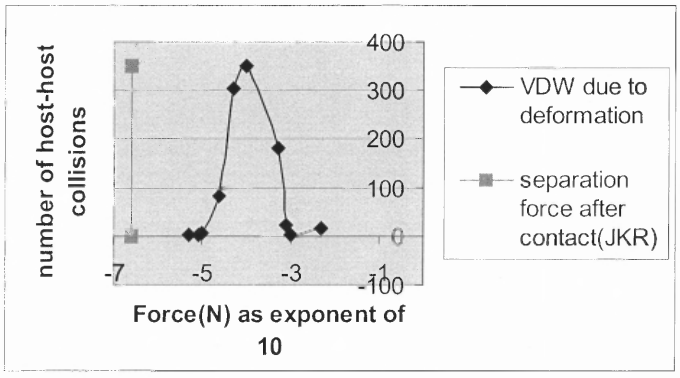


**Figure 4.38** The frequency distribution of the van der waals force between guest and host(JKR).

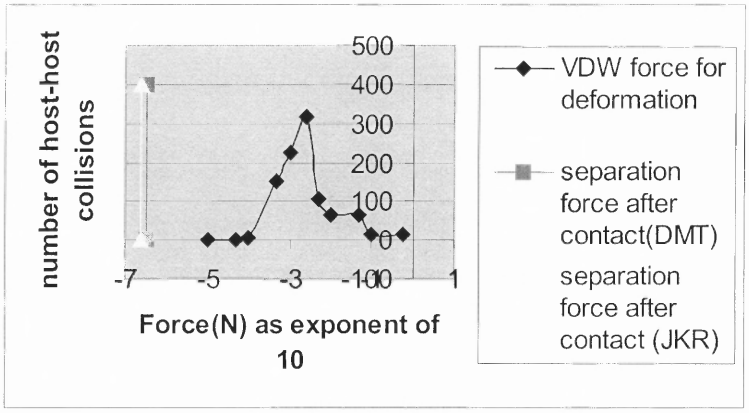


**Figure 4.39** The frequency distribution of the van der waals force between guest and host(MP).

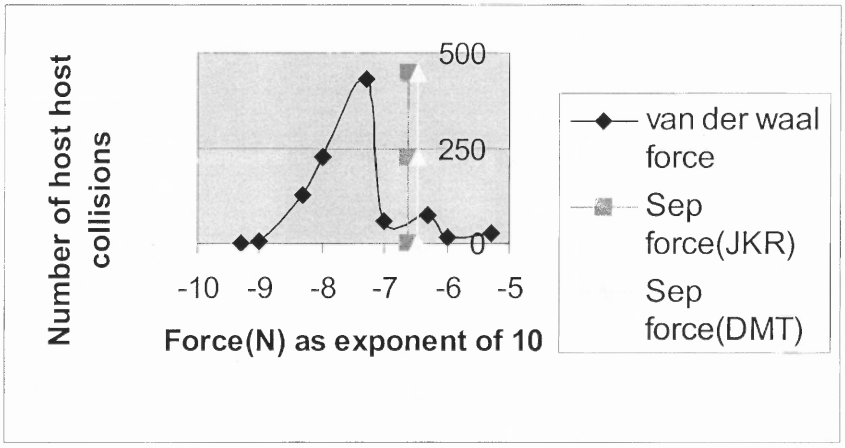


**Figure 4.40** The frequency distribution of the van der Waals force between guest and host(Rogers).

The effect of number of magnetic particles in the coating process is also investigated.

In the same system of PMMA/magnets the number of magnets is varied while keeping the number of PMMA particles same as 1000. The number of magnets is varied as 10,50 and 80 and the number of collisions between the magnets and the hosts, between hosts and host and wall is estimated. Initially the number of collisions increase with number of magnets for all cases which is in favor of increase of coating surface ( as observed in experiments). But as the number of magnets become more than 50 the magnets become inappropriately large as compared with 1000 PMMA particles and the number of host-host and wall-host collisions decrease. But the magnet-host collisions increase with the number of magnets

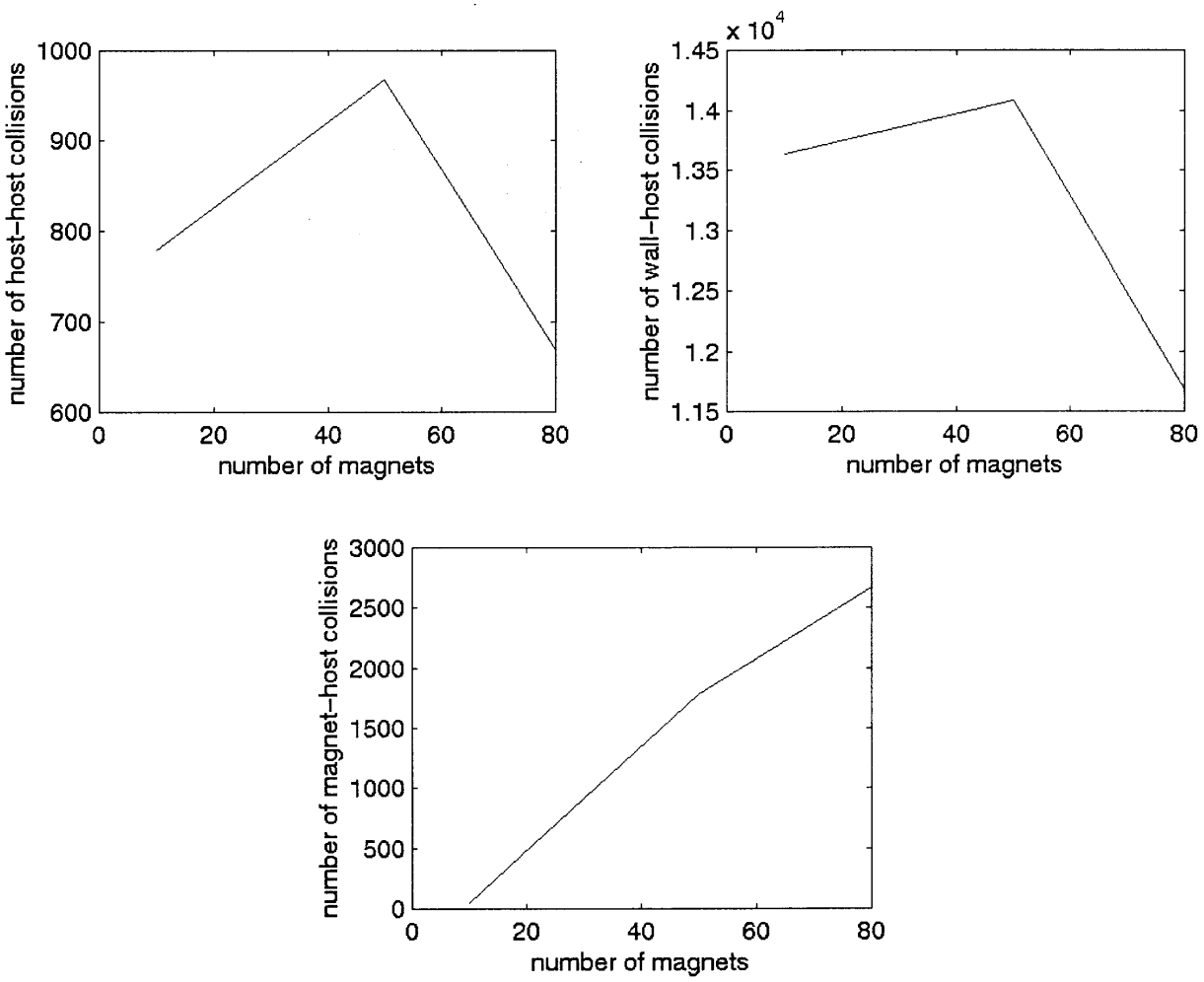


**Figure 4.41** The variation of number of collisions with the number of magnets in the system.

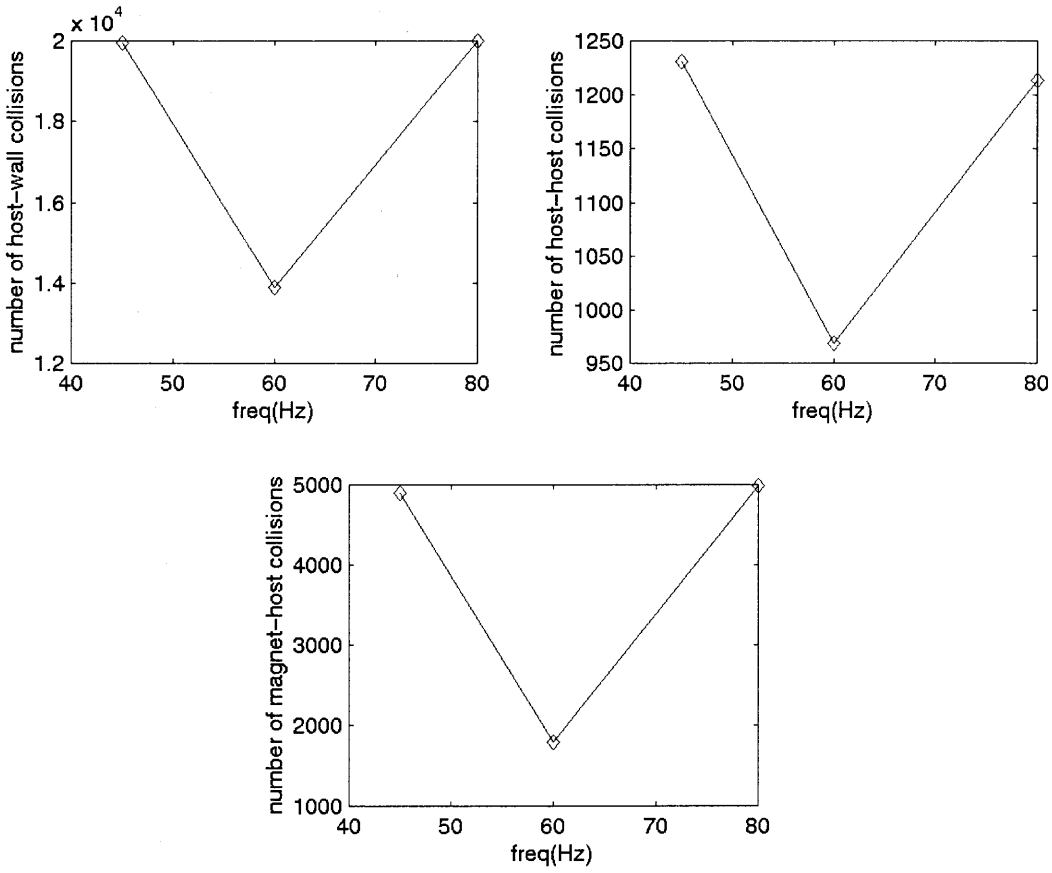


**Figure 4.42** The variation of number of collisions with the change of frequency of the current.

The effect of the frequency of the current on the number of collisions( where the host is involved) is checked. At the frequency of 60 Hz the number of collisions remains low. It's experimentally observed that around the frequency of 60 Hz the surface coating is less. As we consider the number of collision play the major role in coating the surface, the modeling result qualitatively show the same trend of experimental findings.

### 4.4.2 The Estimation of Coating Quality

Alonso Gamez [41] has formulated the coating quality(Q) as function of host-host collision. As in our numerical model we have already calculated the collision frequency of the hosts the estimation of coating quality was one interesting experiment to be tried. He developed a discrete population balance based model assuming (1) both hosts and guests are perfect spheres (2) the guest do not form agglomerate (3) all the host-host collisions are binary (4) in each collision only one guest can be transferred to a host surface. (5) a host complete coated with monolayer of guest cant accept any more guests particle (6) all the guest are attached to the host at all the time (7) all the hosts are randomly mixed within the bulk of the powder. Some of the assumptions mentioned don't match with the MAIC system.

Alonso Gamez considered the number of sites on each host surface available for guests would be denoted by N and, which must be lying in the interval

$$N_{rnd} < N < N_{hex}$$

Where, $N_{hex}$ and $N_{rnd.}$ are the number of sites for hexagonal packing of guests on host and the same for random packing of guest on host-surface respectively.

$$\text{where } \mathbf{N_{hex}} = \frac{2\pi}{\sqrt{3}}\left(\frac{\mathbf{D}}{\mathbf{d}}+1\right)^2 \tag{48}$$

$$\text{And } N_{rnd} = N_{hex} / \lambda^2 \quad \text{where } 1 < \lambda < 4/3 \tag{49}$$

Where d and D are the diameter of the host and guest particles.

$P_t$ is the transfer probability of the guest in a guest-host contact in a host-host collision

and $\gamma_t$ is the number of host-host collisions in time t. In time t the coating quality is formulated by the following expression:

$$Q = 1 - e^{\frac{-2P_t\gamma_t t}{N}} \tag{50}$$

In this case $N_{hex}$ = 3634858 and $N_{rnd.}$= 2044607. N is considered to be the average of $N_{hex}$ and $N_{rnd}$ and equals to 2839733. The variation of $\gamma_t$ in this simulation is shown in figure 4.43. The number of host-host collsions increase with the time. The total number of collisions for t =0.1 s is 968. The coating quality as evaluated from equation 50 is plotted in figure 4.44. The transfer probability increases with time as number of collision increases The quality also increases with the transfer probability. The overall coating quality is very poor here as the number of collisions are not enough and the simulation is only for 0.1s duration.

## 4.5 Conclusions and Future Work

The device scale numerical model is developed with some basic assumptions. The model predicts good qualitative agreement of fluidization of the powder system and also the tremendous rotation movement of the magnets to work as an agitator. The predictions of rotational and translational velocities of magnets are 1200 rad/s and 40cm/s respectively while the corresponding experimental results are 686rad/s and 48cm/s. Two component systems are also modeled along with an estimation of coating time of host particles and coating quality considering the guest particles exist on the host surface. The contact area of host collision is estimated from the normal force of collision. The van der waals force is calculated from the area to find out the binding energy of host and guest. The

separation force is found to be less than the binding force. The effect of the size of the magnet and the frequency of the current on surface coverage is investigated and qualitatively compared with the experimental results.

In this dissertation a very simple numerical model of host and magnetic particle motion is developed. This model can be used to generate extensive data for collision frequencies of different types of particles, the information of normal forces and the normal velocities involved in each of the collisions under various operating conditions. These need to be utilized in developing a coating model that can predict the coating time and coating quality. More research might be done in the following areas mentioned below.

(a) In device and particle scale modeling the external magnetic field can be considered space and time variant.

(b) In particle scale modeling bigger guest particles can be considered in a 3 component system to model the coating process.

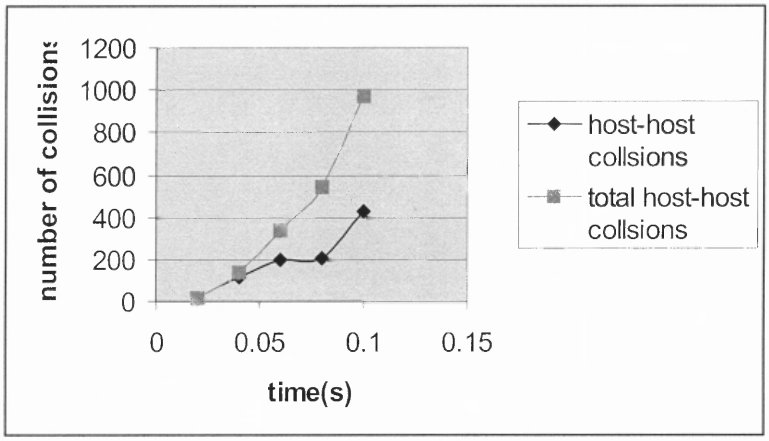


**Figure 4.43** The variation of the number of host-host collisions with time.

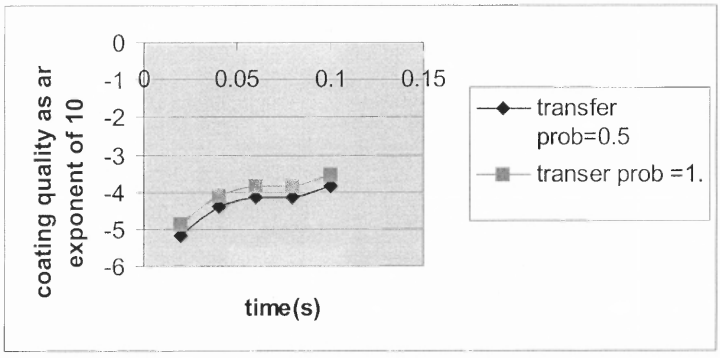


**Figure 4.44** The coating quality as a function of time.

## REFERENCES


1. Singh, R. K., Ata, A., Fitz-Gerald, J., Rabinovich, Y. I., Hendrickson, W. Dry coating method for synthesis of composite particulates. *KONA* 1997,**15**, 121

2. Bradley, R. S., *Philos. Mag.*1932, **13**, 853

3. Bradley, R. S., *Trans. Faraday Soc.*1936, **32**, 1088

4. Derjaguin, B. V., *Kolloid Z.* 1934, **69**, 155

5. Krupp, H., *Adv. Colloid Interface Sci.* 1967, **1**, 111

6. Johnson, K. L., Kendall, K., Roberts, A. D., *Proc. R. Soc. Lond. A* 1971, **324**, 301

7. Derjaguin, B. V., Muller, V. M., Toporov, P. Y., *J. Colloid Interface Sci.* 1975, **53**, 314

8. Muller, V. M., Yushchenko, V. S., Derjaguin, B. V., *J. Colloid Interface Sci.* 1980, **77**, 91

9. Muller, V. M., Yushchenko, V. S., Derjaguin, B. V., *Colloid Surfaces 1983*, **7**, 251

10. Rogers, L. N. and Reed, J., *J. Phys. D: Appl. Phys.* 1984, **17**, 677

11. Dahneke, B. Particle-surface collision dynamics: what might they tell us? *Advances in Particle Adhesion*. Gordon and Breach publishers. Netherlands.1996, 125-137

12. Quesnel, D. J., Rimai, D. S., DeMejo, L. P., *Solid State Commun.*1993, **85**, 171

13. Quesnel, D. J., Rimai, D. S., DeMejo, L. P., *Phys. Rev. B.* 1993, **48**, 6795

14. Quesnel, D. J.,Rimai, D. S., DeMejo, L. P. Molecular dynamic modeling of interfacial energy. *J. Adhesion Sci. Technol.* 1995, **9**, 1015-1030

15. Quesnel, D. J., Rimai, D. S., DeMejo, L. P. Molecular Dynamic Modeling of Particle Modeling. *Journal of Adhesion* 1995, **51**, 49

16. Walton,O.R. Numerical simulation of inclined chute flows of monodisperse, inelastic, frictional spheres. *Mechanics of Materials* 1993, 239-247

17. Kafui, K. D. and Thornton, C. Computer simulated impact of agglomerates. *Powders & Grains* 1993, **93**, 401-406

18. Ning, Z., Boerefijn, R., Ghadiri, M., Thornton, C. Effects of particle size and bond strength on impact breakage of weak agglomerates. *Powders & Grains* 1997, **97**, 127-130

19. Lian, G., Thornton, C., Adams, M. J. Effect of liquid bridge forces on agglomerate collisions. *Powders & Grains* 1993, **93**, 59-64

20. Lian, G., Thornton, C., Adams, M. J. A microscopic simulation of oblique collisions of wet agglomerates. *Powders & Grains* 1997, **97**, 159-162

21. Ning, Z. and Thornton, C. Elastic-plastic impact of fine particles with a surface. *Powders & Grains* 1993, **93**, 33-38

22. Thornton, C. Coefficient of restitution for collinear collisions of elastic-perfectly plastic spheres. *Journal of Applied Mechanics* 1997, **64**, 383-386

23. Israelachvili, Jacob *Intermolecular and Surface Forces*. Academic Press. San Diego. California. 1991

24. Hockney, R. W. and Eastwood, J.W. *Computer Simulation using Particles*. McGraw-Hill. New York. 1981

25. Maugis, D. and Pollock, H. M. Surface forces, deformation and adherence at metal microcontacts. *Acta Metallica* 1984, **32**, 9, 1323-1334.

26. Maugis, D. Adhesion of spheres: The JKR-DMT transition using a Dugdale model. *Journal of Colloid and Interface Science* 1992, **150**, 1, 243-269.

27. Maugis, D. Extension of the Johnson-Kendall-Roberts theory of the elastic contact of spheres to large contact radii. *Langmuir* 1995, **11**, 679-682.

28. Smith, S., Beardmore, K., Gras-Marti, A. Molecular dynamics simulations of particle-surface interactions. *Vacuum* 1995, **46**, 8-10, 1196.

29. *Handbook of Chemistry and Physics*. CRC Press. New York. **79**. 1998.

30. *American Institute of Physics Handbook*. Mc Graw Hill. New York. **3**. 1972.

31. *Encyclopedia of Material Science and Engineering*. Pergamon Press. New York. **1**. 65. 1988.

32. Moakher, M.and Muzzio, M., 1998, DEM code.

33. Walton, O. R. and Braun, R. L. Viscosity and temperature calculations for shearing assemblies of inelastic, frictional disks. *J. Rheol* 1986, **30** , 949-980.

34. Walton, O. R., Numerical simulation of inelastic, frictional particle-particle interactions, *Particulate Two-Phase Flow*. M.C. Roco. Butterworth-Heinemann. Boston. 884-911. 1992.

35. Roller, B. *Physics: Electricity, Magnetism and Light*. Holden-Day. San Francisco. **2**. 1194.

36. Good, R. H. and Nelson, T. J. *Classical Theory of Electric and Magnetic Fields.* Academic Press. New York. 221. 1971.

37. Dave, R. N., Wu., C. Y., Chaudhuri, B., Watano, S.Magnetically Mediated Flow Enhancement for Controlled Powder Discharge of Cohesive Powders. *Powder Technology* 1999, Accepted.

38. *OpenGL Programming Guide.* Addison Wesley. Massachusetts. **3.** Version 1.2. 1999.

39. *X Toolkit Intrinsics Reference Manual.* O'Reilly & Associates Inc. Massachusetts. Release 4&5. 1992.

40. Alonso Gamez, M. *A Fundamental Study on the Coating of Powders.* Ph.D. Thesis presented to the College of Engineering of Osaka Prefecture University. Osaka. Japan. 1992.

41. Gale J., Professor, The Department of Chemistry, Imperial College of Science, Technology and Medicine, London, UK. Email communications. Email: j.gale@ic.ac.uk